Jet Azimuthal Angle Asymmetries in Deep Inelastic Scattering as a test of QCD

Thesis for the degree of Doctor of Philosophy in Physics
by

Christian Jacobsson

1666

DEPARTMENT OF PHYSICS, UNIVERSITY OF LUND
LUND 1994

ISBN 91-628-1470-2
LUNFD6/(NFFL-7093)1994

Jet Azimuthal Angle Asymmetries in Deep Inelastic Scattering as a test of QCD

By due permission of the faculty of mathematics and natural science at the University of Lund to be publicly discussed at the lecture hall B at the department of Physics, January 13 1995, at 10.15 a.m. for the degree of Doctor of Philosophy.

by

Christian Jacobsson
Department of Physics, University of Lund, Sölvegatan 14, S-22362 Lund, Sweden

This thesis is partly based on the following articles, included as Appendices A-D:

A Asymmetries in Jet Azimuthal Angle Distributions as a Test of QCD,
Proceedings 'Physics at HERA', Eds.W. Buchmüller, G. Ingelman,
DESY Hamburg 1992 vol. 1, p. 331
LUNFD 6/(NFFL-7069) 1992

B Study of Jet Reconstruction Algorithms for Deep-Inelastic Events at Hera
Z. Phys. C 63, 49-62 (1994)

C Jet Identification based on Probability Calculations using Bayes' Theorem
To be submitted to Zeitschrift für Physik

D The H1 Forward Muon Spectrometer,
Nucl. Instr. and Meth. A 340 (1994) 304-308

KRONTRYCK - ESLÖV

Contents

Preface 3

Introduction 5

1 Basic theory of Deep Inelastic Scattering 7

- 1.1 DIS kinematics . . . 7
- 1.2 Four-vectors in the laboratory frame . . . 9
- 1.3 Four-vectors in the hadronic cms . . . 10
- 1.4 Zeroth order QCD process . . . 11
- 1.5 First order QCD processes . . . 14
- 1.6 Summary and outlook from the theory . . . 22

2 HERA and the H1 detector 25

- 2.1 HERA . . . 25
- 2.2 The H1 detector . . . 26
  - 2.2.1 Tracking . . . 28
  - 2.2.2 Calorimetry . . . 29
  - 2.2.3 Magnet . . . 30
  - 2.2.4 Muon system . . . 30
  - 2.2.5 Trigger . . . 31

3 Analysis 33

- 3.1 Event selection . . . 33
- 3.2 Kinematic reconstruction . . . 35
- 3.3 Transformation to the hadronic cms . . . 36
- 3.4 Jet reconstruction . . . 37
- 3.5 Further requirements . . . 39
- 3.6 Azimuthal acceptance . . . 41
- 3.7 Jet identification . . . 45
- 3.8 Results . . . 46
- 3.9 Conclusions . . . 48

Acknowledgements 49

Appendices

A Asymmetries in Jet Azimuthal Angle Distributions as a Test of QCD 53

B Study of Jet Reconstruction Algorithms for Deep-Inelastic Events at HERA 55

C Jet Identification based on Probability Calculations using Bayes' Theorem 57

D The H1 Forward Muon Spectrometer 59

To my parents:
Inger and Bengt

Preface

What's the point of it?
That's the most common question I get from friends, concerning my work. The answer to that question is another question. What's the point of everything? That's what physics is all about. Why is there a Universe? Why does it look like it does? Why does it contain humans who question, not only their own existence, but the existence of the Universe itself. And people claim physics is boring?!

Particle physics is a science that to a great extent exist just because people are curious and want to have answers to these questions. There is no basic need that motivates the research. The results do not make life easier, at least not in the near future. Perhaps in many years from now, the knowledge we have gained might be used to tackle problems that we can hardly imagine today. Who knows? It should therefore be regarded as a great favor to have been allowed to work in this field.

My interest in physics started when I was just a kid. It was my father who got me interested. As long as I can remember he has wondered about these great questions, and we have had long discussions, but I can tell you, we couldn't answer any. As a Ph.D. student, working with a tiny detail of a theory for the strong force, I often forgot what physics is all about and started to question what I was really doing. My contribution to a better understanding of the great questions is probably completely negligible, but nevertheless, I'm very glad that I got the opportunity to learn more about how things work in the Universe.

Maybe all the great questions cannot be answered until we have a better understanding of ourselves. I mean, why do we ask these questions? What is meant by understanding? What is knowledge? Who knows? Jesus, I'm more puzzled than ever before!

Christian Jacobsson
Lund, November 1994

Introduction

The subject of this thesis is lepton-hadron azimuthal asymmetries in Deep Inelastic Scattering (DIS) processes in general, and in particular how the asymmetry of the first order processes in QCD has been measured for the first time at HERA. According to theory, the cross section of both zeroth and first order processes in QCD exhibit a dependence on the azimuthal angle of the jet/jets with respect to the scattered lepton. Already in 1978, Georgi and Politzer [1] suggested a measurement of the azimuthal asymmetries of first order processes as an interesting test of QCD. Since then, several attempts to experimentally verify this phenomenon have been performed [2] [3] [4] [5] without any success. In these attempts, with data from different fixed target experiments, the center-of-mass energies have not been high enough to enable production of experimentally resolvable first order processes. The measurements were mainly sensitive to the azimuthal dependence of zeroth order processes which has its origin in the Fermi motion of the partons inside the proton. This has been theoretically studied by Cahn in [6] [7].

HERA, on the other hand, is designed for center-of-mass energies of up to 314 GeV and large amounts of resolvable first order processes will, and already have, been produced. The first Monte Carlo study of the specific problems connected with a measurement at HERA was conducted in 1991 for the Workshop 'Physics at HERA' and can be found in appendix A. The paper describes the procedure of such a measurement on a sample of QCD-Compton processes.

Several 'subproblems' that needed special and separate attention were revealed in this first investigation. Since HERA is the worlds first *ep* collider, specific problems concerning the reconstruction of jets had to be dealt with. An extensive comparison of the five most common jet algorithms in their ability to separate the very energetic proton spectator jet from the hard subprocess, and at the same time resolve the jets of the hard subprocess, was therefore carried out, see appendix B. Another subproblem concerned the identification of jets as originating from the quark or the gluon in the QCD-Compton process. This has been studied in a general context of identifying jets, irrespective of whether they are produced at an e^+e^- or an *ep* collider and the results are presented in appendix C.

Apart from these problems related to a direct and specific measurement, I have also contributed to the construction and tests of the Forward Muon Spectrometer, a combined effort of the Manchester and Lund Universities. The detector and its performance is presented in appendix D. I have also participated in the work on a physics analysis program package (PHAN) that is now used by the entire collaboration. I developed the routines concerning collective treatments of particles, like jet algorithms, Lorentz transformations and rotations etc, routines I could benefit from in the analysis of the azimuthal asymmetries.

Due to the limited statistics collected from HERA 1993, on which this analysis was based, the planned measurement of the azimuthal asymmetries of QCD-Compton processes was not possible. The bulk of the existing events is produced at low values of x and Q^2 where Boson Gluon Fusion processes dominate over QCD-Compton processes. An attempt to measure the azimuthal asymmetries of such a sample has therefore been made.

This thesis is divided into three chapters. The first chapter describes the basic physics of Deep Inelastic Scattering and what the theory predicts for the azimuthal asymmetries.

The second chapter presents the 'tools' for the measurement, namely the HERA collider and the H1 experiment. Finally, in chapter three, the complete analysis of a first attempt to measure the azimuthal asymmetries, with all the subproblems mentioned earlier, is presented. A third subproblem, that actually deserved an investigation by itself, is also presented here. It concerns the acceptance of events with jets in specific azimuthal angles, and the outcome turned out to be quite against, at least my, intuition. The final results of the first azimuthal asymmetry measurement indicate that... Well, you'll just have to read the thesis to find out.

Chapter 1

Basic theory of Deep Inelastic Scattering

In this chapter the basic concepts of deep inelastic scattering of electrons on protons will be described. The standard variables used to describe the kinematics of the events are defined and the four-vectors of the interacting particles are expressed, both in the laboratory system and in the, from a physics point of view, more suitable hadronic center-of-mass system. The expressions for the parton cross sections, for both zeroth and first order QCD processes are presented, including their dependence on the azimuthal angle of the final state partons. Finally, conclusions for the measurability of this azimuthal angle dependence will be drawn.

1.1 DIS kinematics

In fig. 1.1 the simplest deep inelastic scattering process described by the Quark Parton Model (QPM) is depicted. The incoming electron (with a four-momentum p_e) is scattered against a quark (p_i) in the proton (P) under the exchange of a boson (q). The scattered lepton (p_l) balances the scattered quark (p_f) in transverse momentum. The figure is drawn as it would look in the laboratory system with the proton colliding head on with the electron. The coordinate system is defined according to H1-standard with the +z-direction given by the direction of the proton beam, and the polar angle of the scattered lepton (θ_l) is thus measured with respect to this direction.

The kinematics of deep inelastic processes can be described by just two independent variables, from which all other global variables can be derived. In neutral current events, where the exchanged boson is either a virtual photon or a Z^0 and where the scattered lepton is an electron, the energy (E_l) and angle (θ_l) of the scattered electron is normally measured to extract the values of the kinematic variables, see fig. 1.1. Other methods using the final state hadrons are also possible. The definition of three commonly used Lorentz invariant kinematic variables is given below, together with their relations to a measurement of the scattered lepton. If the masses of the scattered lepton and the

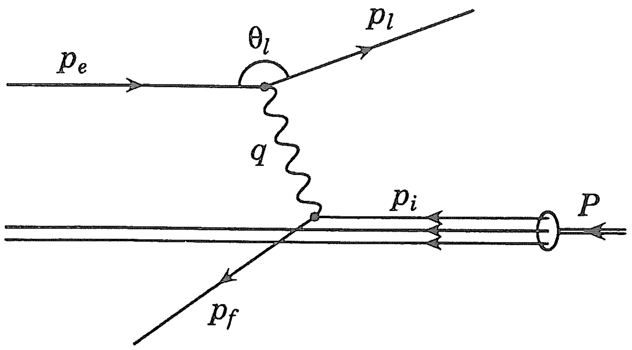

Figure 1.1: *Deep Inelastic ep scattering: the QPM process viewed in the laboratory system.*

colliding electron and proton are neglected, the relations between the kinematic variables and E_ℓ and θ_ℓ simply are:

$$\begin{aligned} Q^2 &\equiv -q^2 = -(p_e - p_\ell)^2 \approx 4E_eE_l\cos^2(\theta_\ell/2) \\ x &\equiv \frac{Q^2}{2P\cdot q} \approx \frac{E_eE_\ell\cos^2(\theta_\ell/2)}{E_p(E_e - E_\ell\sin^2(\theta_\ell/2))} \ ; \ (0 \le x \le 1) \\ y &\equiv \frac{P\cdot q}{P\cdot p_e} \approx \frac{E_e - E_\ell\sin^2(\theta_\ell/2)}{E_e} \ ; \ (0 \le y \le 1) \end{aligned} \tag{1.1}$$

Q^2 is the momentum transfer variable, related to the mass of the exchanged boson, followed by the dimensionless Bjorken-x and y. If we assume the quark in the initial state to have a fraction ξ of the proton's momentum, $p_i = \xi P = \xi(E_p, 0, 0, E_p)$ and the final quark is assumed massless, $p_f^2 = 0$, the Bjorken-x variable has an interpretation as the momentum fraction of the proton carried by the struck quark.

$$p_f^2 = (p_i + q)^2 = (\xi P + q)^2 \approx 2\xi P\cdot q - Q^2 \quad ; \quad p_f^2 = 0 \Rightarrow \xi = x \tag{1.2}$$

An interpretation of y is most easily given in the frame where the proton is at rest, i.e. the fixed target situation. y is then the energy fraction of the incoming lepton taken by the exchanged boson, $y = q_0/E_e$, where q_0 denotes the energy of the exchanged boson. The relationship between these three kinematic variables is conveyed by the total invariant mass squared (s) of the colliding electron and proton.

$$\begin{aligned} s &\equiv (p_e + P)^2 \approx 4E_eE_p \\ Q^2 &\approx xys \end{aligned}$$

Another useful variable is the invariant mass squared of the hadronic system

$$W^2 \equiv (P + q)^2 \approx Q^2\frac{1-x}{x}$$

Figure 1.2 illustrates the relationships of the kinematic variables x, y, Q^2, W^2 and the scattered lepton energy E_l and angle θ_l. A few examples of iso-curves of Bjorken-y, W^2, E_l and θ_l is shown. At HERA a very large domain in all these variables is spanned. Former fixed target experiments covered roughly $y < 0.01$ and Q^2 up to 100 GeV^2.

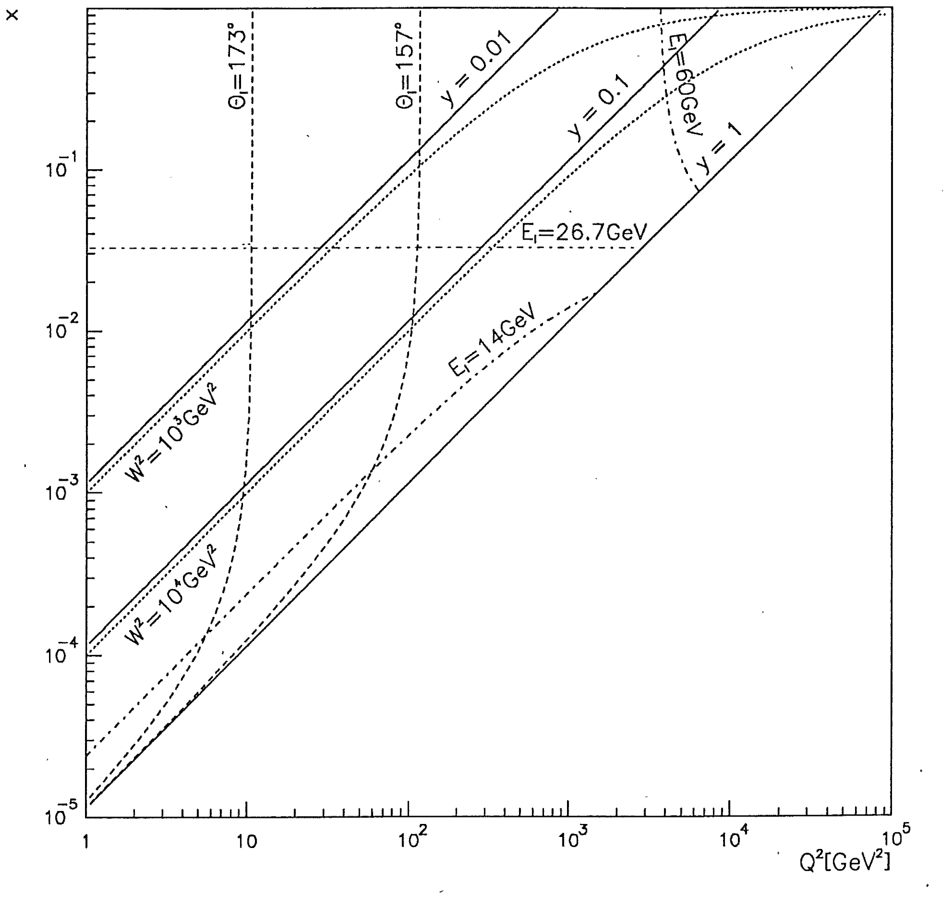

Figure 1.2: *Contour plots of Bjorken-y, W^2, θ_l and E_l in the x, Q^2 plane for $\sqrt{s}$ = 296 GeV at HERA.*

1.2 Four-vectors in the laboratory frame

Using the relations (1.1) it is possible to express the four-vectors of the scattered lepton (p_ℓ), the exchanged vector boson (q), and, in zeroth order assuming the quark parton model, also the scattered quark, both before (p_i) and after (p_f) the interaction.

$$\begin{aligned} P &= (E_p, 0, 0, E_p) \\ p_e &= (E_e, 0, 0, -E_e) \\ p_\ell &= \left(\frac{Q^2}{4E_e} + E_e(1-y), \sqrt{Q^2(1-y)}, 0, \frac{Q^2}{4E_e} - E_e(1-y)\right) \end{aligned} \qquad (1.3)$$

$$\begin{aligned}
q &= \left(yE_e - \frac{Q^2}{4E_e}, -\sqrt{Q^2(1-y)}, 0, -yE_e - \frac{Q^2}{4E_e}\right) \\
p_i &= x(E_p, 0, 0, E_p) \\
p_f &= \left(yE_e + \frac{Q^2(1-y)}{4E_e y}, -\sqrt{Q^2(1-y)}, 0, -E_e y + \frac{Q^2(1-y)}{4E_e y}\right)
\end{aligned}$$

As mentioned earlier, the +z-direction is given by the direction of the proton beam, and to simplify the expressions further, the xz-plane is defined by the two vectors $\bar{p}_\ell$ and $\bar{P}$ and therefore all y-components become zero.

1.3 Four-vectors in the hadronic cms

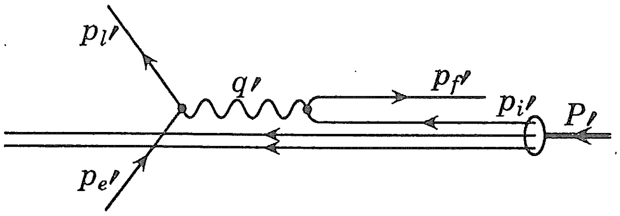

Figure 1.3: *Deep-inelastic ep scattering: the QPM viewed in the hadronic cms.*

The laboratory frame is not always suited for physics studies. More preferable is the hadronic center-of-mass system (cms), i.e. the cms of the exchanged boson q and the incoming proton P, see fig. 1.3. For instance, the azimuthal angle of jets with respect to the scattered electron, which is a vital quantity in the analysis presented in this thesis, could in principle be expressed in a Lorentz invariant way. The results are, however, much more easily interpreted in the hadronic cms. Therefore it is necessary to also express the four-vectors (1.3) in this cms. To do this we must first calculate some invariants to enable the transformation from the laboratory system to the hadronic cms. If P_a and P_b represent the four-vectors of two colliding particles a and b of equal but opposite momentum, the invariant mass squared of the collision is

$$M_{ab}^2 = (P_a + P_b)^2 = -M_a^2 + M_b^2 + 2E_a M_{ab} \quad \Leftrightarrow \quad E_a = \frac{1}{2M_{ab}}(M_{ab}^2 + M_a^2 - M_b^2)$$

Using this expression we can derive the energies of the colliding proton and boson in the hadronic cms.

$$\begin{aligned}
E_{p'} &= \frac{1}{2W}(W^2 + M_p^2 - M_q^2) \approx \frac{W^2 + Q^2}{2W} = \frac{2yE_eE_p}{\sqrt{4yE_eE_p - Q^2}} \\
q_{0'} &= \frac{1}{2W}(W^2 + M_q^2 - M_p^2) \approx \frac{W^2 - Q^2}{2W} = \frac{2yE_eE_p - Q^2}{\sqrt{4yE_eE_p - Q^2}} \qquad (1.4)
\end{aligned}$$

In order to get the energy and the momentum in the z-direction (again defined by the proton beam direction) of the incoming electron, the following invariants are used:

$$\begin{aligned}
p_e \cdot (P+q) &= p_e' \cdot (P'+q') = E_e'(E_p' + q_0') \\
\Rightarrow E_e' &= \frac{E_e(2E_p + q_0 + q_z)}{E_p' + q_0'} = \frac{4E_eE_p - Q^2}{2\sqrt{4yE_eE_p - Q^2}} \\
p_e \cdot P &= p_e' \cdot P' = E_e'E_p' - p_{ez}'E_p' \\
\Rightarrow p_{ez}' &= \frac{E_e'E_p' - 2E_eE_p}{E_p'} = \frac{Q^2(2-y) - 4yE_eE_p}{2y\sqrt{4yE_eE_p - Q^2}}
\end{aligned} \tag{1.5}$$

The transverse momentum of the incoming and scattered electron is simply $p_{e\perp}' = p_{\ell\perp}' = \sqrt{E_e'^2 - p_{ez}'^2} = \sqrt{Q^2(1-y)/y}$, and using the facts that $p_\ell' = p_e' - q'$, $p_i' = xP'$ and $p_f' = p_i' + q'$, the complete list of four-vectors now becomes:

$$\begin{aligned}
P' &= \frac{2yE_eE_p}{\sqrt{4yE_eE_p - Q^2}}(1,0,0,1) \\
p_e' &= \left(\frac{4E_eE_p - Q^2}{2\sqrt{4yE_eE_p - Q^2}}, \frac{\sqrt{Q^2(1-y)}}{y}, 0, \frac{Q^2(2-y) - 4yE_eE_p}{2y\sqrt{4yE_eE_p - Q^2}}\right) \\
p_\ell' &= \left(\frac{4E_eE_p(1-y) + Q^2}{2\sqrt{4yE_eE_p - Q^2}}, \frac{\sqrt{Q^2(1-y)}}{y}, 0, \frac{Q^2(2-y) - 4yE_eE_p(1-y)}{2y\sqrt{4yE_eE_p - Q^2}}\right) \\
q' &= \frac{2yE_eE_p}{\sqrt{4yE_eE_p - Q^2}}\left(1 - \frac{Q^2}{2yE_eE_p}, 0, 0, -1\right) \\
p_i' &= xP' \\
p_f' &= \frac{2yE_eE_p}{\sqrt{4yE_eE_p - Q^2}}\left(1 - \frac{Q^2}{4yE_eE_p}, 0, 0, -(1 - \frac{Q^2}{4yE_eE_p})\right)
\end{aligned} \tag{1.6}$$

1.4 Zeroth order QCD process

In this section, presenting the cross-section of the zeroth order process, I will basically follow the recipe given by Cahn in [6] [7], but give the expressions with a somewhat higher precision which is motivated by the HERA conditions at low values of Q^2. I will also present some results relevant for the ep-collisions at HERA. The differential partonic cross section for pure γ exchange (valid for Q^2 up to around $M_z^2 \sim 10^4\ GeV^2$ above which the contribution from Z^0 exchange becomes significant) can be expressed in the following way:

$$\frac{d^2\hat{\sigma}_i}{dxdy} = \frac{2\pi\alpha^2 Q_i^2}{Q^2} y \frac{\frac{1}{2}\{(p_e' \cdot p_i')^2 + (p_l' \cdot p_f')^2 + (p_l' \cdot p_i')^2 + (p_e' \cdot p_f')^2\}}{(p_i' \cdot p_f')^2} \tag{1.7}$$

where α is the electromagnetic coupling constant and Q_i is the charge of the scattered quark. (The expression within the curly brackets could have been written in a reduced form since $p_e' \cdot p_i' = p_l' \cdot p_f'$ and $p_l' \cdot p_i' = p_e' \cdot p_f'$, but is kept like this for comparison with the corresponding expression from first order calculations in the next section.) Using the four-vectors in eqns. (1.6) when calculating (1.7), we end up with:

$$\frac{d^2\hat{\sigma}_i}{dxdy} = \frac{2\pi\alpha^2 Q_i^2}{yQ^2}(1+(1-y)^2)$$

If we on the other hand take the Fermi motion of the partons inside the proton into account, i.e. we allow for some intrinsic transverse momentum of the initial state parton, $p_i' = (\sqrt{p_\perp^2 + p_{||}^2}, p_\perp \cos\phi, p_\perp \sin\phi, p_{||})$ where $p_{||}$ is given by $0 = p_f^2{}' = (p_i' + q')^2 \Rightarrow p_{||} = P'[x + \frac{1-2x}{2}(1 - \sqrt{1 + 4p_\perp^2/Q^2})] \approx P'[x - (1-2x)\frac{p_\perp^2}{Q^2}]$, the cross section instead becomes:

$$\begin{aligned}\frac{d^2\hat{\sigma}_i}{dxdy} &= \frac{2\pi\alpha^2 Q_i^2}{yQ^2}\{\,(1+(1-y)^2) + 4\frac{p_\perp^2}{Q^2}(1-y) \\ &\quad - 4\frac{p_\perp}{Q}\sqrt{1-y}(2-y)\cos\phi \;+\; 4\frac{p_\perp^2}{Q^2}(1-y)\cos 2\phi\,\}\end{aligned}$$

which is of the type $A+B\cos\phi+C\cos 2\phi$. The azimuthal angle ϕ of the scattered quark is measured with respect to the scattered lepton. To get the full expression for the hadronic cross section we, of course, have to take the proton structure function into account, and the intrinsic transverse momentum of the current quark should be represented by a gaussian function instead of a fixed $p_\perp$. For an investigation of the azimuthal asymmetry and how this varies with x and Q^2 it is however enough to study the partonic cross section. This is especially true if the the asymmetry is expressed as the average values of $\cos\phi$ and $\cos 2\phi$, as it normally is in the literature. Expressed in this way, the proton structure function does not enter, as can be seen from the following definition:

$$\begin{aligned}<\cos\phi> &\equiv \frac{\int f(\phi,...)\cos\phi d\phi}{\int f(\phi,...)d\phi} = \frac{B}{2A} \\ <\cos 2\phi> &\equiv \frac{\int f(\phi,...)\cos 2\phi d\phi}{\int f(\phi,...)d\phi} = \frac{C}{2A}\end{aligned}$$

where $f(\phi,...)$ in our case is $A + B\cos\phi + C\cos 2\phi$. These average values thus relate the amplitudes B for $\cos\phi$, and C for $\cos 2\phi$, to A, the cross section integrated over ϕ. From an experimental point of view, working with a limited data sample, these averages are also relevant since they indicate where in x and Q^2 the most accurate measurement of the asymmetry can be made. If the aim of a measurement is simply to clarify if a dependence on the azimuthal angle exist or not, a χ^2 defined as follows would give the answer:

$$\chi^2 = \int_0^{2\pi}\left(\frac{(A+B\cos\phi+C\cos 2\phi)-A}{\sqrt{A+B\cos\phi+C\cos 2\phi}}\right)^2 d\phi \approx \pi\frac{B^2+C^2}{A}$$

An indication of a ϕ dependence (high χ^2) would thus most easily be achieved where $(B^2+C^2)/A$ is large. The average values of $\cos\phi$ and $\cos 2\phi$ are therefore not perfect variables to find the best region in x and Q^2 for an accurate measurement, but should at least give a rough estimate of where to direct ones interest. These averages, for the zeroth order process, looks like

$$\begin{aligned}<\cos\phi> &= -\frac{2p_\perp}{Q}\frac{\sqrt{1-y}(2-y)}{1+(1-y)^2+\frac{4p_\perp^2}{Q^2}(1-y)} \\ <\cos 2\phi> &= \frac{2p_\perp^2}{Q^2}\frac{1-y}{1+(1-y)^2+\frac{4p_\perp^2}{Q^2}(1-y)}\end{aligned}$$

How these averages vary with x and Q^2 is shown in fig. 1.4. We see that the $\cos\phi$ dependence is a lot stronger than the $\cos 2\phi$ dependence and that the absolute values of the averages grow with decreasing Q^2 and also somewhat with increasing x.

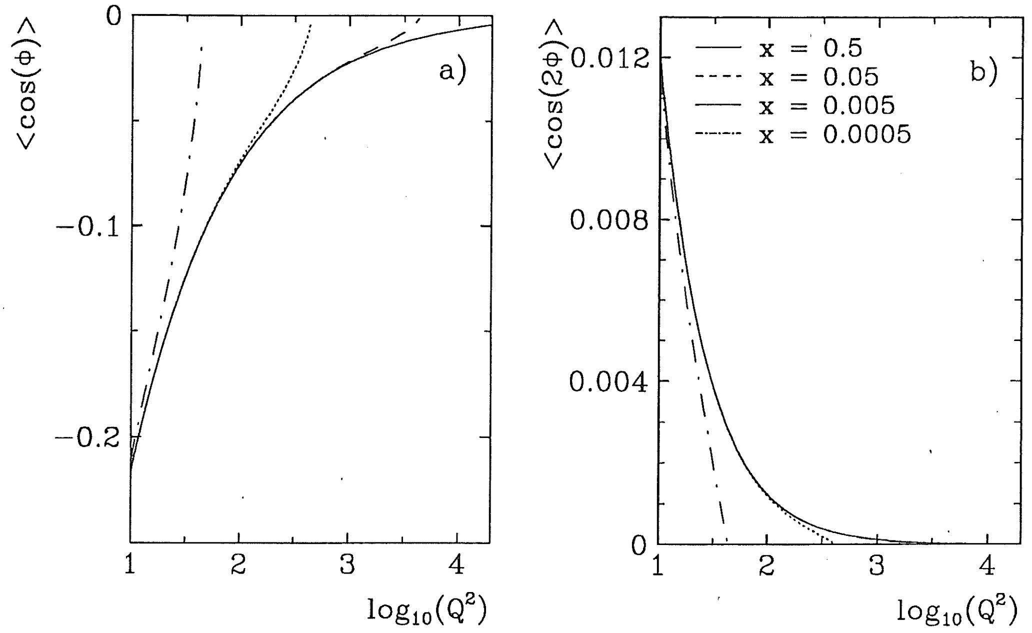

Figure 1.4: *The x and Q^2 dependence of average a) $\cos\phi$, b) $\cos 2\phi$ for the zeroth order process. The intrinsic transverse momentum of the initial quark is simulated as a gaussian distribution of width* 0.44 *GeV.*

An intuitive understanding of why the cross section depends on the azimuthal angle is not easily achieved. One can say that the dependence is due to helicity conservation and the spin of the interacting particles. The incoming and scattered electron are both either left handed or right handed since helicity is conserved at the photon vertex. The polarization of the exchanged photon will thus be determined from the azimuthal orientation of the plane defined by the incoming and scattered electron, see fig. 1.3. Helicity is also conserved at the vertex of the incoming and scattered quark and therefore some directions of the plane spanned by the incoming and scattered quark, with respect to the electron plane, are preferred. This leads to an azimuthal dependence in the cross section. However, the exchanged virtual photon has three possible polarization states, and when calculating the matrix element, the square of the sum of different polarization states leads to interference terms. A simple intuitive understanding of the exact expression for the azimuthal angle dependence is therefore hard to achieve.

The asymmetry of the zeroth order process is not implemented in any of the existing event generators, i.e. the intrinsic transverse momentum of partons inside the proton is normally simulated, but the cross section dependence on the azimuthal angle is not. This is normally justified by the small transverse energies connected with the Fermi motion in comparison with the much higher transverse momenta of higher order QCD emissions.

1.5 First order QCD processes

There are two different types of first order processes, the QCD-Compton and the Boson Gluon Fusion (BGF) processes, depicted in fig. 1.5. Both processes have a ϕ-dependent cross section, i.e. the cross section varies with the azimuthal angle of the hadron plane, defined by the two final partons p_2 and p_3, with respect to the lepton plane, defined by $p_{e'}$ and $p_{l'}$. p_1 denotes the four-momentum of the initial interacting parton. When presenting the partonic cross sections I will follow the style and prescription of Chay, Ellis and Stirling [8][1] and, as in the former section, try to present results relevant for HERA conditions.

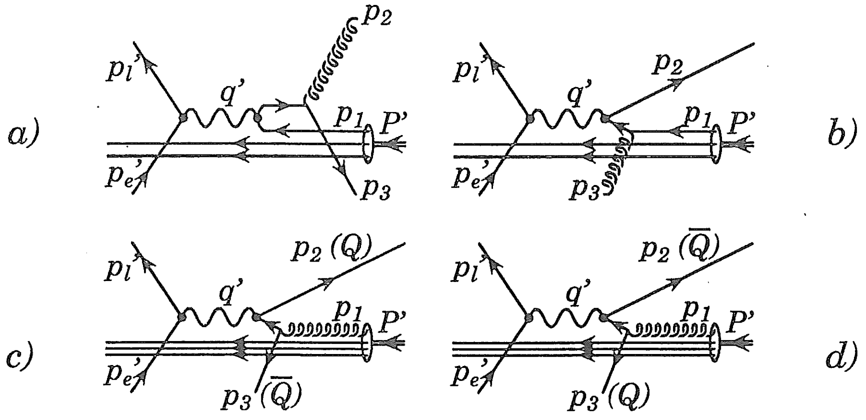

Figure 1.5: *a) and b) show the QCD-Compton process with the gluon emitted in the final and initial state, respectively. Indicated is also the two possibilities of labeling the quark and the gluon. The gluon can be labeled* p_2 *and thus have the energy fraction* z *and the quark* p_3 *with the energy fraction* $1-z$*, as in a), or vice versa as in b). In c) and d) the corresponding two possibilities of labeling the quark and the antiquark in the Boson Gluon Fusion process is shown.*

In the description of first order processes in QCD, the following variables are useful:

$$\begin{aligned} x_p &\equiv \frac{Q^2}{2p_1\cdot q} \quad ; \quad x_p=\frac{x}{\xi} \\ z &\equiv \frac{p_1\cdot p_2}{p_1\cdot q} \quad ; \quad 1-z=\frac{p_1\cdot p_3}{p_1\cdot q} \end{aligned} \tag{1.8}$$

where x_p is the 'partonic' version of Bjorken-x and z describes how the momentum is shared between the two outgoing partons, p_2 and p_3. These variables enable us to express the four-vectors $p_2, p_3, p_{e'}$ and $p_{l'}$ in terms of p_1 and q', the transverse momentum of the

---

[1] A few errors in this reference should be noted: Except for some inconsistency with indexing of the hadronic current, qg, gq and $q\bar{q}$, in equations 16-18, the equations 38 for the inclusive cross sections at page 50 are wrong. For correct expressions I refer to [9] or this thesis.

final partons ($\bar{p}_\perp$) and the transverse momentum of the leptons ($\bar{k}_\perp$), which simplifies the calculations of the partonic cross sections.

$$\begin{aligned}
p_2 &= (1 - x_p - z + 2x_p z)p_1 + zq' + \tilde{p}_\perp \\
p_3 &= (x_p + z - 2x_p z)p_1 + (1-z)q' - \tilde{p}_\perp \\
p_{e'} &= \frac{x_p}{y}(2-y)p_1 + \frac{1}{y}q' + \tilde{k}_\perp \\
p_{\ell'} &= \frac{x_p}{y}(2-y)p_1 + \frac{1-y}{y}q' + \tilde{k}_\perp
\end{aligned}$$

where $\tilde{p}_\perp = (0, \bar{p}_\perp, 0)$ and $\tilde{k}_\perp = (0, \bar{k}_\perp, 0)$ and

$$p_\perp^2 = \frac{(1-x_p)z(1-z)}{x_p}Q^2 \quad ; \quad k_\perp^2 = \frac{1-y}{y^2}Q^2$$

The parton cross section can be expressed like

$$\frac{d^5\hat{\sigma}_{ij}}{dx_p dy dz dp_\perp^2} = \frac{\alpha^2 Q_q^2}{16\pi^2 Q^4} y \delta(p_\perp^2 - \frac{(1-x_p)z(1-z)}{x_p}Q^2) L_{\mu\nu} M_{ij}^{\mu\nu}$$

where Q_q is the charge of the scattered quark and $L_{\mu\nu}(M_{ij}^{\mu\nu})$ is the square of the leptonic (hadronic) current and $dp_\perp^2 = p_\perp dp_\perp d\phi$. It is enlightening to separate the cross sections for the QCD-Compton and BGF processes, and in addition the cases when the gluon momentum fraction is given by z ($M_{gq}^{\mu\nu}$) and by $1-z$ ($M_{qg}^{\mu\nu}$), see fig. 1.5 and eqn. (1.8), since we can then study the asymmetry of the gluon and the quark in the QCD-Compton process individually. For the BGF cross section, nature does not distinguish quarks from anti-quarks in this respect and we therefore only get one expression ($M_{q\bar{q}}^{\mu\nu}$). For pure photon exchange the currents can be written:

$$L_{\mu\nu} M_{qg}^{\mu\nu} = \frac{64\pi}{3}\alpha_s Q^2 \frac{(p_{e'} \cdot p_1)^2 + (p_{\ell'} \cdot p_2)^2 + (p_{\ell'} \cdot p_1)^2 + (p_{e'} \cdot p_2)^2}{p_1 \cdot p_3 \;\; p_2 \cdot p_3} \tag{1.9}$$

$$L_{\mu\nu} M_{gq}^{\mu\nu} = \frac{64\pi}{3}\alpha_s Q^2 \frac{(p_{e'} \cdot p_1)^2 + (p_{\ell'} \cdot p_3)^2 + (p_{\ell'} \cdot p_1)^2 + (p_{e'} \cdot p_3)^2}{p_1 \cdot p_2 \;\; p_2 \cdot p_3} \tag{1.10}$$

$$L_{\mu\nu} M_{q\bar{q}}^{\mu\nu} = 8\pi\alpha_s Q^2 \frac{(p_{e'} \cdot p_3)^2 + (p_{\ell'} \cdot p_2)^2 + (p_{\ell'} \cdot p_3)^2 + (p_{e'} \cdot p_2)^2}{p_1 \cdot p_2 \;\; p_1 \cdot p_3} \tag{1.11}$$

where α_s is the strong coupling constant. Note that apart from propagator factors, these expressions depend only on dot products between the leptons and quarks in exactly the same combinations as for the zeroth order process, see eqn. (1.7) in the previous section. As pointed out in [11], this is an indication of that there is no 'new' physics in the first order QCD cross section, it is just a kinematic reorganization of the 'old' QPM process. What has already been stated about the reason for an azimuthal dependence of the QPM cross section is thus also valid for these first order processes - it is just an effect of the spin of the exchanged boson and the helicity conserving interaction. However, the exact size of the azimuthal angular dependence is given by the specific expressions for the first order QCD processes. Carrying out the tedious four-vector calculations in eqns. (1.9-1.11) we end up with:

$$\begin{aligned}
L_{\mu\nu}M^{\mu\nu}_{qg} &= \frac{64\pi}{3}\alpha_s Q^2\frac{1}{y^2}[(1+(1-y)^2)(\frac{x_p^2+z^2}{(1-x_p)(1-z)}+2(x_p z+1)) \\
&\quad -4(2-y)\sqrt{1-y}\sqrt{\frac{x_p z}{(1-x_p)(1-z)}}(x_p z+(1-x_p)(1-z))\cos\phi \\
&\quad +4x_p(1-y)z\cos 2\phi] \qquad (1.12)
\end{aligned}$$

$$\begin{aligned}
L_{\mu\nu}M^{\mu\nu}_{gq} &= \frac{64\pi}{3}\alpha_s Q^2\frac{1}{y^2}[(1+(1-y)^2)(\frac{x_p^2+(1-z)^2}{(1-x_p)z}+2(x_p(1-z)+1)) \\
&\quad +4(2-y)\sqrt{1-y}\sqrt{\frac{x_p(1-z)}{(1-x_p)z}}(x_p(1-z)+(1-x_p)z)\cos\phi \\
&\quad +4x_p(1-y)(1-z)\cos 2\phi] \qquad (1.13)
\end{aligned}$$

$$\begin{aligned}
L_{\mu\nu}M^{\mu\nu}_{q\bar{q}} &= 8\pi\alpha_s Q^2\frac{1}{y^2}[(1+(1-y)^2)(x_p^2+(1-x_p)^2)\frac{z^2+(1-z)^2}{z(1-z)} \\
&\quad -4(2-y)\sqrt{1-y}\sqrt{\frac{x_p(1-x_p)}{z(1-z)}}(1-2x_p)(1-2z)\cos\phi \\
&\quad +8x_p(1-x_p)(1-y)\cos 2\phi] \qquad (1.14)
\end{aligned}$$

Similar to the zeroth order process, we get an expressions of the type $A+B\cos\phi+C\cos 2\phi$ where the ϕ dependence comes from the multiplication of $\tilde{p}_\perp$ with $\tilde{k}_\perp$ whenever p_2 or p_3 is multiplied with $p_{e'}$ or $p_{l'}$. For QCD-Compton, comparing eqn. (1.12) for the quark with (1.13) for the gluon, we see that changing z to $1-z$ brings us from one to the other, except for a change of sign of the $\cos\phi$ term. This means that the quark and the gluon have the same ϕ-distribution except for a phase-shift of 180°. By looking at eqn. (1.12) we also notice that all terms in the $\cos\phi$ dependence are always positive, and the minus sign in front of them all thus means that the quark prefers to be 180° away from the scattered lepton. For the BGF process (eqn. (1.14)) we see that the expression is perfectly symmetric when changing z to $1-z$. The singularities $x_p = 1$, $z = 1$ and $z = 0$ are avoided by requiring a non-zero mass of the final state, which keeps x from being equal to ξ (see eqn. (1.2) and (1.8)) and thus x_p from being equal to 1, and by requiring a reasonable energy sharing between the two final partons. In practice, all these singularities are avoided when a minimum transverse momentum of the two final partons are required, since $p_\perp = \sqrt{z(1-z)(1-x_p)/x_p}$.

To investigate the size of the azimuthal asymmetry and how it varies with x and Q^2, and with $p_\perp$ of the final state partons, we have to integrate over x_p and z. The proton structure function must then be included since it depends on x_p and an analytic calculation is no longer possible. Instead a Monte Carlo event generator, LEPTO 6.1 [10], has been used, giving the asymmetry distributions shown in fig. 1.6 and 1.7, and the corresponding average values of $\cos\phi$ and $\cos 2\phi$ in table 1.1 and 1.2, for a pure sample of QCD-Compton and BGF, respectively. The various results are extracted for different 'points' in the x,Q^2 plane, equally distributed within the region where a reasonable reconstruction of the kinematics is possible. The exact values of these 'points' are given in the tables.

Only first order processes have been simulated, without any intrinsic transverse momentum of the initial parton, and no higher order corrections using parton showers (PS) where included. The only requirement on the final matrix element partons of the generated events was that their transverse momentum, in the hadronic cms, had to exceed 4 *GeV*. Since LEPTO uses a cut off against divergencies defined in terms of the invariant masses of parton pairs, m_{ij}, the relation between this cut off and the $p_\perp$ of the final state partons must be clarified. $p_\perp = \sqrt{z(1-z)\hat{s}}$ where $\hat{s}$ is the invariant mass squared of the two final state partons from the ME, p_2 and p_3. This means that the maximum value of $\sqrt{\hat{s}}$ (or m_{ij}), above which we must generate first order events, is 8 *GeV*. This corresponds at $z = 0.5$ to ME partons with a transverse momentum of 4 *GeV* and for other z-values to partons that could have even less transverse momenta. The entire phase space for events with ME partons of $p_\perp > 4$ *GeV* is thus guaranteed and the cut-off in $p_\perp$ can safely be made.

Figure 1.6 clearly shows the different ϕ-distributions of quarks and gluons in the QCD-Compton process and, as was predicted by the calculations, the quark tends to be scattered 180° away from the scattered lepton. What is also seen is that the dominant dependence is on $\cos\phi$ and the average values of $\cos\phi$ and $\cos 2\phi$ seem to have their maximum for medium values of Q^2 and x. It agrees with results in [11], showing that the maximum averages are achieved when the transverse momentum of the jets ($p_\perp$) is approximately $Q/2$. In our case the average values are maximized at $Q^2 \approx 120$ GeV^2, which corresponds to transverse momenta of about 5 *GeV*. This is consistent with a $p_\perp$ distribution starting at 4 *GeV* and which is rapidly falling.

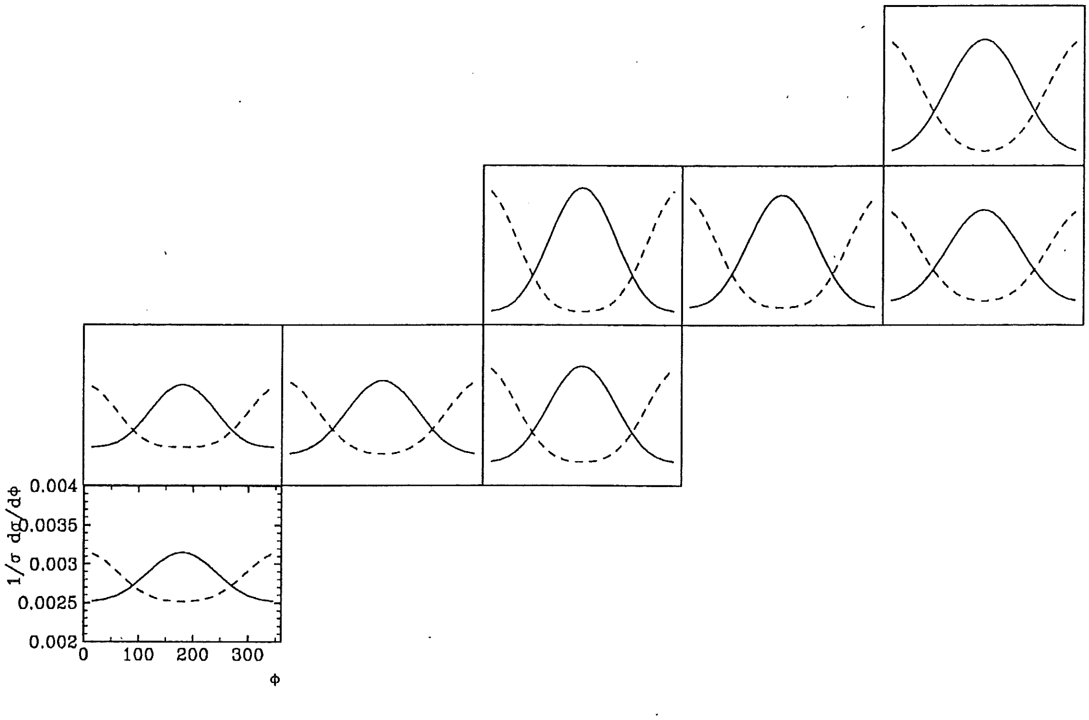

Figure 1.6: *Azimuthal angle distributions for the QCD-Compton process (q = full line, g = dashed line) at different values of x and Q^2. The exact x and Q^2 values are those given in table 1.1.*

$x \backslash Q^2$	12	40	120	400	1200
0.4					$\mp 12.6/1.8$
0.04			$\mp 13.9/3.0$	$\mp 12.7/2.6$	$\mp 10.3/1.7$
0.004	$\mp 7.0/1.6$	$\mp 8.3/1.3$	$\mp 10.8/2.1$		
0.0004	$\mp 5.7/1.0$				

Table 1.1: *Average values of* $\cos\phi / \cos 2\phi$ *(multiplied by a factor* 100*) for the QCD-Compton process at various values of* x *and* Q^2*.*

In the case of BGF, fig. 1.7, a clear $\cos 2\phi$ dependence is seen. The $\cos\phi$ term is exactly zero since the $(1-2z)$ term in eqn. (1.14) becomes zero when we integrate symmetrically around $z = 0.5$. Qualitatively, the variation of $< \cos\phi >$ and $< \cos 2\phi >$ with x and Q^2 is similar to the QCD-Compton process, see table 1.2.

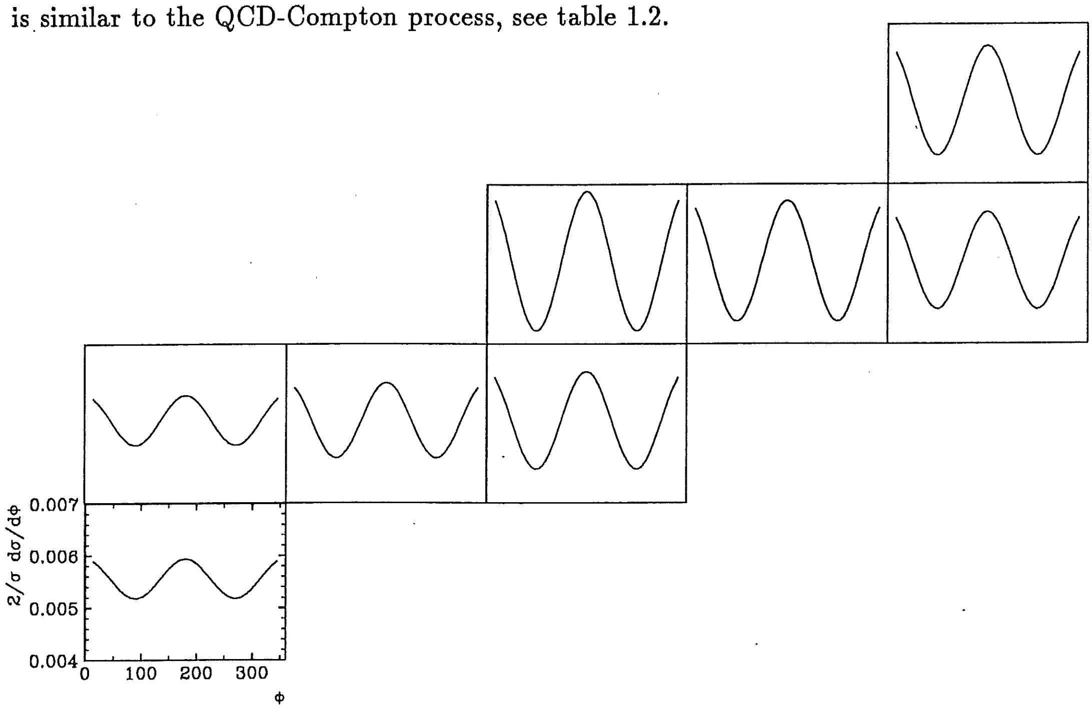

Figure 1.7: *Azimuthal angle distributions for the Boson Gluon Fusion process at different values of* x *and* Q^2*. The exact* x *and* Q^2 *values are those given in table 1.2.*

$x \backslash Q^2$	12	40	120	400	1200
0.4					0/9.3
0.04			0/11.8	0/10.2	0/8.2
0.004	0/4.3	0/6.4	0/8.3		
0.0004	0/3.4				

Table 1.2: *Average values of* $\cos\phi / \cos 2\phi$ *(multiplied by a factor* 100*) for the BGF process at various values of* x *and* Q^2*.*

From an experimental point of view, there is no possibility, yet, to distinguish between QCD-Compton and BGF processes. We should therefore investigate what can be done with a naturally mixed sample, and also when no distinction is made between quark and gluon jets. This means, first of all, that the $\cos\phi$ dependence vanishes completely since both the parton with energy fraction z and the one with $1-z$ enters the expressions. Another way of explaining this is based on the fact that the two final state partons have an azimuthal opening angle of 180°, and if both jets are considered, the $\cos\phi$ dependence is of course gone. The results using a naturally mixed sample of QCD-Compton and BGF processes are shown in fig. 1.8 and table 1.3. Again, the variation of $<\cos\phi>$ and $<\cos 2\phi>$ with varying x and Q^2 is similar to the one obtained for the individual processes.

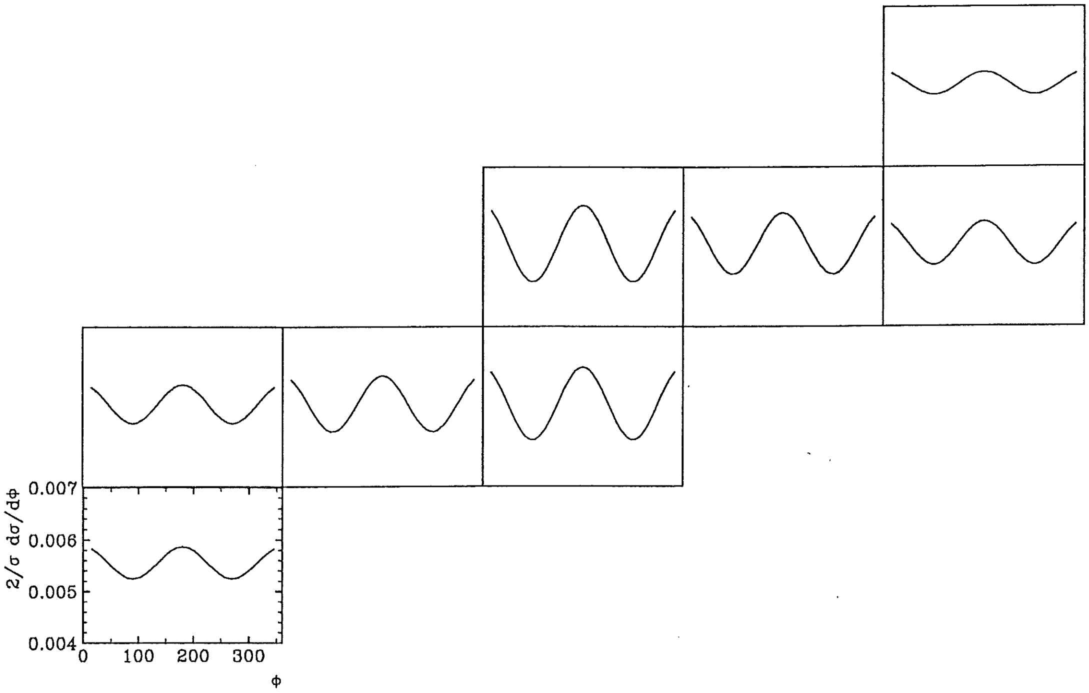

Figure 1.8: *Azimuthal angle distributions for a mixed sample of QCD-Compton and Boson Gluon Fusion processes at different values of x and Q^2. The exact x and Q^2 values are those given in table 1.3.*

$x\backslash Q^2$	12	40	120	400	1200
0.4					0/1.9
0.04			0/6.5	0/5.2	0/3.7
0.004	0/3.3	0/4.7	0/6.2		
0.0004	0/2.8				

Table 1.3: *Average values of $\cos\phi/\cos 2\phi$ (multiplied by a factor 100) for an inclusive sample of QCD-Compton and BGF processes at various values of x and Q^2.*

An alternative way to observe the azimuthal asymmetries is to study only the most energetic jet in each event. This corresponds to selecting the parton with a z value above 0.5 in the expressions (1.12-1.14). The results are shown in fig. 1.9 where the full line represents the asymmetry of the most energetic jet for the QCD-Compton process and the dashed line for the BGF process.

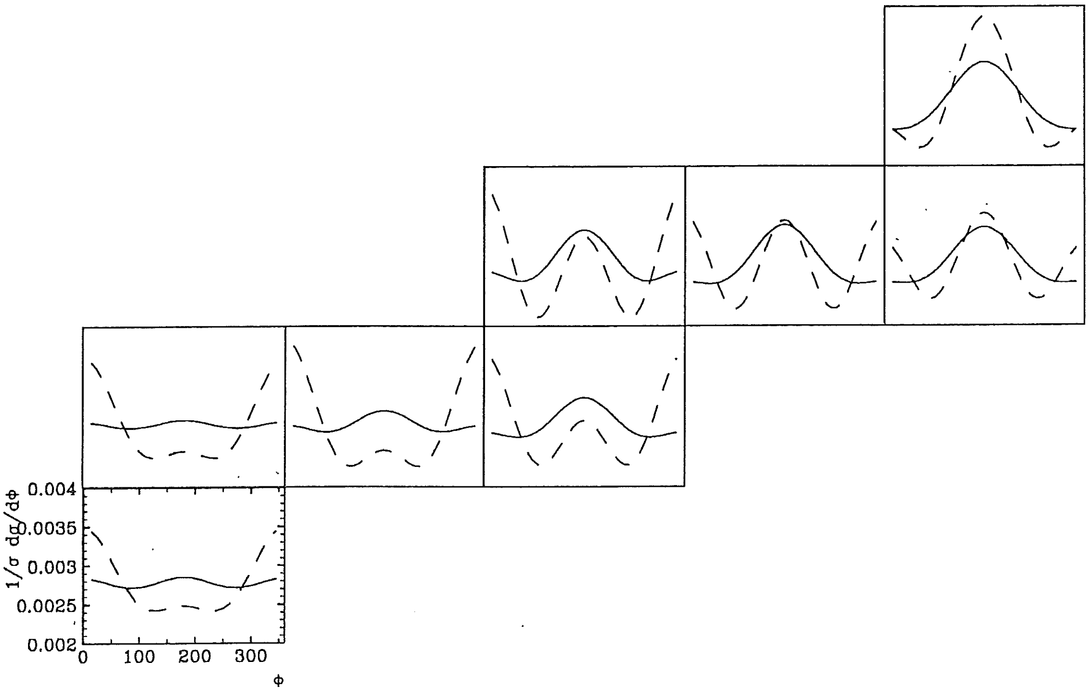

Figure 1.9: *Azimuthal angle distributions for the most energetic jet in QCD-Compton processes (full line) and BGF processes (dashed line), at various values of x and Q^2. The exact x and Q^2 values are given in table 1.4 and 1.5.*

$x \backslash Q^2$	12	40	120	400	1200
0.4					$-7.7/1.8$
0.04			$-4.3/3.0$	$-6.3/2.7$	$-6.2/1.7$
0.004	$-0.4/1.6$	$-1.1/1.4$	$-3.5/2.1$		
0.0004	$-0.4/1.0$				

Table 1.4: *Average values of $\cos\phi/\cos 2\phi$ (multiplied by a factor 100) for the QCD-Compton process when selecting the most energetic jet, at various values of x and Q^2.*

$x\backslash Q^2$	12	40	120	400	1200
0.4					−12.3/9.3
0.04			5.8/11.8	0.5/10.2	−2.7/8.2
0.004	10.1/4.3	12.2/6.4	7.4/8.3		
0.0004	9.1/3.4				

Table 1.5: *Average values of* $\cos\phi/\cos 2\phi$ *(multiplied by a factor* 100*) for the BGF process when selecting the most energetic jet, at various values of* x *and* Q^2*.*

In QCD-Compton events, the jet with highest energy is in most cases the jet originating from the quark. (The gluon is created in a bremsstrahlung like process and has therefore normally less energy than the quark.) One would therefore expect the azimuthal distribution of the most energetic jet in QCD-Compton processes to look primarily like the distribution from quarks, a $-\cos\phi$ distribution, see fig. 1.6. At high values of x and Q^2, the clear $-\cos\phi$ dependence observed is consistent with the high energy jet being a quark but at low values of x and Q^2, just a weak $\cos 2\phi$ dependence is visible. The explanation for this might be referred to the fact that the selected quarks, but especially the gluons, with $z > 0.5$ do not exhibit the same azimuthal distribution as quarks and gluons when no restrictions with respect to z is given.

For BGF processes, the $\cos\phi$ dependence in expression (1.14) tells us that for low values of x, generally corresponding to low values of x_p, the term $(1-2x_p)$ is positive and since the term $(1-2z)$ is always negative when we select jets where $z > 0.5$, we expect to see a $+\cos\phi$ dependence. At high values of x, on the other hand, the sign of the term $(1-2x_p)$ gets reversed and a $-\cos\phi$ dependence should be visible. This is also observed in fig. 1.9.

Again, trying to be realistic, one should investigate what can be measured with a naturally mixed sample of QCD-Compton and BGF processes. The asymmetries obtained from such a sample look very promising, see fig. 1.10. At low values of x and Q^2, where the cross section for these processes are the largest, a relatively strong $\cos\phi$ dependence can be seen with just a weak $\cos 2\phi$ dependence superimposed. A $\cos\phi$ dependence is easier to measure than a $\cos 2\phi$ dependence since the azimuthal angles do not have to be measured as accurately.

$x\backslash Q^2$	12	40	120	400	1200
0.4					−7.7/1.8
0.04			−0.6/6.5	−4.1/5.0	−5.4/3.8
0.004	6.5/3.1	7.7/4.8	3.5/6.2		
0.0004	6.7/3.1				

Table 1.6: *Average values of* $\cos\phi/\cos 2\phi$ *(multiplied by a factor* 100*) for an inclusive sample of QCD-Compton and BGF processes when selecting the most energetic jet, at various values of* x *and* Q^2*.*

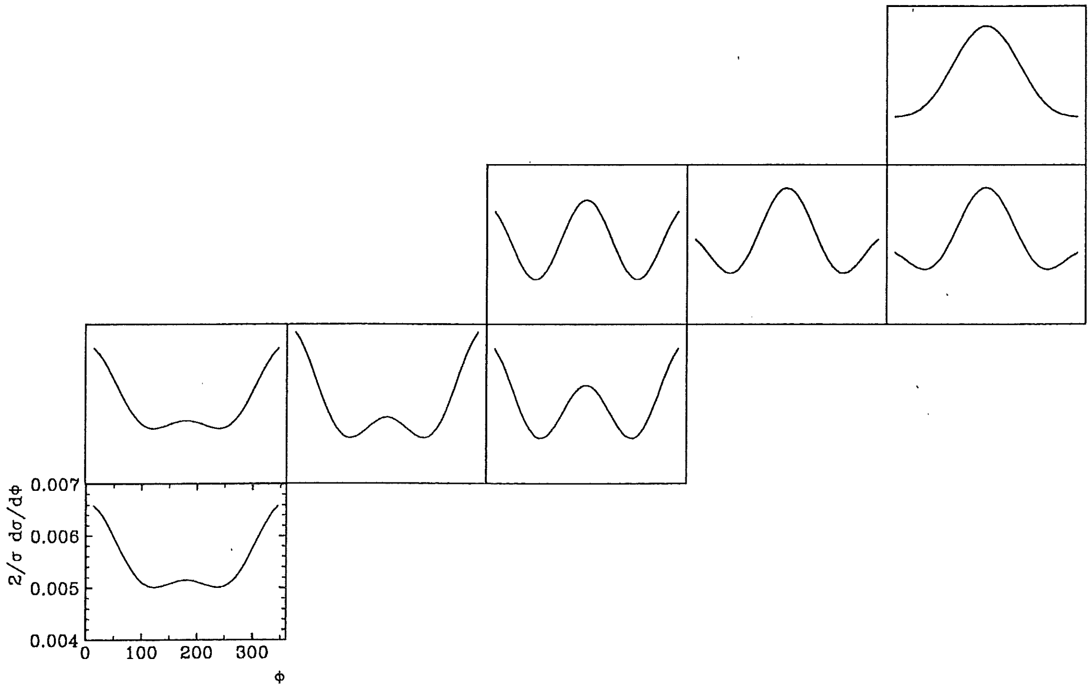

Figure 1.10: *Azimuthal angle distributions for the most energetic jet in a mixed sample of QCD-Compton and BGF processes, at various values of x and Q^2. The exact x and Q^2 values are given in table 1.6.*

1.6 Summary and outlook from the theory

A first remark from the theory describing the azimuthal asymmetries is that it is preferably studied in a frame where the exchanged boson collides head on with the proton, as for instance in the hadronic cms. A transformation of the entire event is therefore necessary, and this transformation can be defined from the reconstructed event kinematics. In the transformation, the azimuthal angles of the particles are only affected by the transverse boost which is defined by $(-\sqrt{Q^2(1-y)}\cos\phi_l, -\sqrt{Q^2(1-y)}\sin\phi_l)$. Therefore not only a good reconstruction of Q^2 and y, but also of the azimuthal angle of the scattered electron, is needed.

A second remark is that the final state parton directions must be well reconstructed through the hadron jets, to enable a determination of their azimuthal angles with respect to the scattered electron. This problem has been thoroughly studied and is presented in appendix B, where also the important problem of making an experimentally reasonable definition and separation of zeroth and first order processes is considered.

An investigation of the asymmetry of QCD-Compton processes is in principal possible. For instance if one chooses to look at events at very high values of x and Q^2, a quite pure sample of QCD-Compton can be held, and methods to distinguish quark from gluon jets also exist. These issues are discussed in appendix A and C. Due to lack of statistics, this is something for the future since the dominant cross section is at low values of x and Q^2.

A more realistic study is the asymmetry of a mixed sample of QCD-Compton and BGF processes in a region of x and Q^2 where the cross section is high enough to provide reasonable statistics with a limited integrated luminosity. What also has to be considered however, is where in x and Q^2 an asymmetry of a measurable size is achieved. Since the maximum values of $< \cos\phi >$ and $< \cos 2\phi >$ are obtained when the transverse momentum of the jets equals $Q/2$, and a transverse momentum of at least 4 GeV is required to get reasonable jet reconstruction, events at $Q^2 \approx 100$ GeV^2 are preferred. The accuracy of a measurement based on a limited data sample thus depends on both the total cross section (A) in a specific region of x and Q^2, and on the size of the asymmetry, (B) and (C), and this dependence can be approximated as $(B^2 + C^2)/A$. Therefore the values of the average $\cos\phi$ $(B/2A)$ and $\cos 2\phi$ $(C/2A)$ to some extent give a hint to where in x and Q^2 an azimuthal angle dependence can most easily be measured.

When it comes to the asymmetry associated with the transverse momentum of the initial parton, 'the zeroth order type of asymmetry', the normal statement is that the small transverse momenta connected with the Fermi motion guarantee a negligible influence on the 'first order asymmetry'. If, however, higher order corrections, as for instance initial state gluon radiation, is taken into account, the transverse momentum of the initial parton can have accumulated to several GeV. The influence might then no longer be negligible. An 'operational' event definition that selects 'appropriate' events will then help. Firstly, if 2+1 jet events are required, having jets with transverse momenta exceeding 4 GeV, events where a hard emission has occurred are selected. Secondly, if these two jets, measured in the hadronic cms, are reasonably back-to-back in the azimuthal plane, we are assured that influences from higher order corrections are small. This can be understood from the fact that if the initial state parton emits gluons, it will have a transverse momentum when it interacts with the exchanged boson and this transverse momentum is transferred to the final state partons. The transverse momentum sum of the two final state partons is thus a direct measurement of the amount of initial state radiation. Events where the two jets are too much deflected from an azimuthal back-to-back situation should thus be discarded. Another approach to solve this problem would be to measure the azimuthal angles in the jet-jet cms. In this system the exchanged boson will collide head on with the initial parton, irrespective of whether initial state radiation has occurred or not. This approach is however left for a future study.

Further potential possibilities of an azimuthal asymmetry measurement is an estimate of the fraction of QCD-Compton and BGF processes at various regions of x and Q^2, since the size of the $\cos\phi$ and $\cos 2\phi$ asymmetry depends on their relative contributions. It might also be used to investigate the content of the colorless Pomeron in diffractive events. Methods to collect a quite pure sample of diffractive events are at hand, and if the Pomeron consists of a bunch of gluons, $2 + 1$ jet diffractive events should exhibit an azimuthal cross section dependence similar to that of the BGF process. Before this can be done reliably, the azimuthal asymmetry should be thoroughly studied and understood in 'ordinary' QCD events, as attempted in this thesis.

Chapter 2

HERA and the H1 detector

The HERA accelerator complex and the H1 detector is described, with the emphasis on the detector parts of relevance for the asymmetry study presented in this thesis. This means concentrating on detector elements needed in the selection of DIS neutral current events and on the calorimeter which is used in the reconstruction of jets.

2.1 HERA

The Hadron-Elektron-Ring-Anlage, HERA [12], is the world's first electron proton collider and was completed in 1991. It consists of two independent accelerators with a circumference of 6.3 *km*, which are designed to store 30 *GeV* electrons and 820 *GeV* protons respectively. The two beams collide head on at two interaction points which are surrounded by the H1 and the Zeus detector, and the first collisions were observed in the spring of 1992. The main parameters of HERA can be found in table 2.1, where the design values are given together with the values of 1993, the year that the data sample of this analysis was collected.

	Design		1993		unit
	p-ring	e-ring	p-ring	e-ring	
Energy	820	30	820	26.7	GeV
Luminosity	1.5×10^{31}		1.3×10^{30}		$cm^{-2}s^{-1}$
Integrated luminosity per year	10^5		600		nb^{-1}
Magnetic field	4.68	0.165	4.68	0.149	T
Number of bunches	210	210	90	90	
Bunch separation	96	96	96	96	ns
Injection energy	40	14	40	12	GeV
Filling time	20	15			min

Table 2.1: *The main parameters of HERA.*

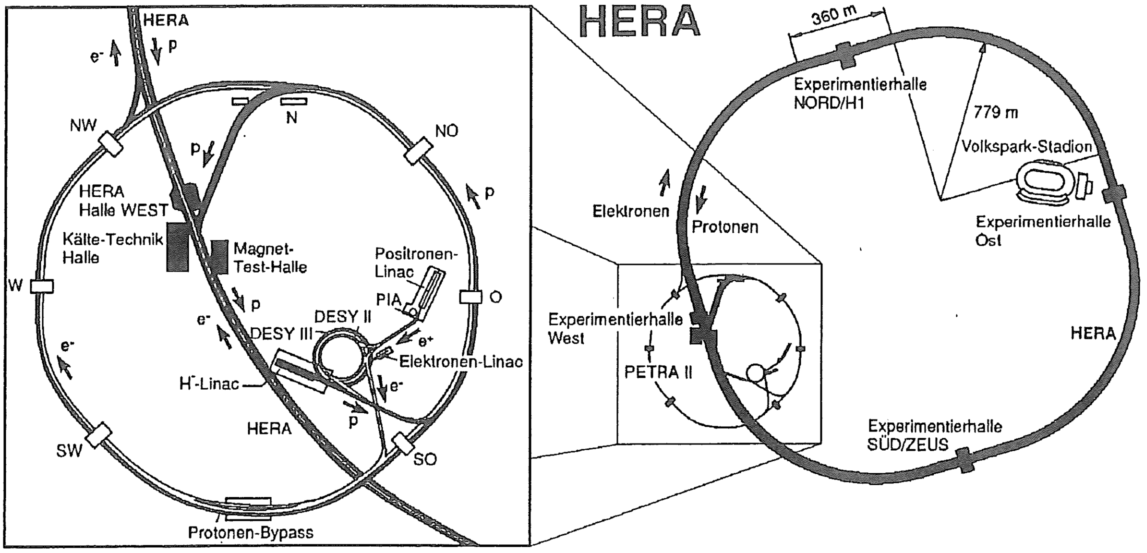

Figure 2.1: *The HERA accelerator complex.*

The acceleration of the electrons and protons up to their final energies is a very complicated procedure involving several accelerators, depicted in fig. 2.1. Electrons from a 450 MeV linear accelerator, LINAC II, are injected into DESY II where they are accelerated to 7 GeV, after which they are transferred to PETRA II. In PETRA they are accumulated in 70 bunches, accelerated to 13 GeV and then transferred to the HERA ring where the final acceleration is made. This is repeated twice until HERA has been filled with 210 bunches. The steering and focusing of the electron beam is performed with conventional magnets.

The acceleration of the proton beam is even more complicated. Negatively charged hydrogen ions are accelerated to 50 MeV in a linear accelerator, LINAC III, and injected into DESY III where the electrons are stripped off. The protons are then accelerated to 7.5 GeV and transferred to PETRA II where 70 bunches are accumulated and again accelerated , now to 40 GeV. The filling of HERA is then, as with the electrons, repeated until one gets 210 bunches of protons, and the final acceleration to 820 GeV is performed in the HERA ring. In order to keep the protons in a circular orbit at 820 GeV, the dipole bending magnets must produce a magnetic field of 4.7 T. This is achieved with superconducting magnets cooled to 4.5 K with liquid helium. The quadrupole focusing magnets are also superconducting.

2.2 The H1 detector

In fig. 2.2 a schematic 3D-view of the H1 detector [13] is shown. The protons enter from the right and the electrons from the left. Since the protons have a much higher momentum than the electrons, the cms of the colliding particles will move along the proton beam direction and most of the particles produced will hit the detector parts in the forward region. This explains the asymmetric design with a higher instrumentation in the proton direction.

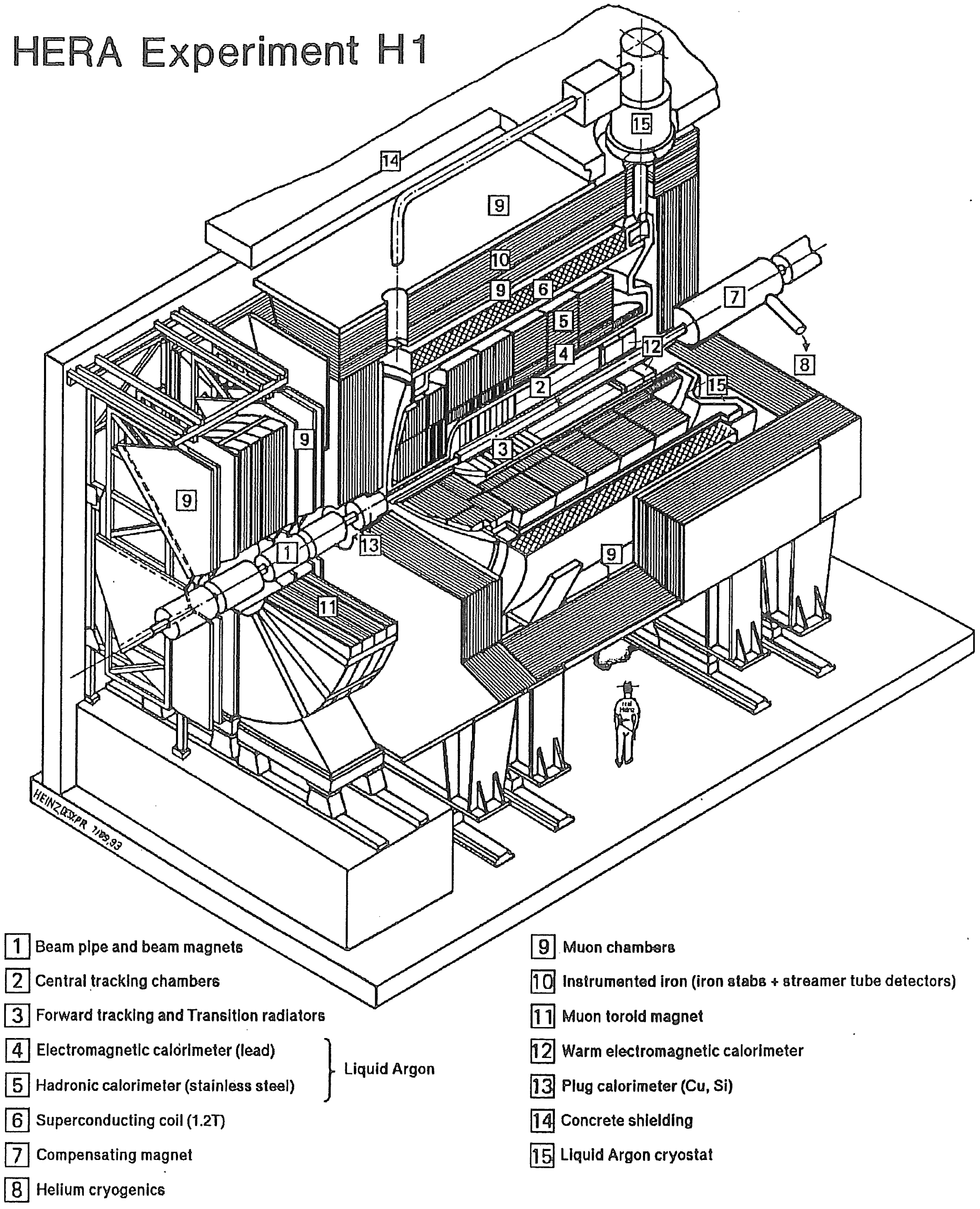

Figure 2.2: *The H1 detector.*

Starting from the interaction point and moving outwards, the detector consists of a central and forward tracking system, the liquid argon and backward calorimeters, a superconducting magnetic coil, the instrumented iron, and the forward muon spectrometer which is located as a separate unit in the forward direction.

2.2.1 Tracking

Because of the many particles being produced at small polar angles, the tracking system is divided into a central and a forward part. The central part, covering a polar angular region of 25° – 155°, consists of two cylindrical jet chambers, proportional chambers and z-chambers. The forward part, covering polar angles between 5° and 30°, is composed of planar chambers, radial chambers and transition radiators, see fig. 2.3.

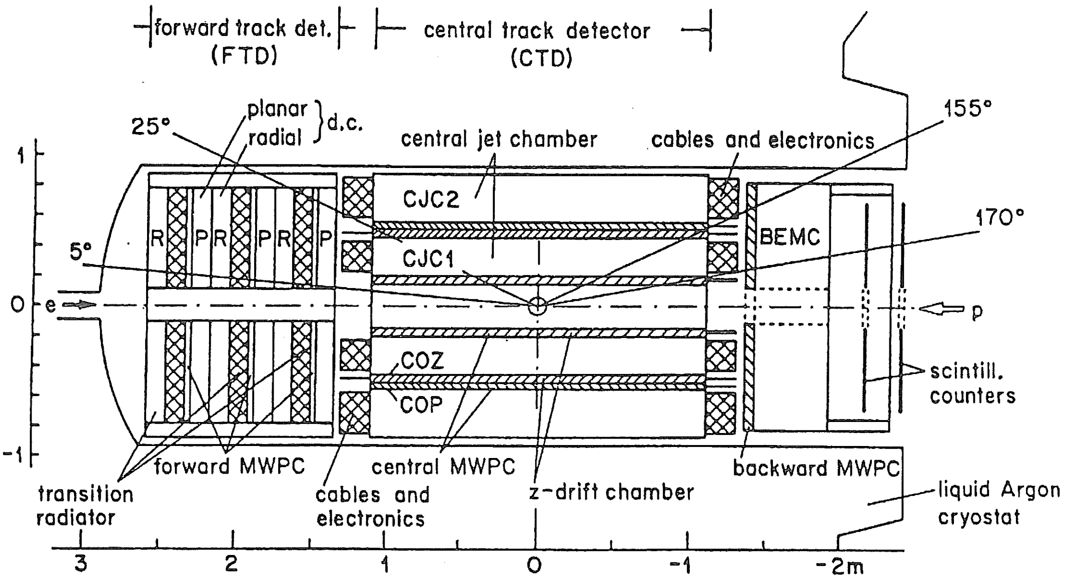

Figure 2.3: *The central and forward tracking system of H1.*

The main task of the inner and the outer central jet chamber (CJC1 and CJC2) is to very accurately measure the track coordinates in the $x - y$ plane, but also to provide a moderate measurement of the z coordinate by the method of charge division along the wires. Particle momenta can be determined with a precision of $\sigma_p/p^2 \approx 0.003\ GeV^{-1}$ and the resolution along the wires parallel to the beam axis is $\sigma_z \approx 22\ mm$. The jet chambers are also used in dE/dx measurements for particle identification, mainly electron identification and rejection of beam gas events by identification of protons. As a complement to the jet chambers, the central inner and outer z-drift chambers (CIZ and COZ) measure the z-coordinate of tracks with a high accuracy, $\sigma_z \approx 0.30\ mm$. Three multiwire proportional chambers (MWPC), the central inner and outer (CIP and COP) and the backward proportional chamber (BPC), are also located in the central tracking area. They are mainly used for triggering since they deliver a fast timing signal with a resolution better than the separation of two succeeding HERA bunch crossings. The BPC, which covers the front surface of the backward electromagnetic calorimeter, is important for the reconstruction of scattered electrons, especially in directions where the drift chambers fail. The BPC provides a space coordinate, which together with the reconstructed vertex defines the scattered electron direction, and it also serves to discriminate between electrons and photons.

The three planar chambers of the forward tracking system are designed to make precise measurements of the polar angle θ of charged particles, whereas the three radial chambers provide accurate measurements of the azimuthal angle ϕ, and a rough estimate of the radial coordinate r. These chambers are interleaved with transition radiators, which together with the radial chambers are used mainly to discriminate between electrons and pions. In the forward region, three multiwire proportional chamber can also be found. Each consists of two wire planes interleaved with three cathod planes, and they are mainly used for triggering purposes.

There are two scintillator systems both located in the backward region: the time of flight system (TOF) at $z \approx -2\ m$ and the two veto walls at $z \approx -6.5\ m$ and $z \approx -8.1\ m$, respectively. The purpose of these is to reject proton beam induced background, the so-called beam-gas and beam-wall events, at the first level trigger, and to monitor the rates after filling and during runs.

2.2.2 Calorimetry

The calorimeter system consists of the liquid argon calorimeter (LAC), the backward electromagnetic calorimeter (BEMC) and the small plug calorimeter (PLUG) in the very forward direction, see fig. 2.4. The system is completed by the instrumented iron which serves as a tail catcher for energy 'leaking' out of the LAC.

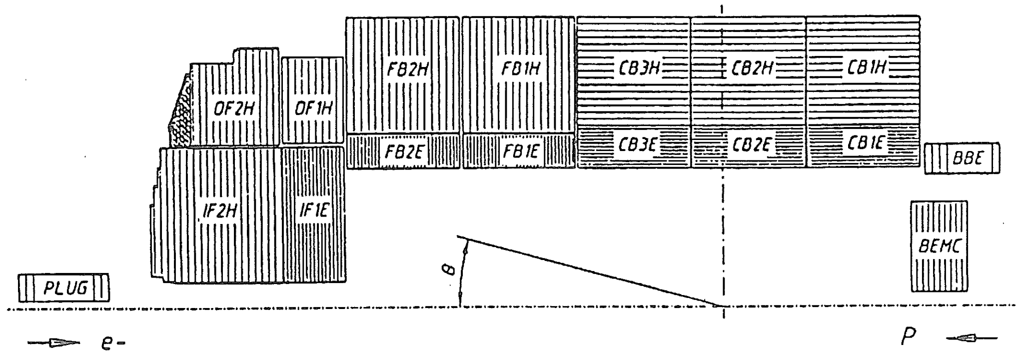

Figure 2.4: *The calorimeter system of H1.*

The liquid argon calorimeter is located inside the magnetic coil to minimize the amount of dead material in front of it and covers the polar angular range from $\theta \approx 4°$ to $\theta \approx 153°$.

It is composed of one hadronic and one electromagnetic part. The absorber material is stainless steel in the hadronic part and lead in the electromagnetic part. Both the steel and the lead plates are separated by gaps for the active medium liquid argon. The electromagnetic part has a total thickness varying between 20 and 30 radiation lengths (X_0) and the depth in terms of interaction lengths (λ) is for the entire LAC between 4.5 and 8. For electrons, the energy resolution is $\sigma_E/E \approx 12\%/\sqrt{E\ GeV} \oplus 1\%$ and for charged pions the resolution has been determined in a test beam to $\approx 50\%/\sqrt{E\ GeV} \oplus 2\%$. The electromagnetic energy scale could be verified to ±8% and for the hadronic scale to ±5%.

The main purpose of the backward electromagnetic calorimeter is to measure the energy and angle of the scattered electron in deep inelastic scattering processes. The BEMC covers the polar angular region from 154° to 176° which corresponds to a region in Q^2 from roughly 5 GeV^2 to 100 GeV^2, see fig 1.2. A sample of events is therefore referred to as a low Q^2 sample when the scattered electron is found in the BEMC and to a high Q^2 sample when the scattered electron is found in the LAC. The 'crack' between the BEMC and the LAC at $\theta \approx 154°$ prevents a continuous measurement over the full polar scattering angles of the electron. The BEMC is made out of lead-scintillator sandwich stacks and the entire structure has a thickness of 22 radiation lengths which, in this case, corresponds to about 1 interaction length. Since there is no hadronic calorimeter in this polar angular region, the tail catcher together with the BEMC is used to measure hadronic energy depositions. The energy resolution is about $10\%/\sqrt{E} \oplus 3\%$ for electrons and about $80\%/\sqrt{E}$ for hadrons. The energy scale in the BEMC is known to about 2%.

The plug calorimeter is designed to close the gap between the forward part of the LAC and the beam pipe and thus covers the region of polar angles from 4° down to 0.7°. It consists of copper absorber plates interleaved with layers of silicon detectors corresponding to 45 radiation lengths and 4 interaction lengths. The energy resolution is of about $150\%/\sqrt{E}$.

The purpose of the tail catcher (a part of the instrumented iron) is to measure energy leaking out of the LAC. It consists of streamer tube layers equipped with readout pads and the total thickness of the tail catcher is 4.5 absorption lengths. It covers the polar angular region from 6° to 172° and has an energy resolution of $\sigma_E/E \sim 100\%/\sqrt{E}$.

2.2.3 Magnet

The superconducting solenoid, operating at 4.5 K, provides a uniform field of 1.15 T parallel to the beam line and pointing in the direction of the proton beam. The purpose of the magnetic field is to bend the trajectory of charged particles, making it possible to determine their charges and momenta. The surrounding iron serves as a flux return yoke for the magnetic field.

2.2.4 Muon system

Apart from the purpose of measuring energy leaking from the LAC, the instrumented iron is also equipped with sixteen streamer tube layers (eleven of them covered with readout pads), to measure both the tracks and the energy of muons. An angular resolution σ_θ of 15 mr is achieved and the momentum resolution is $\sigma_p/p \approx 35\%$.

There is also a muon spectrometer (see appendix D), standing by itself in the forward direction covering the polar angular range $3^\circ \leq \theta \leq 17^\circ$. The detector consists of six drift chamber planes mounted three on each side of a toroidal magnet which provides an average field of 1.6 T. Four out of the six drift chamber planes measure the polar angle θ of traversing muons, and from their deflection in the magnetic field, also the momenta. The other two planes measure the azimuthal angle ϕ. Muons with a momentum between 5 and 200 GeV can be measured. The upper limit is set by the magnetic field strength in the toroid together with the spatial resolution of the drift chambers, and the lower limit is set by the amount of material the muons have to penetrate before hitting the forward muon system. The momentum resolution σ_p/p varies from 0.24 for 5 GeV tracks to 0.36 for 200 GeV tracks.

2.2.5 Trigger

The purpose of the trigger system [14] is to select interesting *ep* collision events and to reject background events. There are three basic types of so-called machine background events: synchrotron radiation from the electron beam and beam gas and beam wall interactions due to the proton beam. As we are interested in deep inelastic neutral current events for these asymmetry studies, there are also 'physics background', consisting of mainly photoproduction and possibly charged current events.

The unique feature which distinguishes the *ep* events from most of the machine background is their origin from the nominal fiducial volume of the *ep* interaction region. The time of flight system provides information on whether particles come from upstreams or from the interaction volume by comparing their arrival time with the HERA clock phase. The central jet chambers and the central and forward multiwire proportional chambers allow for a fast estimation of the vertex position.

In a more sophisticated procedure, the fact that hard scattering events have higher total transverse energy than normal background events can be used since the liquid argon and the backward electromagnetic calorimeter deliver information about the observed energy deposition. Missing total transverse energy signals charged current events, while the requirement of some electromagnetic but no hadronic energy deposited in a given position of the calorimeter spots a scattered electron from a neutral current event. A further natural division of the neutral current events is made based on if the scattered electron is spotted in the backward electromagnetic calorimeter, the low Q^2 sample, or in the liquid argon calorimeter, the high Q^2 sample. The photoproduction events can be identified from a scattered electron in the electron tagger of the luminosity system, indicating an event with a very low value of Q^2, but when the scattered electron remains in the beam pipe, triggering becomes more complicated and the event selection must be completed off-line.

There are four levels of triggers with increasing complexity and allowed decision time. Due to the very short time (96 ns) between two bunch crossings, the information for the first level trigger is stored in a pipeline while a decision is made. All conditions mentioned above are applied in this first level trigger and an expected total interaction rate of $\sim 50 - 100 kHz$ should be reduced to $\sim 1 kHz$.

Then there are two intermediate trigger levels working in parallel. Level 2 is a hardware trigger and should reduce the input rate from $\sim 1kHz$ to about $200Hz$. It uses the same information as level 1 but more sophisticated checks can be undertaken since more time is available. Level 3 is a software based trigger which further reduces the rate to maximum $50Hz$. (During the running of 1993, H1 operated without trigger level 2 and 3.)

At level four, the software filter, the full event information is available and allows for a complete event reconstruction on-line. The rate is reduced to $\sim 5Hz$ before the surviving information is sent to storage media in the computer center.

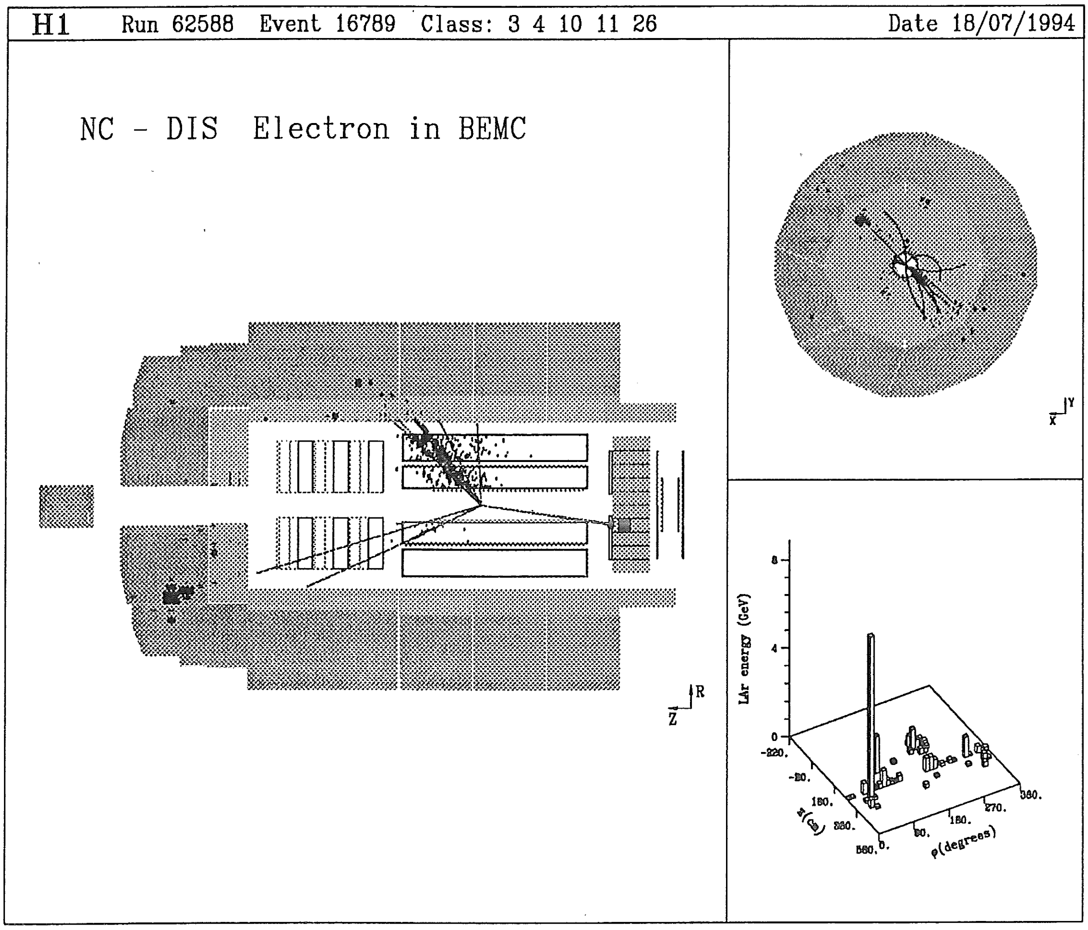

Figure 2.5: *A neutral current deep inelastic* $2+1$ *jet event. The electron is scattered into the BEMC.*

Chapter 3

Analysis

In this chapter the complete analysis of the lepton-hadron azimuthal angle asymmetries of $2+1$ jet events is presented. The various subproblems are described in some detail as a complement to what is presented in appendices B and C on jet reconstruction and jet identification. The azimuthal acceptance in the hadronic cms, which constitutes a complicated problem, is explained in detail, and a solution to the problem is given. The theoretical predictions of a $\cos 2\phi$ dependence when both jets are considered, and mainly a $\cos\phi$ dependence when just the most energetic jet is considered, are verified by the final results.

3.1 Event selection

The event sample used in this analysis was collected in 1993 and corresponds to an integrated luminosity of about 250 nb^{-1}. This sample mainly consists of neutral current deep inelastic scattering events in which the scattered electron is found in the backward electromagnetic calorimeter, the so-called low Q^2 sample. Due to the rapidly decreasing cross section with increasing Q^2, a much smaller fraction comes from the high Q^2 sample where the electron is scattered into the liquid argon calorimeter, and although a considerable asymmetry is expected in this Q^2 range, the present statistics prevents an analysis.

For the low Q^2 sample, the scattered electron is identified as the most energetic electromagnetic cluster in the BEMC, with an associated hit, within 5 cm, from the backward proportional chamber (BPC). The BPC hit defines together with the reconstructed vertex position the scattering angle of the electron. Restrictions for the cluster center of gravity to be well within the limits of the BEMC are given along with similar requirements for the BPC hit. These requirements correspond to an allowed scattering angle of the electron between 157° and 172.5°, when the event vertex lies exactly at the nominal interaction point. This vertex can, however, be considerably shifted, but if the shift in the z direction is more than ± 30 cm, the event is discarded.

To ensure a clean separation of DIS events from photoproduction background, the energy of the scattered electron is required to exceed 14 GeV, see ref. [15]. Another approach to suppress this background is to ensure that the radius of the cluster is less than 5 cm since a 'fake' electron from a photoproduction event is most likely a hadron which in general gives broader showers. The amount of photoproduction background in the final sample is after these cuts completely negligible. To exclude diffractive events which normally give no activity in the forward region, the sum of the calorimetric energy of clusters with a rapidity greater than two must exceed 0.5 GeV, see ref. [16]. This cut reduces the low Q^2 sample by about 5% while the LEPTO generated neutral current DIS events are hardly affected.

Apart from these standard H1 cuts, I have also applied the additional constraints of $Q^2 > 12\ GeV^2$ which matches the polar angle limit of the scattered electron at 172.5°, see fig. 3.1, and only accepted events with $y > 0.03$ which is on the limit of reasonably good y-reconstruction. The reconstruction of y, at low values of y, is not that critical for this analysis since y is only used for the definition of the transverse boost to the hadronic cms in the form $\sqrt{Q^2(1-y)}$. Therefore an error in y, at small values of y, will not have a large impact on the boost. The other two kinematic limitations of the event sample are given by the detector boundaries of the BEMC, $\theta_l > 157°$ which roughly corresponds to $Q^2 < 100\ GeV^2$, and the reduction of the photoproduction background, $E_l > 14\ GeV$ which corresponds to $y < 0.5$, see fig. 3.1.

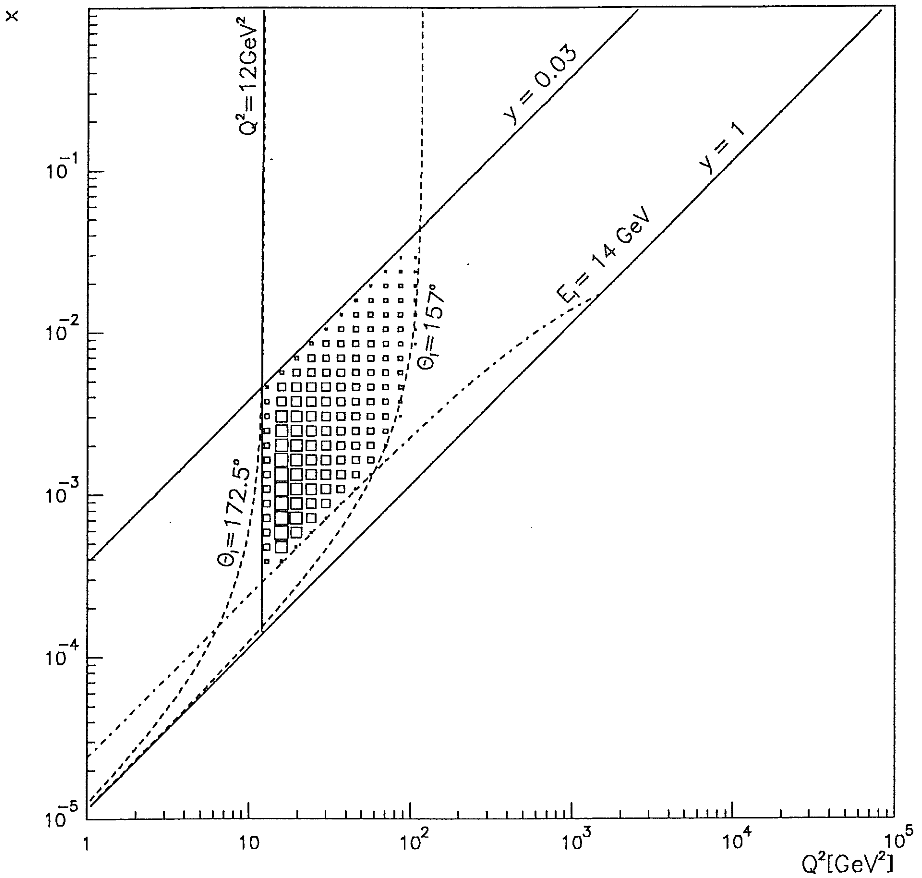

Figure 3.1: *The area in x and Q^2 covered by the selected event sample.*

3.2 Kinematic reconstruction

The reconstructed DIS kinematic variables are first of all used for the selection of events in the analysis, but for the asymmetry studies they are also important for the transformation from the laboratory system to the hadronic center-of-mass system in which the azimuthal angles are defined.

There are several different methods to reconstruct the kinematics of DIS events. As has been already shown, the kinematics of neutral current events can be directly calculated from the measured energy and polar angle of the scattered electron. The relations between the energy and angle of this scattered electron and the kinematic variables are given in eqns. (1.1).

A second method is the so called Jacquet-Blondel method [17] [18] which reconstructs the kinematics from, basically, the hadrons of the current jet:

$$\begin{aligned} y_{JB} &= \frac{\sum_i (E_i - p_{zi})}{2E_e} \\ Q^2_{JB} &= \frac{(\sum_i p_{xi})^2 + (\sum_i p_{yi})^2}{1 - y_{JB}} \end{aligned} \tag{3.1}$$

where $(E_i, p_{xi}, p_{yi}, p_{zi})$ is the four vector of hadron i and the sum runs over all final state hadrons. A third method is the Double Angle method [18] which uses information from both the scattered electron measurement and the hadronic final state:

$$\begin{aligned} \cos\gamma &= \frac{Q^2_{JB}(1 - y_{JB}) - 4E_e^2 y_{JB}^2}{Q^2_{JB}(1 - y_{JB}) + 4E_e^2 y_{JB}^2} \\ Q^2_{\theta\gamma} &= \frac{4E_e^2 \sin\gamma(1 + \cos\theta_l)}{\sin\gamma + \sin\theta_l - \sin\theta_l + \gamma} \\ y_{\theta\gamma} &= \frac{\sin\theta(1 - \cos\gamma)}{\sin\gamma + sin\theta - sin\theta + \gamma} \end{aligned} \tag{3.2}$$

where γ represents the angle of the current jet. These three methods are complementary in the sense that they provide good precision in the reconstruction in different regions of the total kinematic range covered by HERA. Fig. 3.2 shows the relative errors of the reconstructed Q^2 and y for events from the low Q^2 sample. In the Jacquet-Blondel and the Double Angle methods, only the calorimeter clusters were used. No information from the tracking devices was included. As can be observed, the electron method in general gives the best results although the tails of the y-reconstruction are very long. Since these results are based on the complete low Q^2 sample, $1 + 1$ jet events dominate. However, in the final sample of this asymmetry study, $2 + 1$ jet events have been selected and the tails in the y-reconstruction using the electron method are for this sample strongly reduced. The electron method was therefore chosen for the reconstruction of the kinematic variables. A comparison of the Q^2 and y distributions from data with those from the detector simulated LEPTO generated events, shows good agreement, see fig. 3.3, giving average values in the final sample of: $< Q^2 >= 27\ GeV^2$ and $< y >= 0.15$.

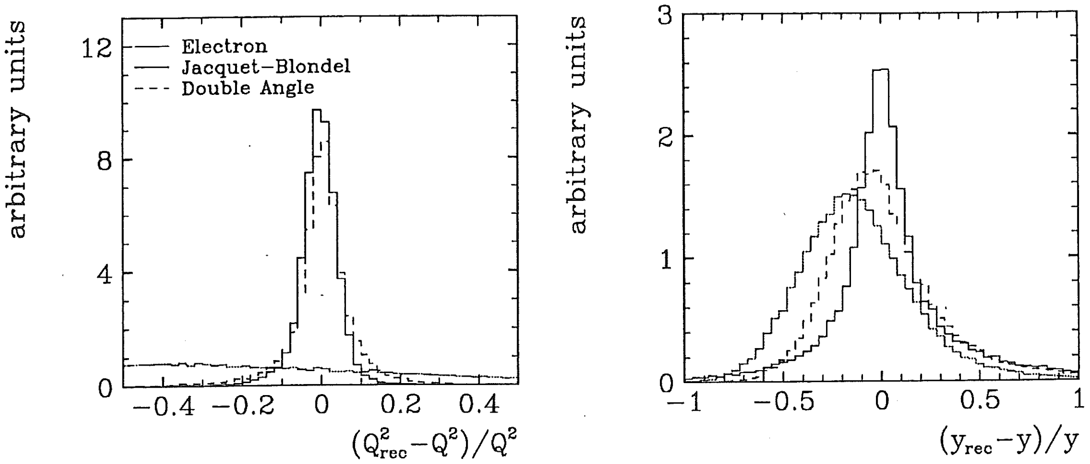

Figure 3.2: *Relative errors in the reconstructed Q^2 and y values, based on the electron measurement (full line), the Jacquet-Blondel method (dotted line) and the Double Angle method (dashed line).*

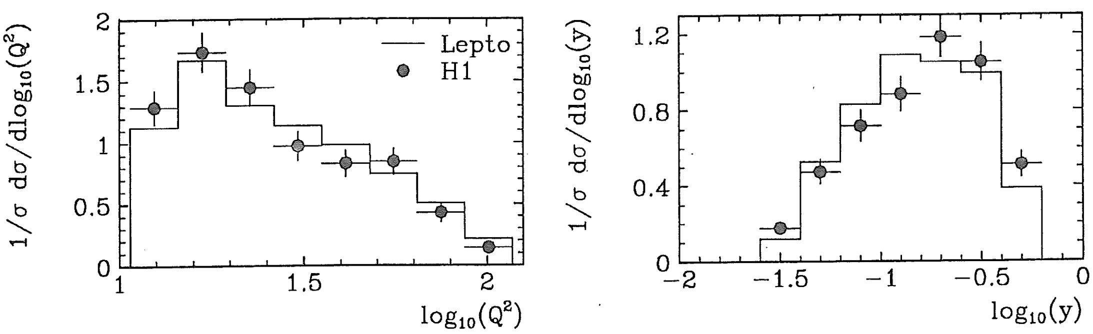

Figure 3.3: *Comparison of the Q^2 and y distributions obtained from data with the ones using the* LEPTO *event generator.*

3.3 Transformation to the hadronic cms

The transformation from the laboratory system to the hadronic center-of-mass system can be defined from the reconstructed kinematics of each event. In the hadronic cms the vector sum of the incoming proton and the exchanged boson is zero and therefore this vector sum, calculated in the laboratory frame, defines the transformation. The direction of the transverse boost is given by the azimuthal angle of the scattered electron (ϕ_l) and thus the complete transformation vector becomes:

$$P + q = \left(E_p + yE_e - \frac{Q^2}{4E_e}, -\sqrt{Q^2(1-y)}\cos\phi_l, -\sqrt{Q^2(1-y)}\sin\phi_l, E_p - yE_e - \frac{Q^2}{4E_e}\right) \tag{3.3}$$

The four vector of the proton is known and the four vector of the exchanged boson is calculated from the incoming and scattered electron according to eqn. (1.3). The coordinate system in the hadronic cms is defined in such a way that the +z-direction is given by the incoming proton direction and the scattered electron lies in the xz-plane. Thus the azimuthal angles of the jets is always measured with respect to the scattered electron.

How well the transformation vector can be reconstructed is shown in fig. 3.4 where the absolute error in the azimuthal angle of the scattered electron (ϕ_l) and the relative error of the transverse boost component (P_t) is plotted. Also the correlation plot of the relative error in the x and y component of the boost vector is shown in fig. 3.4c where the distribution along the diagonal indicates that the most severe errors are connected with the reconstruction of Q^2 and y, i.e. with the size of the transverse boost, and not with the direction of the transverse boost, see eqn. (3.3). The longitudinal component of the boost vector does not, as mentioned, directly influence the azimuthal angles of the jets, but is in any case very well reconstructed.

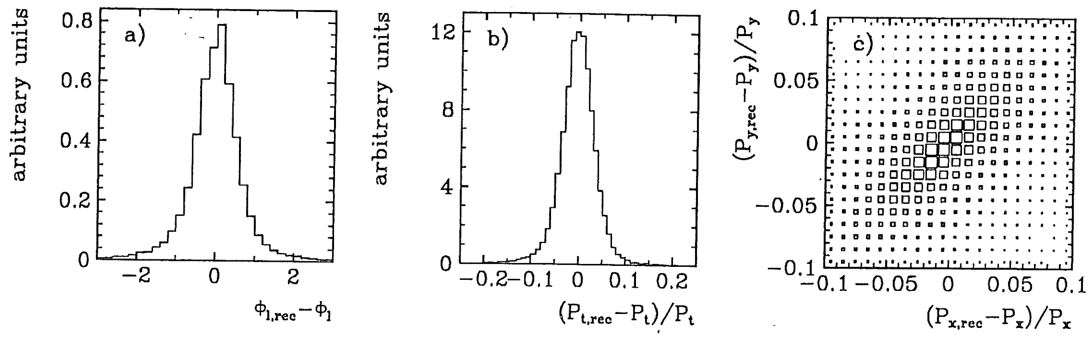

Figure 3.4: *Reconstruction of the transformation vector to the hadronic cms. a) Absolute error in the azimuthal angle of the scattered electron. b) Relative error in the transverse boost component. c) Relative error in the y- versus the x-component of the boost vector.*

3.4 Jet reconstruction

A complete study of how to reconstruct jets at the ep-collider HERA is described in appendix B. The problem of how to deal with the very energetic spectator jet is described and a comparison of five different jet algorithms with respect to their ability of reconstructing the underlying hard parton emission is investigated.

For the asymmetry study we used two different jet algorithms. One was a cone type of algorithm [19] with a cone size, defined as $\Delta R = \sqrt{\Delta\eta^2 + \Delta\phi^2} = 1$. A transverse energy of at least 3.5 *GeV* inside the cone was required, according to the results in appendix B. This type of jet algorithm performs well in the sense that it provides a very good reconstruction of the ME parton four vectors and gives a good separation between zeroth and first order processes, regardless of event kinematics. The other jet algorithm used was LUCLUS [20] which also exhibited similar performance in the jet study. When using LUCLUS an inclusion of a pseudoparticle to account for the lost fractions of the proton remnant in the beam pipe is necessary, see [22], and the cut-off parameter d_{join} was set to 4.0 GeV, in accordance with results in appendix B.

The reconstruction of jets was made in the hadronic cms using calorimeter clusters only. Clusters from the liquid argon calorimeter, having a polar angle coverage from roughly 4° to 157°, were used. At larger angles, up to 176°, the hadron energy has to be measured from the backward electromagnetic calorimeter and the tail catcher, since there is no hadronic calorimeter in this region.

In fig. 3.5a the jet multiplicity obtained using the LEPTO event generator and real data is compared. In the selection of $2+1$ jet events, the required jet multiplicity is two for the CONE algorithm since the spectator jet is not reconstructed, while the LUCLUS algorithm should find three jets including the spectator jet. Both algorithms show a certain disagreement between the data and Monte Carlo and this is probably due to the non-default parameter settings used in LEPTO, see [21]. The LEPTO generator is based on QCD matrix element calculations up to the first order in α_s, and the inclusion of parton showers accounts for higher order processes. $2+1$ jet events is thus in general generated using the ME calculations to first order, but could also in principal originate from a zeroth order simulation where the added parton showers account for the second jet. Since the azimuthal angle asymmetries of $2+1$ jet events are correctly described only when the first order ME calculations have been used, it is crucial that the reconstructed $2+1$ jet events originate from a simulation using these first order ME calculations to the greatest possible extent.

The QCD matrix element gives divergences for soft and collinear emission which is technically avoided by defining a smallest invariant mass, m_{ij} of the created parton pairs. The normal implementation of this mass cut is through a cut parameter, y_{cut}, which is defined by $m_{ij}^2 \geq y_{cut} W^2$ and thus results in a correlation between m_{ij} and W. Depending on the choice of y_{cut}, m_{ij} might vary between masses close to the divergence limit at low W and very high values at high W. This will thus result in high m_{ij} cuts at high W values, although jet structures can still be resolved below this cut. In appendix B it is also demonstrated that high values of W do not necessarily correspond to high values of the hard subsystem mass $\sqrt{\hat{s}}$ for $2+1$ jet events. A parametrisation for the cut in m_{ij} which follows the divergence limit with a 2 GeV margin is therefore used to achieve a production of $2+1$ jet events using the first order ME calculations to the greatest possible extent. (In the section describing the final results, the amount of reconstructed $2+1$ jet events originating from the parton showers is presented.) The differences between the data and Monte Carlo in fig. 3.5a should, in any case, not be considered problematical, since what is important for this analysis is that the features of the selected $2+1$ jet events are well described. This is verified by figs. 3.6 and 3.7 in the next section as well as in [21].

How well the jet algorithms reconstruct the underlying hard parton level are shown in figs. 3.5b,c and d. Comparisons of reconstructed jet four vectors and the four vectors of the ME partons are made. With ME partons is meant the two final state partons from the first order QCD matrix element calculations, adjusted for the backward evolution to generate initial state radiation. The final state ME partons describe the hardest emission in the event, and reconstructing their four vectors with jets from calorimeter clusters will be the very best we can ask for. In fig. 3.5b is shown the relative error in the reconstructed energy and in c) the absolute error of the polar angle. The energy in particular is shifted somewhat with respect to zero. This applies to a lesser extent also to the polar angle. A small correction was therefore applied to achieve better estimates of the underlying parton four vectors. This is important since we want to avoid systematic effects when cuts are applied (as explained below) to the four vectors of the reconstructed jets. Fortunately, the reconstruction of the azimuthal angle is however nicely peaked at zero, as can be seen in fig. 3.5d.

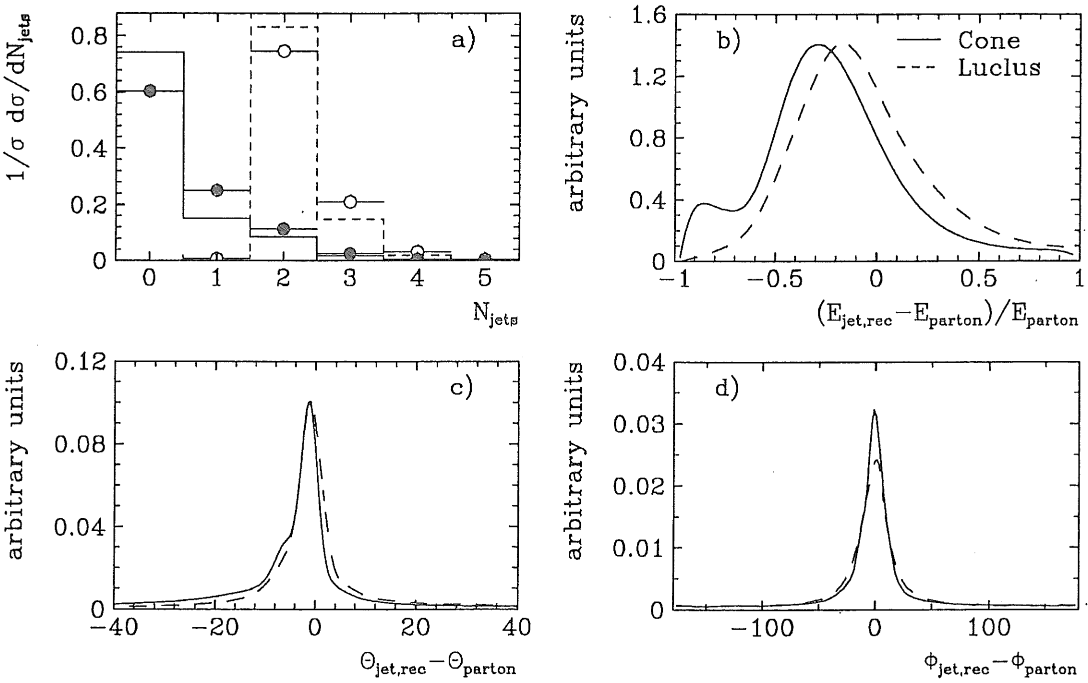

Figure 3.5: *a) Comparing jet multiplicities from* LEPTO *with data, using the* CONE *(full line) and the* LUCLUS *(dashed line) jet algorithm. Error distribution due to the reconstruction of b) the energy c) the polar angles and d) the azimuthal angles of the ME partons.*

3.5 Further requirements

After the DIS neutral current events have been selected and the jet algorithm has provided a subsample of $2+1$ jet events, further requirements are needed to obtain a final sample with well defined and understood features. For instance, only jets with a transverse momentum of at least 4 *GeV* are selected which improves the reconstruction quality of the underlying parton four vectors, and thus also the reconstructed azimuthal angles.

Fig. 3.6a shows the transverse momentum distribution of the jets for both data and LEPTO generated events, using LUCLUS for the jet reconstruction. An excellent agreement is achieved.

The next requirement is that the polar angles of the jets, in the laboratory system, must be within certain limits. Normally, only events with jets within 10° and 150° are allowed. The 10° cut is to exclude events with jets too close to the beam pipe and the very energetic spectator jet, and the 150° cut ensures that only jets measured in the liquid argon calorimeter are used. As we will see in the next section, it is however essential for this study to include jets in the very forward direction and therefore the limits were set to 5° and 150°. As can be seen in fig. 3.6b a satisfactory agreement between the data and the LEPTO generated events is also apparent here.

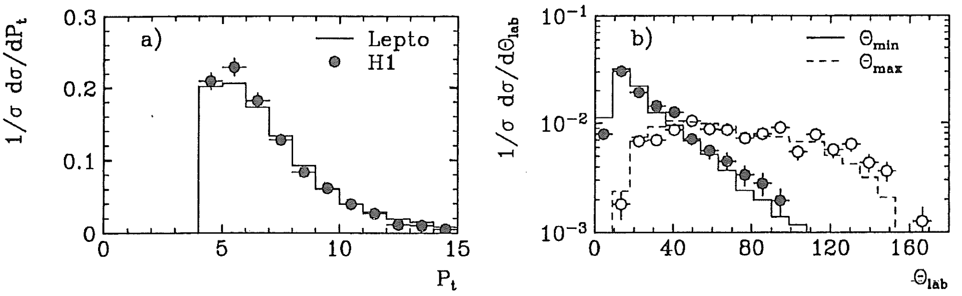

Figure 3.6: *Comparing* LEPTO *with data, using the* LUCLUS *jet algorithm, with respect to a) the transverse momentum distribution of jets and b) the laboratory polar angle distribution of the most forward and backward jet.*

Another variable in which cuts are applied is the azimuthal opening angle of the two hard jets. According to theory, the two final state partons from the first order ME must be exactly back-to-back in the azimuthal plane in the hadronic cms, if intrinsic transverse momentum of the partons in the proton are neglected and no initial state QCD radiation occurs. If intrinsic transverse momentum and especially initial state radiation is included, the opening angle can deviate somewhat from 180°. Already this effect is a problem for the measurement of the azimuthal asymmetries since it is not taken into account in the theoretical predictions. The deviation from 180° can also be a sign of poor reconstruction, either of the jets or of the event kinematics which is reflected in the transformation to the hadronic cms, or both. Therefore only events where the azimuthal opening angle is within 30° from the back-to-back situation are selected. In fig. 3.7a the azimuthal opening angle is shown for reconstructed jets from both LUCLUS and from the CONE algorithm. For both algorithms, a satisfactory agreement between the data and the LEPTO generated events is obtained, but LUCLUS seems to reconstruct jets somewhat more back-to-back. The cut at 180° ± 30° removes the tails of the distributions.

The distribution of the transverse momentum balance ($p_{\perp bal}$) is shown in fig. 3.7b. $p_{\perp bal}$ is the transverse momentum sum of the two hard jets in the hadronic cms and is exactly zero for two jets with equal $p_\perp$ which are back-to-back in the azimuthal plane. It is, in principle,

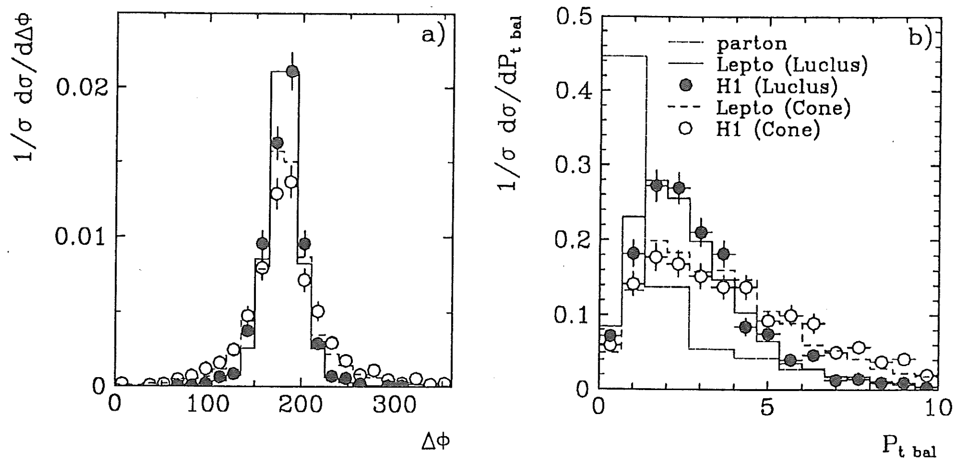

Figure 3.7: *a) The azimuthal opening angle of the two jets and b) the transverse momentum distribution of the sum of the two jets, using* LUCLUS *(full line) and the* CONE *algorithm (dashed line). In b) is also included the distribution of the transverse sum of the two ME partons, adjusted for initial state radiation (dotted line).*

a direct measurement of the amount of initial state QCD radiation, since it corresponds exactly to the transverse momentum of the interacting parton from the proton, and is therefore an interesting measurement. Fig. 3.7b shows the $p_{\perp bal}$ distributions for both the LUCLUS and the CONE algorithms, and again a good agreement with data is obtained. Included is also the parton level result, i.e. what one gets if the two final state partons from the hard ME, (adjusted for initial state radiation) are used to calculate $p_{\perp bal}$. This thus indicates that LUCLUS is less sensitive than the CONE algorithm to final state radiation and detector smearing, and therefore reconstructs the amount of initial state radiation better.

The reason why the azimuthal opening angle is used as a variable in which cuts are applied and not the $p_{\perp bal}$ variable, is that the results of this analysis is not very much affected if the two hard jets do not have exactly the same transverse momentum as long as they are back-to-back. If they are back-to-back the azimuthal angle is probably correctly reconstructed even if they have different transverse momenta, but if the opening angle deviates too much from 180°, it is a sign of either initial state radiation or poor reconstruction.

3.6 Azimuthal acceptance

A necessary condition in the investigation of the azimuthal asymmetries is that the acceptance of events does not depend on the azimuthal angles of the jets, a 'flat' acceptance, or that it is very well known. The cylindrically shaped calorimeter in the barrel gives a complete azimuthal coverage and the only acceptance losses are due to the beam pipe in the forward and backward directions. The acceptance region is easily defined as an $\eta - \phi$

area from $\eta = 3.4$ to $\eta = -3.4$, corresponding to the polar angular cuts of 4° and 176°, and a full acceptance in ϕ from 0° to 360°.

The definition of the ϕ-angles are, however, made in the hadronic cms and one therefore has to investigate the acceptance behavior in this frame. Since the boost to the hadronic cms is defined from the event kinematics which obviously varies from event to event, so will this region of acceptance. The acceptance situation at three different values of y and Q^2 is therefore presented. In these examples is illustrated how the acceptance region, limited by the beam pipe at laboratory polar angles of 4° and 176°, would look like, as well as possible limits at other polar angles ($10°, 30°, 50°, 70°, 90°, 110°, 130°$ and $150°$). In fig. 3.8a the result from $y = 0.4$ and $Q^2 = 12\ GeV^2$, the lower left corner of the kinematic region of selected events (see fig. 3.1), is shown. The laboratory polar angle 10° is marked as filled circles and 150° as filled triangles. As can be seen the azimuthal acceptance is not flat in the hadronic cms. If for instance the limits are set at 10° and 150°, events with jets of rapidities about 4 are only accepted as long as their azimuthal angles are in the region of 180°. The effects on the data sample of the various jet requirements applied, are exemplified in figs. 3.8b,c and d. In b, the distribution of jets, two from each event, is shown when the only requirement is that the jets have a transverse momentum exceeding $4\ GeV$ (it is reflected in the vertical 'cut off' at $\eta = -3.6$). In c an additional requirement that both jets should have laboratory polar angles between 10° and 150° has been added. The problematic non-flat azimuthal acceptance in the backward region is clearly visible. The effect of this on the azimuthal asymmetry measurement is that the ϕ-distributions will be suppressed at angles near 0° (360°), but also at 180° since the two jets of each event are back-to-back in the azimuthal plane. (The corresponding jet to the one that is being lost by the 150° cut at ϕ values near 0° (360°), will be close to 180° but will have a higher rapidity than its partner, and the depletion around $\phi = 180°$ is therefore less visible.) The $\cos 2\phi$ dependence predicted by the theory when both jets of an event is considered, see fig. 1.8, will thus be observed as a more or less flat distribution due to acceptance effects.

One way to circumvent this is to calculate, for each event, the limits in rapidity within which a flat azimuthal acceptance can be achieved. These limits can easily be calculated using the formalism of Lorentz transformations using invariants presented in chapter 1 of this thesis. Let k be a massless laboratory four vector with a certain polar angle θ_{lab}, lying in the plane defined by the transverse boost vector and the z-direction (here the xz-plane for simpler equations):

$$k = (1, \mp \sin\theta_{lab}, 0, \cos\theta_{lab})$$

Its azimuthal angle is either 0° or 180° depending on if the x-component is positive or negative. We can now calculate the rapidity, or more precisely the pseudorapidity (η), of k', vector k transformed to the hadronic cms.

$$\eta = \frac{1}{2}\ln\left(\frac{k_{o'} + k_{z'}}{k_{o'} - k_{z'}}\right)$$

where $k_{0'}$ and $k_{z'}$, the energy and z-component can be calculated, see eqns. (1.4) and (1.5), according to:

$$k_{o'} = \frac{k(P+q)}{E_{p'} + q_{o'}} \quad ; \quad k_{z'} = k_{o'} - \frac{k \cdot P}{E_{p'}}$$

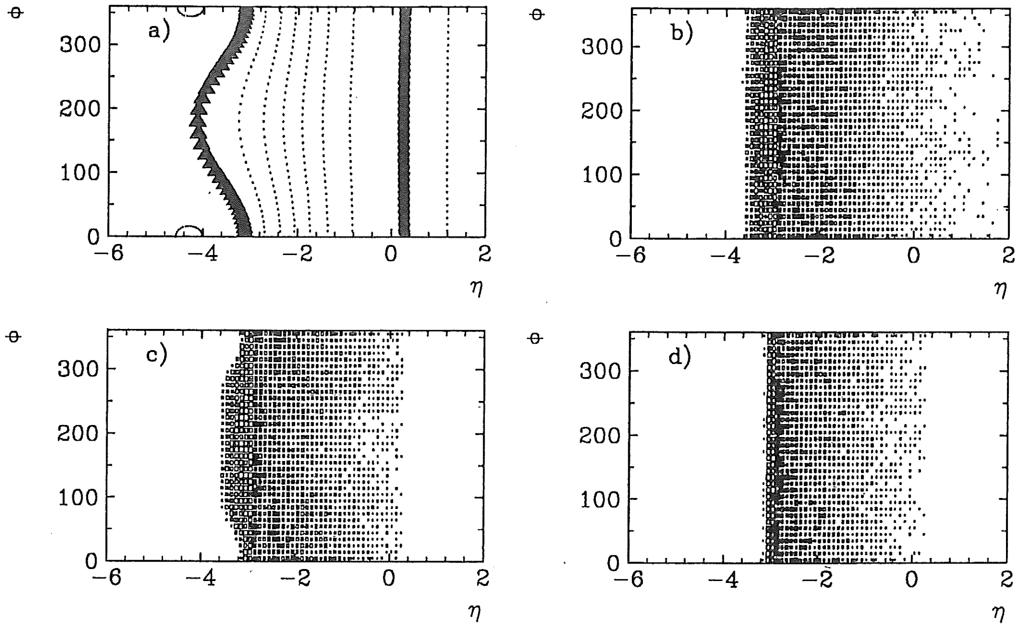

Figure 3.8: *Azimuthal acceptance at* $Q^2 = 12$ *GeV*^{2} *and* $y = 0.4$. *a)* ϕ, η *positions in the hadronic cms of massless four-vectors, in the laboratory system equally spaced in* ϕ *on a cone at a polar angle of* 176°, 150° *(filled triangles)*, 130°, 110°, 90°, 70°, 50°, 30°, 10° *(filled circles) and* 4°. *b) Distribution of jets (two from each event) when the only requirement is that* $p_{\perp,jet} > 4$ *GeV and when also c)* $10^\circ < \theta_{lab,jet1\&jet2} < 150^\circ$ *and finally d) after the azimuthal acceptance cut has been applied.*

The final expression for the rapidity of a laboratory vector k with a polar angle θ_{lab} transformed to the hadronic cms as defined by the specific values of $Bjorken-y$ and $-x$, can then be written

$$\eta \;=\; \frac{1}{2}\ln\frac{yE_e(1+\cos\theta_{lab}) + xE_p(1-y)(1-\cos\theta_{lab}) \mp 2\sqrt{xyE_eE_p(1-y)}\,\sin\theta_{lab}}{E_p(1-x)(1-\cos\theta_{lab})}$$

The $\mp$ sign corresponds to an azimuthal angle of k' (and k) being 0° (plus sign) or 180° (minus sign). Using this expression to calculate the limits for the case illustrated in fig. 3.8, no events with jets outside the rapidity region $-3.1 < \eta < 0.3$ are accepted, as shown in fig. 3.8d.

The second example is given for $y = 0.4$ and $Q^2 = 70$ GeV^2 (see fig. 3.1) with the corresponding results shown in fig. 3.9. This case differs from the first one in that the limit corresponding to a laboratory polar angle of 150° now has broken up in two separate curves. The region without acceptance above 150° in the laboratory system corresponds to a cone centered around the z-axis. In the transformation to the hadronic cms this cone is boosted such that it ends up completely outside the z-axis. The region without acceptance in the hadronic cms is thus the region within the two half circles, and events with jets at very high (negative) rapidities could actually be accepted. Only the region

$-5.5 < \eta < -2.7$ has not a full azimuthal coverage, except of course for the region in the proton direction at $\eta > 0.2$ which is due to the 10° limit. To be able to control this situation, one must try to understand when a cone ends up completely outside the z-axis in the hadronic cms. When the cone is tilted by the transverse boost in such a way that its side exactly coincides with the z-axis in the hadronic cms, the rapidity of a vector $k\prime$, pointing along the side of the cone at an azimuthal angle in lab of 180°, will be $\pm\infty$, depending on if $k_z\prime$ is positive or negative. We can therefore take a k vector, with an azimuthal angle of 180° (k_x negative), and calculate at what value of Bjorken-y (y_{lim}), for a specific value of Bjorken-x and θ_{lab}, we get a rapidity of $-\infty$. This means solving the equation $k_0\prime + k_z\prime = 0$ and we get the following expression:

$$y_{lim} = xE_p \frac{xE_p(1-\cos\theta_{lab})^2 + E_e \sin^2\theta_{lab}}{(xE_p(1-\cos\theta_{lab}) + E_e(1+\cos\theta_{lab}))^2}$$

The other possibility, getting rapidities of $+\infty$ only seems to be possible for Bjorken-x= 1 and is thus not a problem.

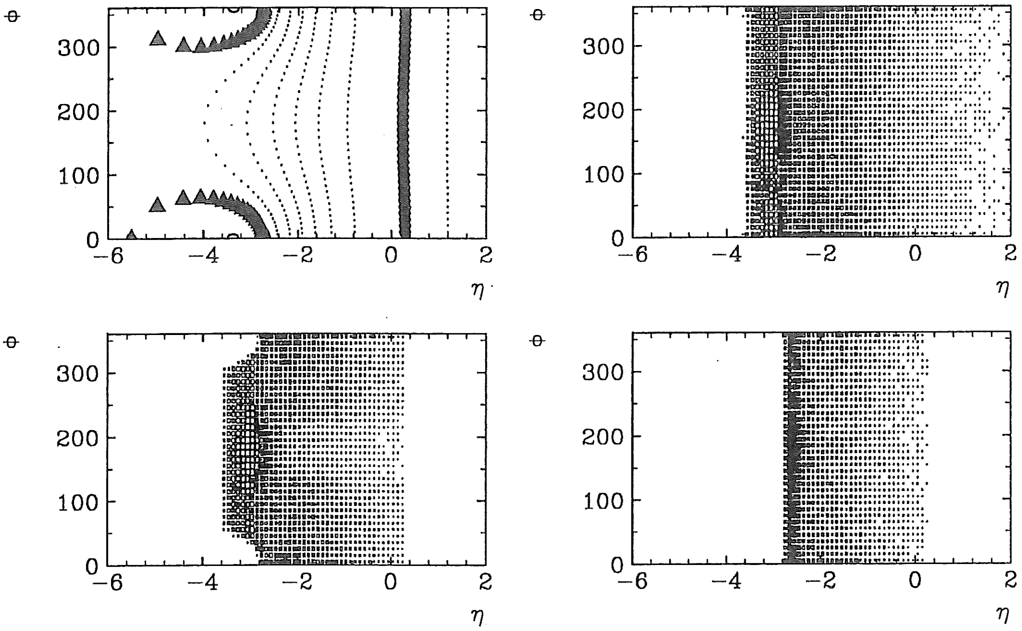

Figure 3.9: *Azimuthal acceptance as in fig. 3.8 but for $Q^2 = 70$ GeV^2 and $y = 0.4$.*

The third example, fig. 3.10, has $y = 0.03$ and $Q^2 = 70$ *GeV*^{2} (see fig. 3.1) and is especially interesting since here the azimuthal asymmetries are at a maximum. The limits of 10° and 150° are heavily distorted. The 150° limit is completely curled up and we have a very small region without acceptance at about $\eta = 2$ and $\phi = 0°$. Also the 10° limit is curved such that events with jets in the forward region will be affected by the non-flat acceptance as well. What should be noted is that the azimuthal acceptance cuts remove most of the events. This prevents a measurement and the only way out of this situation

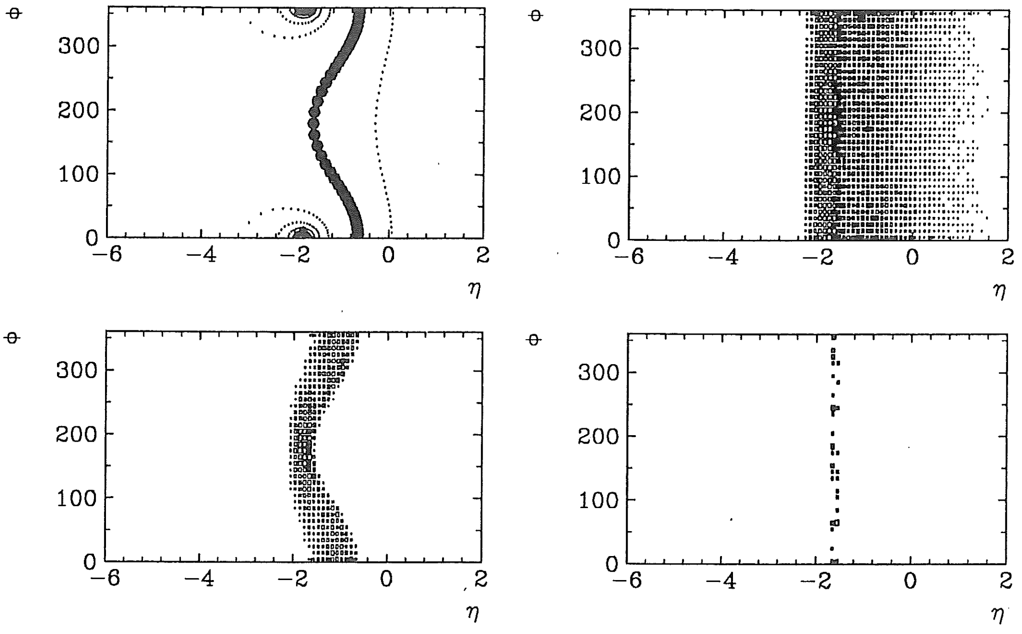

Figure 3.10: *Azimuthal acceptance as in fig. 3.8 but for $Q^2 = 70$ GeV^2 and $y = 0.03$.*

is to accept events with jets of polar angles down to 5°. (Remember that the dotted line to the right of the 10° filled circles line corresponds to polar angles of 4°.)

In addition to the reason of increasing the acceptance of events at high values of x and Q^2, it is also favorable if an acceptance region as large as possible can be used. The reason for this is that the azimuthal acceptance cut described in this section relies on that the laboratory polar angles of the jets can be measured accurately, as well as the variables defining the boost. Systematic effects from poor reconstruction will be hard to handle.

3.7 Jet identification

In the future, with more data available, it will be possible to investigate the azimuthal asymmetries of a quite pure QCD-Compton sample at high values of x and Q^2. In that specific analysis, it would be necessary to identify the jets in the events since the asymmetries of the quark and the gluon would otherwise cancel (see fig. 1.6). One is then only sensitive to the very weak $\cos 2\phi$ dependence, as explained in the first chapter. The problem of jet identification has been thoroughly studied and is presented in appendix C.

For the present investigation, working with a mixed sample of BGF and QCD-Compton processes at low values of x and Q^2, it would in principle be favorable if the two processes were separated using jet identification. The jet energy which provides the most prominent difference between quark and gluon jets in a QCD-Compton processes can however not be used. It turns out that an almost identical energy difference is present between the two quark jets in BGF processes. One is therefore left with the much less distinguishing fragmentational differencies of quarks and gluons, and this is not enough to enable any useful separation of the two processes.

3.8 Results

The possibilities of measuring the azimuthal asymmetries is first presented with results from a Monte Carlo study. The event generator LEPTO was used and events were detector simulated and reconstructed. These results will be called cluster level results and are compared with results on ME partons from the generator directly, called the parton level results. It is thus possible to obtain a sense of how the final state parton shower, the hadronization and the detector smearing affect the measurement. This is also done because of a bug in the LEPTO generator program found at a very late stage in this analysis. The bug concerns the simulated BGF processes only, and in the sense that the most and least energetic jet have been switched with respect to their orientations. If just the parton level results are considered, the error can be corrected for by a simple shift of the azimuthal angle distributions of the partons by 180°. On the cluster level, however, other effects connected to detector smearing and acceptance might very well cause the results to be inconsistent with what could have been obtained from a 'correct' event generator, and of course with real data. I should point out though, that all plots in the theory chapter of this thesis have been corrected for this bug in LEPTO, but since it is a lengthy procedure to re-simulate the detector effects on the MC data and perform the reconstruction, this was not possible within the time limits of my Ph.D studies and this analysis.

In the plots presented here, the azimuthal angles of the two jets in each event are not used directly. Instead a plane, containing the coordinate z axis around which the plane is rotated, is defined such that the minimum amount of transverse momentum out of the plane is achieved. The azimuthal angle of this plane is then used instead. This angle is a somewhat better estimate of the corresponding angle on the parton level, since it to some extent corrects for non perfect boosts and jet reconstruction imperfections. As mentioned in section 3.3, the size of the transverse boost is not so well reconstructed, see fig. 3.4, which can cause the jets in the hadronic cms to deviate from a back-to-back orientation in the azimuthal plane. The same effect is obtained from poorly performing jet reconstruction as mentioned in section 3.5. Using the azimuthal angles defined by the plane with minimum $p_{\perp,out}$ means as well that the azimuthal distributions when both jets in each event is considered, will have a period of 180°. What should also be mentioned is that the bins have been chosen in such a way that they are centered at 0°, 180° and 360° to adapt to the expected azimuthal angle distributions with a $\cos\phi$ and/or a $\cos 2\phi$ dependence. Therefore the first and last bin in the figures are actually the same.

As can be seen from fig. 3.11 where the cluster and parton level results are compared, the measurability seems to be very good. The asymmetry of the mixed sample of QCD-Compton and BGF processes is well reproduced and the influence of QPM processes is negligible. The contribution from QPM processes is due to the fact that a few of these events have been incorrectly reconstructed as 2+1 jet events, fulfilling all the requirements

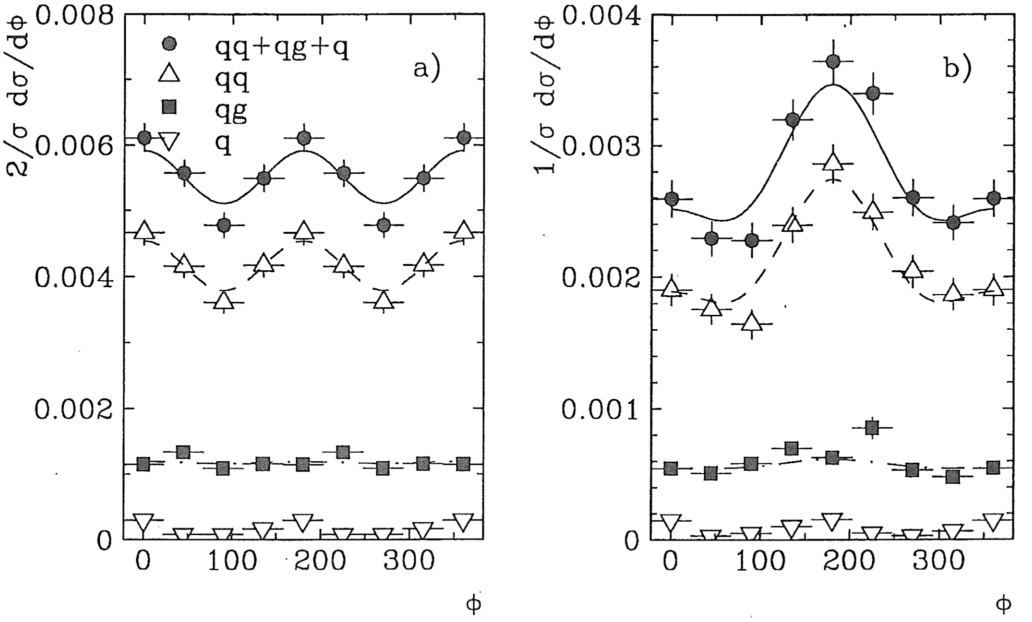

Figure 3.11: *Comparing azimuthal asymmetries as given by* LEPTO *after detector simulation and reconstruction (symbols), with parton level results (lines), for an inclusive sample of BGF (qq), QCD-Compton (qg) and QPM (q) events, and for the different processes individually. a) Including both jets of each event and b) selecting only the most energetic jet. (BGF results wrong by* 180°*.)*

given. The cross section of zeroth order processes is, however, much larger than the cross section of first order processes, and it is therefore not strange that some of them survived the cuts. The asymmetries of the individual processes are also reproduced on the cluster level, which is very promising since it means that the asymmetry we observe is not just due to acceptance or other possible detector effects. The generated azimuthal angular dependence which in the case of BGF processes is a $\cos 2\phi$ distribution, considering both jets, is also observed on the cluster level. In the case of the QCD-Compton process, the generated azimuthal angle dependence is instead more or less flat, as is also what we get on the cluster level, see fig. 3.11a. The distributions for the most energetic jet, fig. 3.11b, are also very well in agreement with the parton level results (although here wrong by 180° for the BGF processes due to the LEPTO bug).

To allow for a comparison with real data, the azimuthal angle of the most and least energetic jet from the LEPTO generated BGF events have been shifted 180°. This shift could only be done after the detector simulation and event reconstruction, and therefore the comparison only tells us if the theoretically predicted asymmetries are in rough agreement with the data. Any detailed comparisons with MC can not reliably be carried out. This is also why just statistical errors are presented in the figures since systematic errors may very well be influenced by the LEPTO bug. As can be seen from fig. 3.12, data appears to behave as predicted by the theory. If both jets are considered, as in fig. 3.12a, the predicted $cos2\phi$ dependence is clearly visible, and if only the most energetic jet is used as in fig. 3.12b, a clear $+cos\phi$ dependence can be seen. Data show somewhat 'steeper' distributions than the MC generated ones, but the possible reason for this can only be speculated on after the 'correct' MC simulation has been performed and the systematic errors have been estimated.

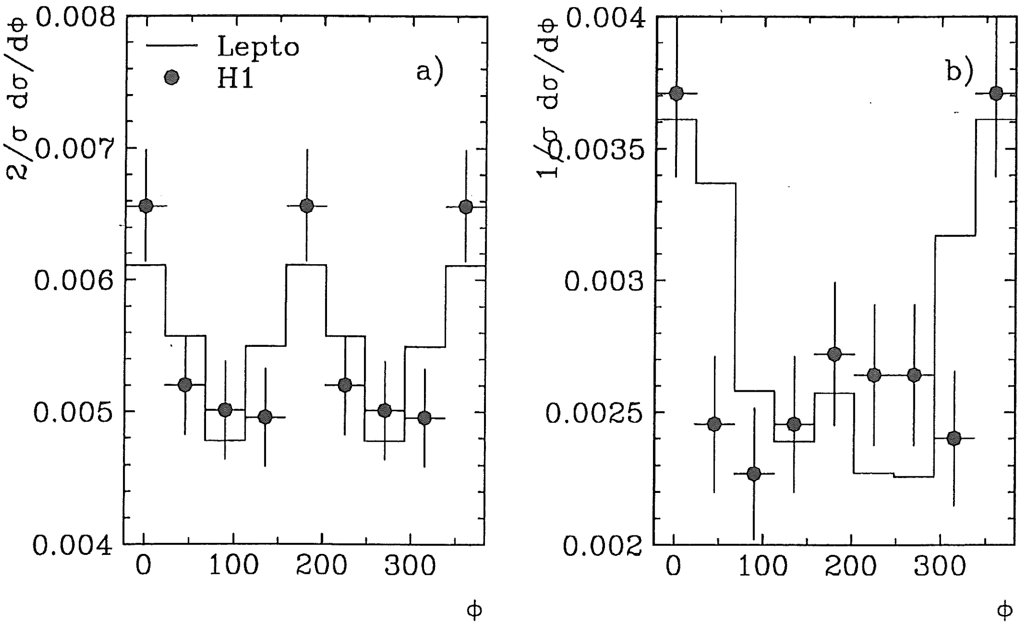

Figure 3.12: *Comparing the azimuthal asymmetry as given by* LEPTO *(where the mentioned bug concerning the mixup of the most/least energetic jet in BGF processes has been 'corrected' by a* 180° *shift) with data. The results should not be taken too seriously but just as an indication of that the data in general do exhibit the theoretically predicted azimuthal distributions. a) Including both jets of each event and b) selecting the most energetic jet.*

3.9 Conclusions

The lepton-hadron azimuthal angle asymmetries of first order QCD processes have been measured for the first time. Various subproblems connected to this analysis have been described, such as the transformation to the hadronic cms, jet reconstruction, the possibilities of jet identification and especially the azimuthal acceptance problems encountered. The importance of a large acceptance in the laboratory polar angular range has been explained.

With the limited amount of data currently available from HERA, and due to a very unfortunate bug in LEPTO (the only presently useful MC event generator for this analysis), no detailed comparisons with simulated events could be made. Only the general features of the asymmetry could be studied, and they seem to agree well with the theoretical predictions.

With more statistics available in the future (10 times more already collected in 1994), and with a 'correct' event generator, detailed studies of the azimuthal asymmetries can be made. As soon as the asymmetries of ordinary QCD events have been investigated thoroughly and are well understood, further conclusions might be drawn from such measurements. As mentioned in chapter 1, the fraction of BGF and QCD-Compton processes can be studied at various values of x and Q^2, and perhaps a definition of the constituents of the Pomeron in diffractive events can be made.

Acknowledgements

There are just too many people involved in a high energy physics experiment of today to thank everybody individually, so a collective 'THANK YOU ALL' must therefore be given to the H1 collaboration at DESY. Another 'THANK YOU ALL' goes to the department in Lund. The time I spent there just got more and more enjoyable. Keep changing! I am also grateful for financial support from the University of Lund, although I could have been even more grateful.

Special thanks goes to my supervisor Leif Jönsson, for support and encouragement, but especially for being open minded to new and sometimes unorthodox methods and ideas.

As a poor experimentalist I often felt a lack of brain power when dealing with theoretical subtleties, and I therefore deeply appreciated the patience and understanding shown to me by two great theoreticians, Gunnar Ingelman and Michael Seymour.

Vincent Hedberg, what can I say?. It is never a dull moment when you are around, not even when you are far away and just electronically connected. Thanks for everything!

Håkan, do I still owe you 50 öre? Thanks for many laughs over the years.

Morten, yes! we have had a million discussions. I'm not sure we solved anything but I hope we will have a million more.

Last, but by far most, I would like to thank the girl with whom I share the morning paper. Tina, since you did put up with me during my ups and downs, when I was the most frustrated by apparently insurmountable and unsolvable issues of physics, I hope you will put up with me for ever more.

Bibliography

[1] H. Georgi, H.D. Politzer, Phys. Rev. Lett. vol.40 nr.1 (1978), p.3

[2] EMC collaboration, Phys. Lett. 130B 1983, p.118

[3] EMC collaboration, Z. Phys. C34 (1987) p.277

[4] A. Mukherjee et.al., Phys. Rev. Lett. vol.60 nr.11 (1988), p.991

[5] E665 collaboration, Phys. Rev. D48, 11 (1993) p.5057

[6] R. N. Cahn, Phys. Lett. 78B 1978, p.269

[7] R. N. Cahn, Phys. Rev. D40, 9 (1989) p.3107

[8] J. Chay, S.D. Ellis, W.J. Stirling, Phys. Rev. D45, 1 (1992) p.46

[9] R.D. Peccei, R. Rückl, Nucl. Phys. B162 (1980) p.125

[10] G. Ingelman, LEPTO version 6.1, in [23] vol. 3, p.1366

[11] M.H. Seymour, *A Simple Prescription for First Order Corrections to Quark Scattering and Annihilation Processes*, Lund preprint LU TP 94-13, submitted to Nucl. Phys. B.

[12] B. H. Wiik, in [23] vol. 1, p.1

[13] I. Abt, et al., H1 Collaboration, DESY 93-103

[14] T. Kurca, *The H1 Trigger for Neutral Current Deep Inelastic Scattering Events at Low Q^2*, Ph.D. thesis, Hamburg University, (H1-06/94-364)

[15] I. Abt et al., H1 collaboration, Nucl. Phys. B407 (1993) p.515

[16] M. Derrick et.al., Zeus collaboration, Z. Phys. C59 (1993) p.231

[17] F. Jacquet, A. Blondel, Proceedings of the study of an ep facility for Europe 79/48 (1979), p.391, U. Amaldi ed.

[18] S. Bentvelsen, J. Engelen, P. Kooijman, in [23] vol. 1, p. 23

[19] F. Abe et al., Phys. Rev. D45 (1992) p.1448
M. Seymour, LU TP 93-7, May 1993.

[20] T. Sjöstrand, Computer Phys. Comm. 28 (1983) p.227

[21] L. Jönsson, H. Küster, M. Nyberg-Werther, J. Stier, *A Measurement of the Gluon Density in the Proton at Low x*, included in Ph.D. thesis, M. Nyberg-Werther, Lund University (ISBN 91-628-1451-6) LUNFD6/(NFFL-7090)1994

[22] D. Graudenz, N. Magnussen in [23] vol. 1, p.261

[23] Proceedings 'Physics at HERA', Eds. W. Buchmüller, G. Ingelman, DESY Hamburg 1992, vol. 1-3

Appendix A

Asymmetries in Jet Azimuthal Angle Distributions as a Test of QCD

LUNFD 6/(NFFL-7069) 1992

Asymmetries in Jet Azimuthal Angle Distributions as a Test of QCD*

V. Hedberg[a], G. Ingelman[b], C. Jacobsson[a], L. Jönsson[a]

[a] Dept. of Elementary Particle Physics, Lund University, Lund, Sweden
[b] DESY, Hamburg and Dept. of Radiation Sciences, Uppsala University, Sweden

Abstract: First order QCD matrix elements predict a specific dependence in azimuthal angle (around the DIS current direction) of the produced jets which, at HERA energies, gives a new test of QCD. We show how the QCD Compton process can be used for this purpose, taking experimental effects into account. In the analysis we introduce a novelty in the jet finding procedure and we separate quark and gluon jets by using a neural network.

1 Introduction

The description of the hadronic final state in deep inelastic scattering (DIS) is influenced by perturbative QCD in several ways, as can be calculated through exact matrix elements or leading log parton showers [1]. In this study we will consider the distribution of jets in azimuthal angle Φ around the exchanged boson direction since this has been proposed as a suitable test for first order QCD matrix elements [2]. However, at low energies the expected effect is masked by the influence of the primordial transverse momentum [3, 4] and the hadronization, which are described by non-perturbative QCD. Thus, the effect from the underlying perturbative parton process has not been possible to observe in lepton scattering experiments on fixed targets [5]. With increasing energy, the perturbative effect is expected to dominate over the non-perturbative ones and the situation should therefore be more favourable at HERA energies [6]. In the following we will investigate the prospects for such a QCD test at HERA. To be realistic, we have performed a full event simulation and have taken experimental effects into account by using a detector simulation program.

2 The QCD Φ-dependence

The hadronic final state is best studied in its own center-of-mass system (cms), i.e. the cms of the exchanged boson and the proton. A z-axis along the proton direction can then be chosen to define longitudinal and transverse momentum components. The angle we consider is the azimuthal angle around this axis and with $\Phi = 0$ defined by the scattered lepton, which together with the incoming one forms the lepton scattering plane shown in Fig. 1. In the naive quark-parton model (QPM) the incoming quark will be back-scattered along this z-axis. However, in first order QCD processes such as QCD Compton

---

*Submitted to the Proceedings of the HERA Workshop 1992

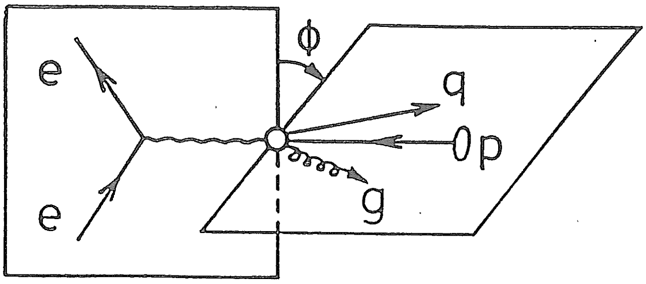

Figure 1: *The first order QCD Compton process, $\gamma^* q \to qg$, viewed in the hadronic (i.e. boson-proton) center-of-mass system. The lepton scattering plane and the parton plane are shown as well as the azimuthal angle around the boson direction with $\Phi = 0$ defined by the scattered lepton.*

($\gamma^* q \to qg$) and boson-gluon fusion (BGF) ($\gamma^* g \to q\bar{q}$) two final partons will emerge with some transverse momenta. These transverse momenta will balance (neglecting primordial $k_\perp$ to be discussed below) and therefore define the 'parton plane' as illustrated in Fig. 1. The azimuthal angle between this plane and the lepton scattering plane has a non-trivial distribution given by the QCD matrix elements [2, 6] that can be schematically written

$$\frac{d\sigma}{dcos\Phi} = A + B\, cos\Phi + C\, cos2\Phi \tag{1}$$

where A, B and C are given by QCD. The complete first order cross-section is five-fold differential and depends, in addition to Φ, on the normal DIS kinematic variables x and Q^2 as well as on two extra variables needed to specify energy and polar angle of one parton (the other parton follows by energy-momentum conservation). Thus, A, B and C will in general depend on these variables (except Φ) or the integral over some of them if a more inclusive cross-section is considered. In particular, B and C tend to increase with $p_\perp$ of the partons.

In the case of the incoming quark having a non-zero primordial transverse momentum $k_\perp$, reflecting the Fermi motion in the proton, it will be back-scattered keeping its transverse momentum such that an azimuthal angle can also be defined in the zero-order QPM process. The resulting Φ-distribution is not flat, but leads to an asymmetry that is different from the one in the first order QCD process [3, 4]. In addition, the fluctuations in hadronization, which are essentially symmetric around the quark momentum direction, will tend to reduce the Φ-asymmetries at the hadron level. Both these non-perturbative transverse momentum effects should be limited to a few hundred MeV and, therefore, play less of a role in events with large $p_\perp$ which are dominated by the QCD process. At the relatively low cms energies in fixed target scattering experiments, however, the cross-section at sufficiently high $p_\perp$ is too small and the previous analyses [5] have been dominated by the Φ-dependence due to the non-perturbative effects and, in fact, have been used to estimate $k_\perp$.

The following study is based on the simulation of complete events using the AROMA [7] and LEPTO [8] Monte Carlo programs, based on the exact, fully differential first order

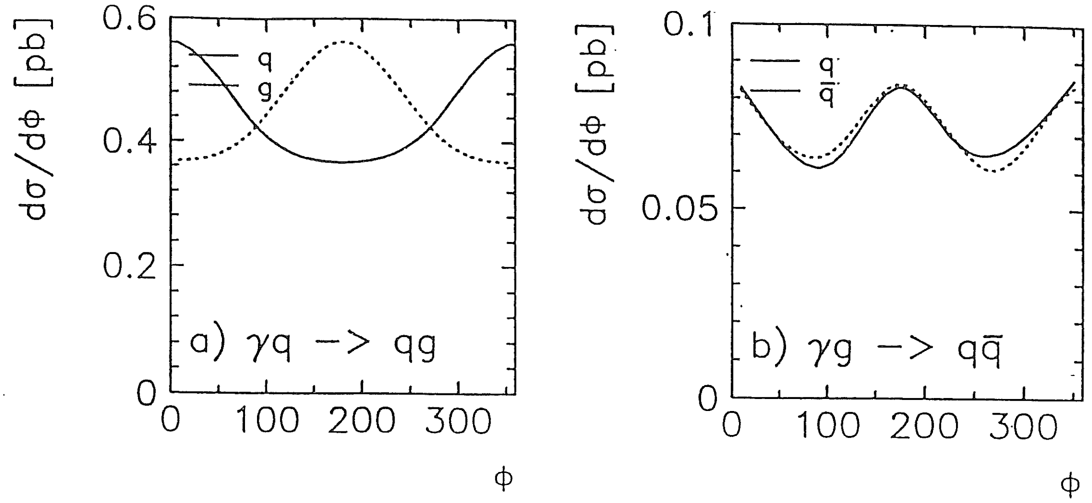

Figure 2: *Differential cross-section versus azimuthal angle for partons, with $p_\perp \geq 4$ GeV, produced by (a) the QCD Compton and (b) the boson-gluon fusion processes, (in the selected kinematic region shown in Fig. 4).*

QCD matrix elements. Primordial transverse momentum is included using the conventional Gaussian distribution (with a width of 440 MeV) and hadronization is performed using the Lund model [9, 10].

The Φ-dependence of partons with $p_\perp \geq 4$ GeV is shown in Fig. 2 for both the QCD Compton and the boson-gluon fusion processes. These distributions are different and tend to give a reduced effect if added. Therefore it is preferable to separate the two processes to make the interpretation clearer. In this sense one process is the background to the other. In the QCD Compton case, the quark and the gluon have opposite distributions that would cancel the effect if added. The proper way to resolve this is, of course, to separate the two by identification of quark and gluon jets. It may also be possible to add them with their energies as weights relying on the fact that the quark jet usually is more energetic in this frame. In the fusion process there is symmetry between the quark and the antiquark such that their distributions can simply be added. As an overall measure of these Φ-asymmetries one can use

$$\langle cos\Phi \rangle = \frac{B}{2A}\,, \quad \langle cos2\Phi \rangle = \frac{C}{2A} \tag{2}$$

which thus directly measure the QCD coefficients, since A can be obtained from the jet rate integrated over Φ. The parton level distributions of these quantities are shown in Fig. 3, which demonstrate the increasing asymmetry with increasing parton $p_\perp$. In the Compton case, the asymmetry increases strongly up to about 4 GeV after which it tends to level off. In the subsequent analysis we require the jet to have $p_{\perp jet} \geq 4$ GeV to obtain a significant asymmetry and to ensure a suitable region for perturbative QCD. From Fig. 2 and 3 it is clear that the Compton process will have a significant contribution from the $cos\Phi$ term but only a small one from the $cos2\Phi$ term, whereas the situation is quite the opposite for the fusion process.

The size of the effect also depends on the event kinematics and, in particular, the asymmetry is larger for larger x. In the following analysis, we have concentrated on the QCD Compton process and return in the concluding discussion to the BGF process. The

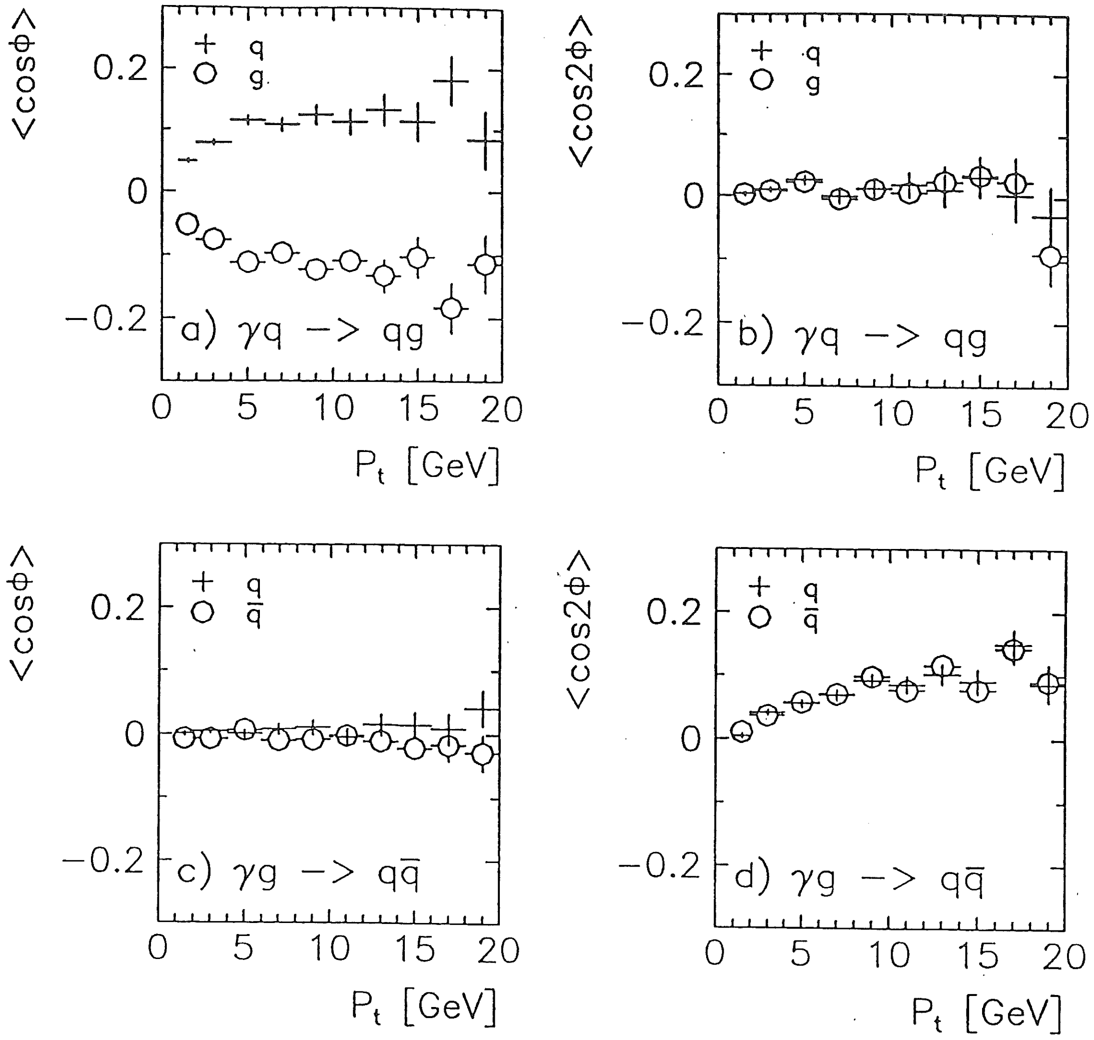

Figure 3: *Azimuthal asymmetries of the partons produced in (a,b) the QCD Compton process and (c,d) the boson-gluon fusion process versus the parton transverse momentum. The kinematic region of Fig. 4 is selected and the error bars correspond to an integrated luminosity of 100* pb^{-1} *illustrating an ideal (parton level) measurement.*

choice of the kinematic region shown in Fig. 4 is based on several criteria that must be fulfilled. The lower limit in y is motivated by the measurement of the scattered electron, which is needed to define $\Phi = 0$ as well as to reconstruct x and Q^2 for the transformation to the hadronic cms. The relatively large x-values enhance both the size of the azimuthal asymmetry and improves the ratio of the signal (QCD Compton) to the BGF 'background' which has a softer x-distribution governed by the gluon distribution. The ratio of cross-sections in this region is, for $p_\perp \geq 4$ GeV,

$$\frac{\sigma(\gamma q \to qg)}{\sigma(\gamma g \to q\bar{q})} = \frac{160\,pb}{46\,pb} = 3.5 \qquad (3)$$

giving a favourable signal-to-background ratio, which may be further improved by either applying some event topology cuts or exploiting the quark/gluon jet separation discussed below. This dominant background, as well as others, are therefore neglected in the following. To perform this QCD test one must thus measure the scattered electron, reconstruct

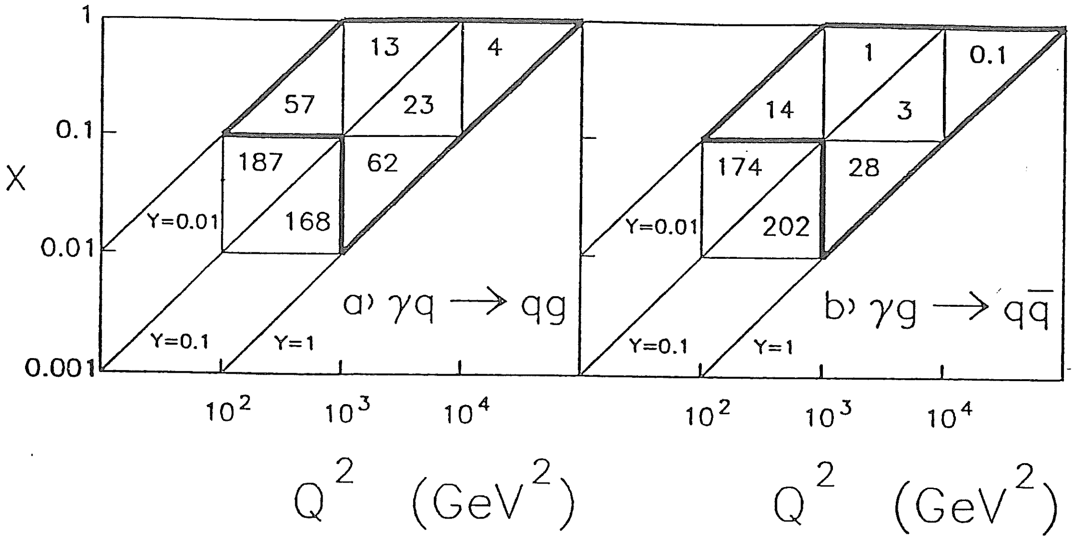

Figure 4: *The kinematic region marked by the thick black line was selected in this analysi Cross-sections in pb are given for (a) the QCD Compton signal process and (b) the fusion 'background' process. The parton level cross-section for* $p_\perp \geq 4$ *GeV are shown.*

the event kinematics and select the above x, Q^2-region. Jets have to be found and identified as quark or gluon jets and their azimuthal distributions in the hadronic cms have to be measured and compared with the QCD expectations.

3 Experimental aspects

In order to investigate the influence of the H1-detector on the generated events, we applied the detector simulation program H1PSI [11] and for the analysis of the resulting detector output we used the tools provided by the physics analysis package H1PHAN [12]. Energy clusters in the calorimeters were formed by the program PACLUS [11], which was tuned to give somewhat fewer clusters than real particles.

3.1 Electron tagging and reconstruction of event kinematics

All particles that gave rise to a track, which was uniquely connected to a cluster with more than 90% of its energy in the electromagnetic part of the calorimeter, were classified as electrons and were hence candidates for being the scattered electron. In our kinematic region, the scattered electron has always an angle greater than 20° (relative to the incoming electron) and an energy larger than 10 GeV. Requiring our candidates to fulfill these criteria in addition, gave a reliable identification of the scattered electron such that in 90% of the events an electron fulfilling these requirements was found and the probability of missidentification was very low.

As mentioned, the kinematics of the event has to be determined to allow for a transformation into the hadronic center of mass system. We have compared the results from a reconstruction of the kinematic variables, when only the information from the scattered electron was used, with the 'double angle' method [13], where information also from the hadronic system was included (in our case based on the calorimeter only). The double angle method is slightly better in our kinematic region and can be expected to deteriorate less when initial QED radiation is taken into account.

3.2 Jet reconstruction

For the jet reconstruction, we have only used the calorimeter information and not yet exploited the expected improvement, on the jet four-vector reconstruction, when including information from the tracking devices. Jets were found using the JADE algorithm in LUCLUS [10], where the pair of particles (or clusters) with the smallest invariant mass are joined into a cluster. The procedure is then repeated until all remaining pairs have an invariant mass exceeding a cut-off, i.e. $m_{ij}^2 > y_{cut}M^2$ where M is a suitable reference-mass such as the invariant mass W of the hadronic system. The final clusters then represent the jets in the event. Although most of the spectator-jet will escape down the beampipe, some of its fringe particles might still hit the detector. Since all particles are assigned to a jet, this may cause either extra jets or biases of other jets and it is therefore important to also reconstruct the spectator-jet properly. For this purpose, we introduced a 'pseudo-particle' with a momentum equal to the measured missing longitudinal momentum. This will ensure that the observed particles from the hadronization of the proton remnant will, to a large extent, be correctly associated with the spectator-jet.

We have found that using the hadronic mass W as a reference in the jet algorithm is not appropriate for our purposes (and most likely also not in other cases). In our kinematic region, W^2 can vary by several orders of magnitude ($W^2 = Q^2(1-x)/x + m_p^2$), whereas the squared invariant mass $\hat{s}$ of the quark-gluon system is rather constant around 200 GeV^2. The cut in the invariant mass squared, $m_{ij}^2 = y_{cut}W^2$, of a jet, will thus not scale according to the hard scattering process, as desired, but the quark and gluon jets will be treated differently in different kinematic regions.

To overcome this problem, we introduced a new feature in the jet reconstruction procedure by dividing it into two steps. First the jet algorithm was applied to the complete event, including the pseudo-particle, using W as the reference mass. This gave a good reconstruction of the spectator-jet since the mass-cut varies properly with its angular separation from the remaining hadronic system. This latter system, with mass W_{rem}, is then associated with the hard scattering system, i.e. the quark-gluon system with mass squared $\hat{s}$. The y_{cut}-parameter was tuned to give the optimal agreement between W_{rem}^2 and $\hat{s}$ and we show the result in Fig. 5a obtained for $y_{cut} = 0.06$. (The small bump at large positive values is due to cases where the gluon jet is not separated from the spectator-jet. Since this affects the reconstructed spectator-jet, it can be removed by a cut on the angle of the spectator-jet.) In the second step, the particles belonging to the spectator-jet was removed and the jet algorithm applied to the remaining system, but with W_{rem} as the proper reference scale for the hard scattering system. For our purposes we now tuned the y_{cut}-parameter to give the maximum number of two-jet events, however, still keeping it large enough to avoid creating artificial extra jets which could make normal one-jet DIS events look like QCD Compton events. Choosing $y_{cut} = 0.18$, we obtained the jet multiplicity shown in Fig. 5b for our kinematic region.

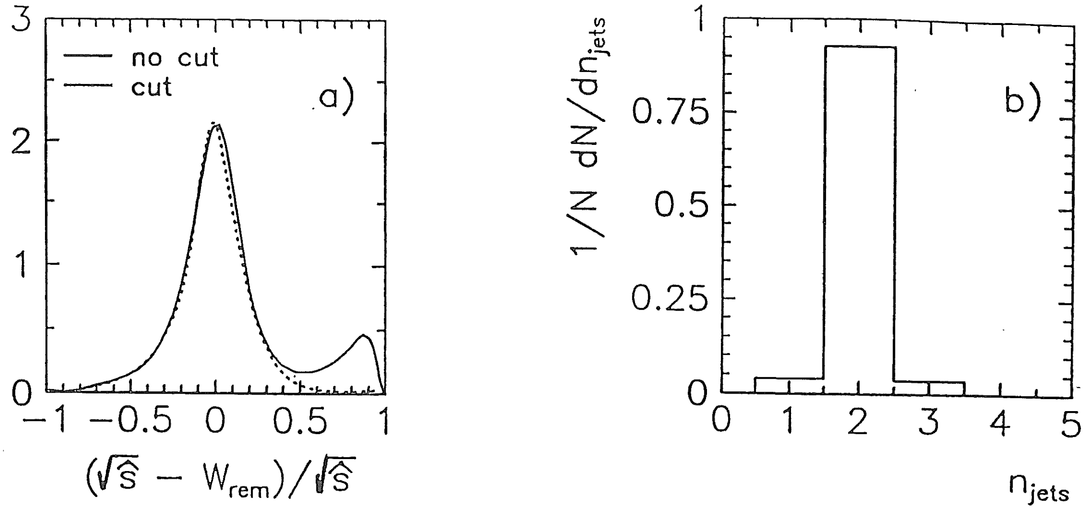

Figure 5: *(a) The relative error in the reconstructed invariant mass* $\sqrt{\hat{s}}$ *of the hard scattering quark-gluon system (with and without cut in the angle of the spectator-jet). (b) The jet multiplicity distribution for QCD Compton events after removing the spectator-jet and repeating the jet finding algorithm.*

3.3 Transformation to the hadronic cms

To make the transformation into the hadronic cms, where the azimuthal angle has been defined, we calculated the four-vector PH_i of the hadronic system in the following way:

$$\begin{aligned} PH_x &= -\cos\Phi_\ell E_\ell\sqrt{1-\cos^2\theta_\ell} \\ PH_y &= -\sin\Phi_\ell E_\ell\sqrt{1-\cos^2\theta_\ell} \\ PH_z &= E_p - E_e - E_\ell\cos\theta_\ell \\ PH_E &= E_p + E_e - E_\ell \end{aligned} \tag{4}$$

where x, y and Q^2 are obtained from the double angle method giving $E_\ell = E_e(1-y) + \frac{Q^2}{4E_e}$ whereas Φ_ℓ and θ_ℓ are determined directly from the measured electron. In particular the reconstruction of PH_x and PH_y was improved using the double angle method compared to when only the information from the scattered electron was used. PH_x and PH_y

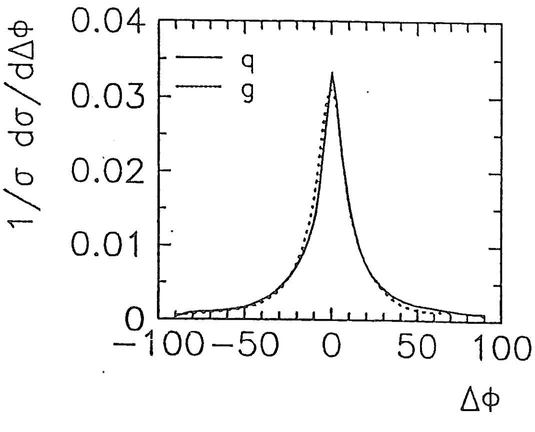

Figure 6: *The distribution of the error on the azimuthal angle (in degrees) of the reconstructed jets, taking detector simulation effects into account.*

are used in the transverse boost and, as can be understood from Fig. 1, the resulting azimuthal angle is affected by the transverse boost but not by the longitudinal one. After the transformation has been completed, rotations are performed to obtain the initial proton momentum along the z-direction and the transverse momentum components of the electrons along the x-direction. The resulting absolute error on the reconstructed azimuthal angles of the jets is shown in Fig. 6.

3.4 Jet identification using a neural network

As explained in section 2, the quark and gluon jet should preferably be identified to get an optimal result. Such an identification has to be based on characteristic differencies in the production and hadronization of these partons. This is a typical feature recognition problem well suited for a neural network.

A neural network [14] has a hierarchic structure of several layers of nodes (neurons) where each node is connected via synapses to every other node in the adjacent layers. The number of nodes should be correlated to the number of input parameters presented to the network. The latter number depends in turn on how many variables that are sensitive to differencies in the objects to be separated. The input data are given to the lowest layer of the network and are then fed through the synapses, where the input values are weighted, to the nodes in the next layer. A transfer function in each node converts the sum of all input values from the incoming synapses, to an output value that is passed on further up in the network. In the hidden layers, i.e. layers between the input and output layer, an internal representation of the observed data is constructed and in the top layer the data is put into different categories. The network has to go through a learning procedure in which a data sample (most often Monte Carlo generated) with known properties is used as input. The weighting at the synapses will then be adjusted to minimize the error in categorizing the data. The data sample is presented to the network repeatedly until this error is acceptably small.

We have used the program package JETNET 2.0 [15] to construct our network, a Multilayer Perceptron, and we have applied a 'backpropagation' learning procedure. The architecture of the network consisted of 10 input nodes, 15 hidden nodes and 1 output node. As input to the network we have selected the following quantities that show differences between quark and gluon jets (cf. Fig. 7ab):

- the energy of the jet, E_{jet}, and
- the nine most distinguishing Fodor moments: $F_{00}, F_{01}, F_{02}, F_{10}, F_{11}, F_{12}, F_{13}, F_{21}, F_{310}$.

The Fodor moments [16] are defined as $F_{mn}(E_{jet}) = \sum_i \left(\frac{p_{ti}}{E_{jet}}\right)^m \eta_i^n$ where the sum is over all particles in a jet. The transverse momentum p_t and the pseudorapidity η are calculated with respect to the jet axis. All ten input variables were scaled to give values in the region between zero and one since this simplifies the learning procedure of the network. A transfer function of the form $g(x) = 1/(1 + exp(-2x))$ was used in all nodes and the summed squared error in the network output provided a quality measure of the performance of the network. A training sample of 3000 quark jets and 3000 gluon jets was generated with our complete Monte Carlo chain. The learning rate, which defines the size of the corrections of the weights each time they are adjusted, had an initial value of

0.05 and was set to decay during the learning phase to allow the net to settle in a stable state. When the complete training sample had been presented to the network 200 times the performance of the network was evaluated by a new test sample containing 2000 quark and gluon jets which were correctly identified in 73% of the cases, see Fig. 7c. Correctly identified means that the network gave an output value above 0.5 for a quark jet and a value below 0.5 for a gluon jet.

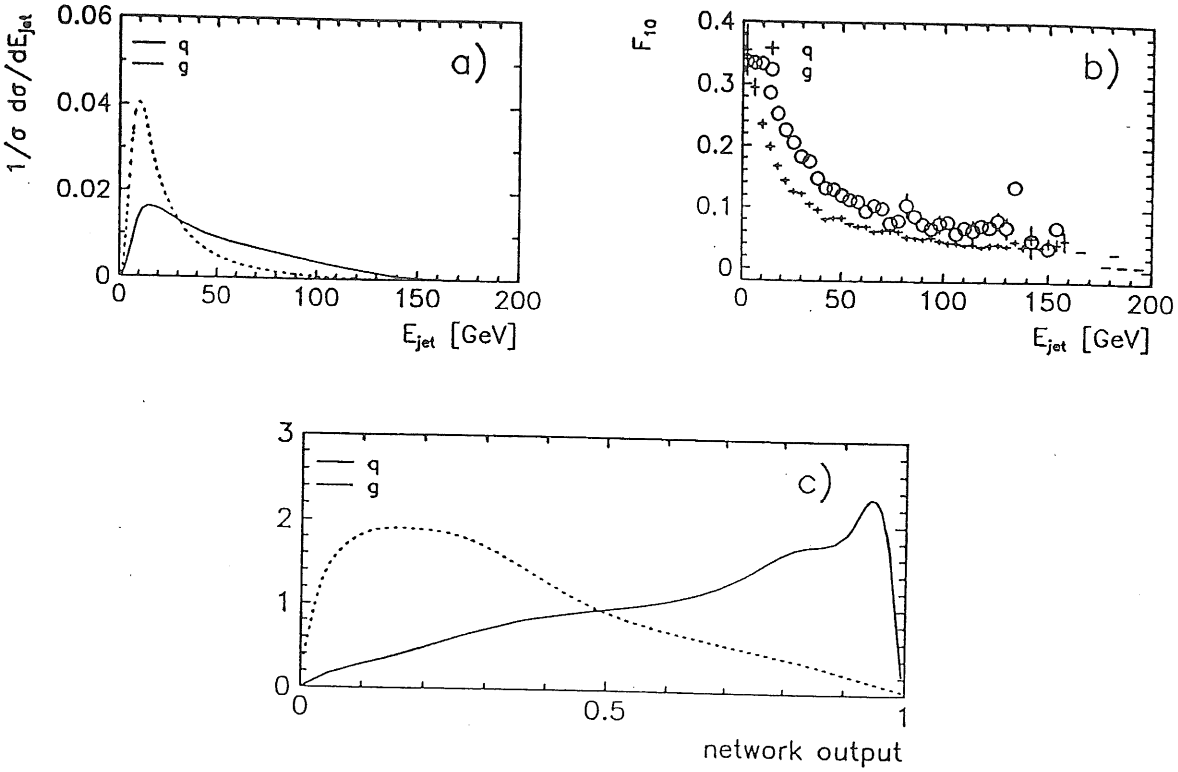

Figure 7: *(a) The energy of quark and gluon jets and (b) an example of a Fodor moment used as input to the neural network. (c) The network output classification of quark and gluon jets.*

Taking advantage of the fact that QCD Compton events must contain exactly one jet of each kind, we required one output value larger than 0.5 and one value smaller than 0.5 for each event. This requirement was fulfilled in 67% of the events for which 86% of the jets were correctly assigned. (In principle, the effect of the remaining missidentification on the final asymmetry results can be corrected for.) It should be pointed out however, that the condition for a succesfull use of the neural network method, based on supervised learning, is that the training sample presented to it has been generated according to a Monte Carlo model which gives a reasonable description of reality. The sensitivity of the network to different models is one way of testing the reliability of the network result. This has not been checked in our particular case, but previous studies of quark and gluon jet separation have indicated that the model dependence is fairly weak [17].

4 Results and conclusions

The final distributions in azimuthal angle for our quark and gluon jets (with $p_\perp \geq 4$ GeV) are given in Fig. 8. After detector simulation a clear asymmetry can still be observed. Close to $\Phi = 0$ there are some discrepancies between the asymmetries after reconstruction and the asymmetries at the generated parton level. These discrepancies may occur if the cuts applied introduce a bias in Φ or if the quality of the reconstruction and identification of jets is correlated with their Φ-angle. Such effects can arise due to the transverse boost between the hadronic cms and the lab system, since a jet with $\vec{p}_\perp$ opposite (parallel) to this boost may loose (gain) $p_\perp$ and therefore be more difficult (easy) to reconstruct properly in the lab system. In particular, small $p_\perp$ jets in the lab system are more likely to be (partly) lost in the beam pipe.

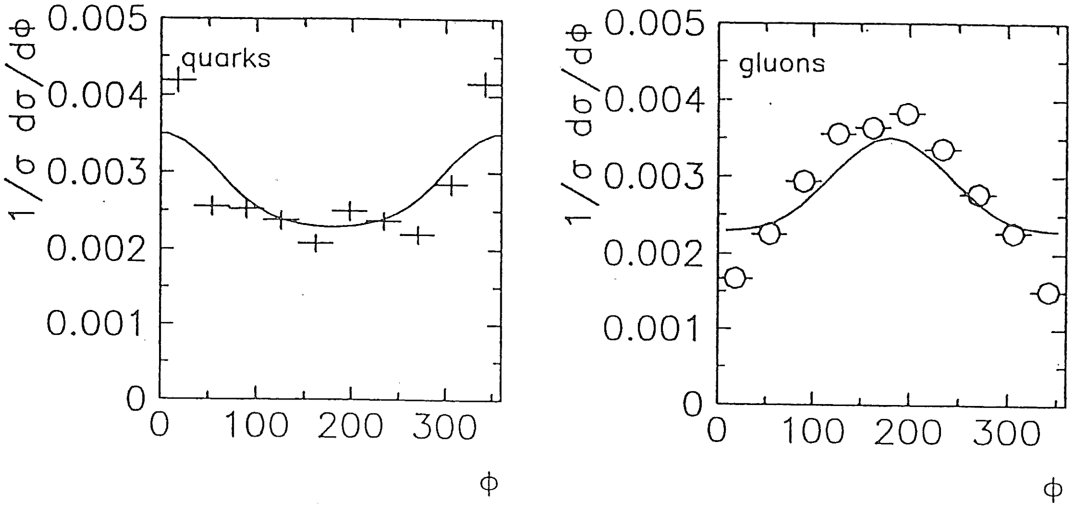

Figure 8: *The reconstructed azimuthal angle distribution for quark and gluon jets (data points) compared to the original parton level distribution (curves). The jets have passed through detector simulation and the sample corresponds to an integrated luminosity of 100* pb^{-1}.

Fig. 8 is based on a QCD Compton sample with no background. We have found that the fusion process, which should yield the dominating background to our two-jet sample, is about a factor four lower in cross-section and should therefore not influence the results to a large extent. This background will, however, be further reduced by the jet identification which should rarely classify $\gamma g \to q\bar{q}$ events as having a quark and a gluon jet.

Finally, we would like to mention that the asymmetry in the fusion process can be measured as well. An identification of the quark and antiquark jet is not neccessary, since their distributions in azimuthal angle are identical due to the crossing symmetry of the matrix element, and they can therefore be added together. The background, which in this case is the QCD Compton process, would then give a flat contribution (when quark and gluon jets are added without jet identification) and hence it would not disturb the wanted asymmetry.

References

[1] M. Bengtsson, G. Ingelman, T. Sjöstrand, in Proc. HERA workshop, Hamburg 1987, DESY Hamburg 1988, vol 1, p. 149
M. Bengtsson, G. Ingelman, B. Naroska, *ibid* vol 1, p.281

[2] H. Georgi, H.D. Politzer, Phys. Rev. Lett. 40 (1978) 3
G. Köpp, R. Maciejko, P.M. Zerwas, Nucl. Phys. B144 (1978) 123
A. Mendez, A. Raychaudhuri, V.J. Stenger, Nucl.Phys. B148 (1979) 499

[3] R.N. Cahn, Phys. Lett. 78B (1978) 269

[4] A. König, P. Kroll, Z. Physik C16 (1982) 89

[5] M. Arneodo et al., EMC collaboration, Z. Phys. C34 (1987) 277
A. Mukherjee et al., Phys. Rev. Lett. 60 (1988) 991

[6] J. Chay, S.D. Ellis, W.J. Stirling, Phys. Rev. D45 (1992) 46

[7] G. Ingelman, G.A. Schuler, AROMA 1.2, unpublished program manual
G. Ingelman, G.A. Schuler, Zeitschrift für Physik C40 (1988) 299

[8] G. Ingelman, LEPTO version 5.2, unpublished program manual

[9] B. Andersson, G. Gustafson, G. Ingelman, T. Sjöstrand, Phys. Rep. 97 (1983) 31

[10] T. Sjöstrand, JETSET 6.3, Comp.Phys.Comm. 39 (1986) 347, *ibid* 43 (1987) 367

[11] R. Nisius, P. Schleper et. al., 'A Guide to H1PSI', H1 internal note

[12] H. Albrecht, M. Erdmann, P Schleper, 'PHAN, a physics analysis program for H1'

[13] P. Kooijman, HERA workshop 1991, these proceedings

[14] C. Peterson, T. Rögnvaldsson, Lund preprint LUTP 91-23 to appear in proc. CERN school of computing 1991

[15] L. Lönnblad, C. Peterson and T. Rögnvaldsson, Lund prepint LUTP 91-18, to appear in Comp. Phys. Comm.

[16] Z. Fodor, Phys. Rev. D41, 1726 (1990)

[17] L. Lönnblad, C. Peterson and T. Rögnvaldsson, Nucl. Phys. B349 (1991) 675

Appendix B

Study of Jet Reconstruction Algorithms for Deep-Inelastic Events at HERA

Z. Phys. C 63, 49–62 (1994)

ZEITSCHRIFT
FÜR PHYSIK C

Study of jet reconstruction algorithms for deep-inelastic events at HERA

V. Hedberg[1], G. Ingelman[2,3], C. Jacobsson[1], L. Jönsson[1]

[1] Department of Physics, Lund University, Sölvegatan 14, S-223 62 Lund, Sweden
[2] Deutsches Elektronen-Synchrotron DESY, Notkestrasse 85, D-22603 Hamburg, Germany
[3] Department of Radiation Sciences, Uppsala University, Box 535, S-751 21 Uppsala, Sweden

Received: 19 January 1994

Abstract. Three commonly used jet algorithms and two new ones have been studied with respect to their performance in the new experimental situation of deep-inelastic scattering at the HERA electron-proton collider. Their ability to reconstruct properties of the underlying parton level subprocesses was investigated. This relates to first order QCD matrix elements and higher order parton emissions as described by parton showers. A new method was devised to determine suitable values for the resolution parameters of the algorithms and assess their reconstruction quality. The Jade algorithm, which is frequently used in e^+e^--annihilation, is found to perform less well compared to other algorithms.

1 Introduction

High-energy quarks and gluons emerging from hard scattering processes are not directly observable due to the confinement of colour charges in quantum chromodynamics (QCD). Instead they are revealed through the appearence of so-called jets, i.e. collimated flows of hadrons, which can be reconstructed from the observed particles. Although this hadronisation process from partons (i.e. quarks and gluons) to hadrons is not understood from first principles, it is well described by phenomenological models. Due to the complexity of the process these models require elaborate Monte Carlo simulation programs for the calculation of detailed final state properties. In all models (e.g. independent, string or cluster hadronisation) the kinematic properties of a jet are strongly correlated with those of the parton from which it evolved. This is not only true in the case of independent fragmentation, where one expects a direct relation, but also for models where, as a matter of principle, one cannot unambiguously associate a given final hadron with a specific parton.

The basic, or lowest order, parton level process must be corrected for higher order perturbative QCD effects causing the emission of extra partons on a short space-time scale before hadronisation. These can either be calculated by exact matrix elements, which has so far only been done to low orders in the strong coupling α_s, or approximately by so called parton showers based on the iteration (to arbitrary order in the coupling α_s) of the basic quark (q) and gluon (g) radiation processes $q \to qg$, $g \to gg$ and $g \to q\bar{q}$. Due to the bremsstrahlung nature of this radiation, most partons will be soft (low-energy) or collinear with the emitting parton. Hence they will not give rise to separately observable jets, but rather to a softening of the hadron momenta and broadening of the jet corresponding to the original parton. At a reduced rate, however, hard emission at large angles does occur which gives rise to observable extra jets. In order to establish a correlation between a jet and a single parton one therefore has to correctly account for both the parton emission process and the hadronisation process. Two jets will be individually observed in a detector only if they are separated by a distance which is at least as large as the lateral dimensions of the jets. On the parton level this corresponds to fairly high parton momenta and a certain angular separation.

Ever since the first observation of jet structure in e^+e^- collisions the question of how to define jets has been controversial. The picture of a jet as a collimated flow of particles implies that a minimum energy must be available for the jet formation. In particular, the particle momenta along the parton momentum direction must be much larger than the transverse momentum fluctuations induced in the hadronisation process. As the parton momentum increases, the jets tend to become more pencil-like which simplifies their identification. Experimentally, it is found that 2-jet systems, e.g. in $e^+e^- \to q\bar{q}$, can only be observed as containing two visible jets if the invariant mass is at least 10 GeV [1]. This sets a lower limit on the invariant mass of systems to which jet algorithms should be applied.

Different types of jet-finding algorithms have been developed to provide a way of reconstructing jets but since the definition of a jet is not unique, the algorithms all include a parameter which specifies the desired resolution. The danger in blindly relying upon a jet-algorithm lies in the fact that most algorithms will find jets, even if the event is completely spherical and contains no collimated flows of particles. Unphysical results may also be produced with an exagerated jet resolution that splits a well collimated particle flow from a single parton into two jets, or a too coarse jet resolution that joins two separately detectable clusters of particles from different partons into a single jet. The outcome of the jet reconstruction is thus dependent upon the algorithm that has been used and how the resolution parameter has been set.

Clearly, one needs proper guidance in the choice of jet reconstruction algorithm and the value of its jet resolution parameter. Unfortunately, there is no unique 'best choice' since it depends on the purpose for which the jets are being reconstructed. If one only wishes to demonstrate the occurrence of multi-jet events the choice is not so critical as when quantitative tests of QCD are to be made, such as measuring the strong coupling constant α_s. Since the latter requires a well-defined renormalisation scheme to be fully significant, one must invoke exact QCD matrix elements rather than leading logarithm parton shower models. A jet algorithm which is defined such that it can be imposed on analytical matrix element calculations is therefore necessary to enable a direct comparison or to fit data to the theory. Such investigations based on jets are the most interesting, but also the most challenging with respect to the jet reconstruction. It has to be tuned so as to reconstruct mainly the hard parton emission calculable with exact matrix elements that are only available in leading and next-to-leading order in α_s. The sensitivity to higher order emissions, which can only be calculated approximately, should be minimized by effectively merging the outcome of such extra, softer parton emissions with the few harder jets that can be associated with the matrix element calculation.

Due to the complexity of the event structure and the jet algorithms, these probems can in practice only be investigated through Monte Carlo simulation of complete events based on the theories of electroweak interaction and QCD for the hard processes and a model for the hadronisation. To study the physics, one may first use exact QCD matrix elements only and neglect the approximate higher order emissions. This is also of advantage for our study of jet-finding algorithms, since it is then possible to formulate unambiguous quality measures of how well the reconstructed jets correspond to a well-defined underlying parton level system. With higher orders giving many but softer partons, which may or may not give observable jets, this becomes an ill-defined problem. Our approach is therefore to assess the quality of jet reconstruction algorithms applied to Monte Carlo generated events with first order QCD effects only. The best performance of the algorithms in reconstructing the partons in such matrix element events will consequently determine proper values of the resolution parameters. Once these values are specified, the effects of higher order emissions simulated through parton showers are added to investigate how the quality of the reconstruction is modified.

Previous studies [2] have mostly investigated the quality of reconstruction by applying jet algorithms to the multi-parton state generated by parton showers and to the same events after hadronisation. The test of the algorithm is then restricted to a comparison between the reconstructed parton jets and the reconstructed hadron jets. Hence, an algorithm which makes the same mistakes on the parton and hadron level will appear better than it really is. With this type of analysis one is mainly determining how sensitive an algorithm is to the hadronisation process and not how well it will reconstruct the hard matrix element.

A further motivation for this new study of jet reconstruction at HERA is that some recently proposed algorithms need to be investigated and compared with the old ones. We have therefore performed a systematic study of five jet algorithms: Jade [3], Luclus [4], Lucell [5], Arclus [6] and K_T [7]. Their ability to reconstruct jets in HERA *ep* collider events is examined with the purpose of extracting information on hard parton emission processes. In Sect. 2 we discuss the characteristics of event and jet topologies at HERA. Section 3 describes the Monte Carlo event generation, and the five jet algorithms are defined and briefly discussed in Sect. 4. In Sect. 5 we present the main results, starting with the general behaviour of the algorithms and how to measure their performance, followed by results on the reconstruction of the hard subsystem and the parton four-momenta. Finally, the effects of higher order parton emissions are investigated. In Sect. 6 we present the conclusions of this study.

2 Event characteristics at HERA

At HERA, 26.7 GeV electrons collide with 820 GeV protons giving an energy of 296 GeV in the cms. The four-momenta p_e, P, q and p_ℓ represent the incoming electron, incoming proton, the exchanged boson and the scattered lepton (cf. Fig. 1a). The basic kinematic variables for deep-inelastic scattering (DIS) are then given by

$$Q^2 \equiv -q^2 = -(p_e - p_\ell)^2, \quad x \equiv \frac{Q^2}{2P\cdot q}, \quad y \equiv \frac{P\cdot q}{P\cdot p_e},$$
$$W^2 \equiv (q+P)^2 = Q^2\,\frac{1-x}{x} + m_p^2, \tag{1}$$

which specify the momentum transfer squared, the Bjorken-x and y scaling variables, and the invariant mass squared of the hadronic system. Only two of these variables are independent.

The major difference between reconstructing jets in e^+e^- events compared with ep events is due to the presence of the spectator jet in the latter case. This jet, which travels in the proton beam direction, originates from that

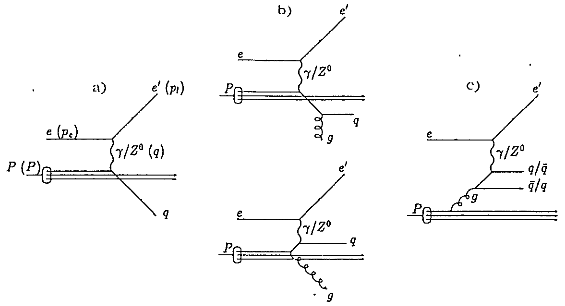

Fig. 1a–c. Deep inelastic *ep* scattering at HERA with **a** the leading order QPM process and the first order QCD processes **b** QCD Compton and **c** boson-gluon fusion (BGF)

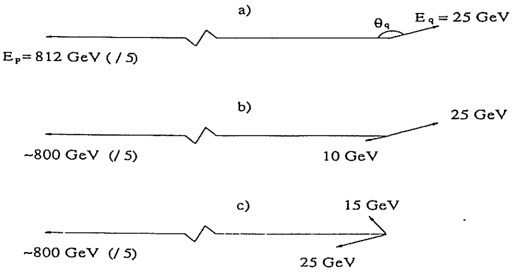

Fig. 2a. The parton momentum-vectors in a QPM event with $x=0.01$ and $y=0.9$. **b** A 'typical' boson-gluon fusion event with $x=0.01$ and $y=0.9$. **c** A 'typical' boson-gluon fusion event with $x=0.01$ and $y=0.09$

part of the proton which does not take part in the hard scattering process. The spectator jet is, in most analyses, of no interest and the fact that a major part of this jet remains undetected within the beam pipe does usually not cause any problems. However, if part of it enters the detector it may upset or even spoil the reconstruction of the jets associated with the hard scattering, henceforth called current jets.

The energy of the spectator jet is usually very high at HERA. Only events with high x values will have current jets with energy similar to the spectator jet. This is easily understood with the help of the naive quark parton model (QPM) in which x is the fraction of the proton momentum carried by the struck quark and the energy of the spectator jet is given by $(1-x)\,E_p$. Since the cross section is large at small x (and consequently also small Q^2) most HERA events have $x \ll 0.1$ and, with naive QPM kinematics, a spectator jet with an energy greater than 700 GeV. Thus, the normal situation is that most of the energy goes into the spectator jet.

In e^+e^- collisions the total centre-of-mass energy ($\sqrt{s}$) is available in the hard scattering to produce jets. The invariant mass of the hadronic final state, W, is here equal to $\sqrt{s}$, such that the phase space for QCD jet production is directly given by W. This differs from ep collisions where the initial momentum fraction of the scattered parton regulates how much energy is available for hard QCD jet production and how much goes into the spectator jet.

The leading order process (zero order in QCD) in Fig. 1a contains only one current jet. This type of events will be called $1+1$ jet events to account for both the current jet and the spectator jet. The invariant mass squared of the hadronic final state can, in a massless approximation, be written as:

$$W^2 = 2(1-x)\,E_p\,E_q(1-\cos\theta_q), \tag{2}$$

where E_q is the energy of the struck quark and θ_q is its scattering angle with respect to the proton beam direction, see Fig. 2a. We notice that the separation between the spectator jet and the current jet is directly correlated to W^2. In addition, E_q, θ_q and the azimuthal angle, ϕ_q, of the struck quark, can be calculated from Q^2, y and the azimuthal angle of the scattered electron, ϕ_e, using the following relations:

$$\begin{aligned} E_q &= yE_e + \frac{Q^2(1-y)}{4E_e\,y}, \\ \cos\theta_q &= 1 - \frac{2E_e\,y}{E_q}, \\ \phi_q &= \phi_e + \pi. \end{aligned} \tag{3}$$

While the 4-momentum of the current jet in the QPM case can be calculated directly from Q^2 and y, the first order QCD processes have three more degrees of freedom describing the internal structure of the $2+1$ jet system. The two possible processes in this case are the QCD-Compton process where a gluon is emitted from the quark (see Fig. 1b), and the boson-gluon fusion process where a gluon from the proton interacts with the virtual photon to give a quark-antiquark pair (Fig. 1c). The mass of the total hadronic system in a boson-gluon fusion event can (when neglecting parton masses) be written as a sum of three terms:

$$W^2 = m_{pq}^2 + m_{p\bar{q}}^2 + \hat{s}. \tag{4}$$

Here $m_{pq/\bar{q}}$ is the invariant mass of the spectator jet and the quark/antiquark jet while $\sqrt{\hat{s}}$ is the invariant mass of the two current-jets. Obviously, the expression above is also true for a QCD-Compton even if $m_{p\bar{q}}^2$ is changed to m_{pg}^2 which then denotes the invariant mass of the spectator jet and the gluon jet.

With ξ denoting the momentum fraction of the parton entering the first order QCD process, the energy of the spectator jet is $(1-\xi)\,E_p$. With massless partons one obtains:

$$\begin{aligned} m_{pq}^2 &= 2(1-\xi)\,E_p\,E_q(1-\cos\theta_{pq}), \\ m_{p\bar{q}}^2 &= 2(1-\xi)\,E_p\,E_{\bar{q}}(1-\cos\theta_{p\bar{q}}), \\ \hat{s} &= 2E_q\,E_{\bar{q}}(1-\cos\theta_{q\bar{q}}), \end{aligned} \tag{5}$$

where E_q and $E_{\bar{q}}$ are the energies of the quark and antiquark jet, respectively and θ_{pq}, $\theta_{p\bar{q}}$ and $\theta_{q\bar{q}}$ are the angles between the jets. Although ξ can have any value in the range $x < \xi < 1$, small x values are still correlated with

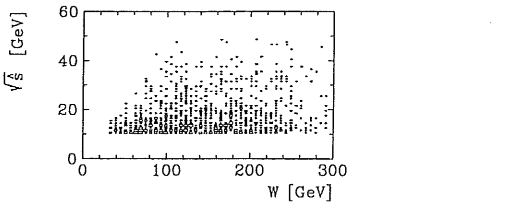

Fig. 3. Scatter plot of the invariant mass of the current jets ($\sqrt{\hat{s}}$) and the total hadronic mass (W) for a sample of ME events

small ξ such that typically $(1-\xi)\,E_p \gg E_q$ and $E_{\bar{q}}$. Therefore, W^2 will be dominated by the two terms m_{pq}^2 and $m_{p\bar{q}}^2$ involving the spectator, cf. Fig. 2b and c. This means that high values of W do not neccessarily correspond to high values of the hard subsystem mass $\sqrt{\hat{s}}$. In the event samples with 2+1 jets produced at HERA it is therefore not enough to study the jet reconstruction as a function of W. Also, $\sqrt{\hat{s}}$ must be considered, as demonstrated more explicitly in Fig. 3. In this scatterplot no strong correlation between $\sqrt{\hat{s}}$ and W can be seen. In conclusion, while the energies and the separation of the spectator jet and the current jet in a 1+1 jet event are correlated with W, the invariant mass of the hard subsystem in a 2+1 jet event is not. Therefore, one cannot use W in ep collisions in the same way as one uses W in e^+e^- collisions.

3 Event generation

To study the performance of the jet algorithms it is preferable to apply them to Monte Carlo generated events. The available knowledge about the underlying parton process can then be used to judge the correctness of the jet assignment. We use the program Lepto 6.1 [8] which is known to reproduce the DIS data from previous lepton-nucleon scattering at fixed target energies [9] and also to give a fair description of the limited data presently available from HERA [10].

Lepto simulates the basic deep-inelastic scattering at the parton level and we have chosen to consider the dominating neutral current process. In addition to the leading order QPM process, $\gamma^* q \to q$, also the first order (α_s) processes of gluon radiation, i.e. QCD-Compton, $\gamma^* q \to qg$, and boson-gluon fusion, $\gamma^* g \to q\bar{q}$, are included based on the QCD matrix elements (ME). In accordance with our desire to have a well-defined underlying parton level process for our test of the jet reconstruction algorithms, we have switched off higher order QCD parton emission processes. To check the effects of such higher order corrections we later include them through the parton shower (PS) option available in the program. The QCD matrix elements have the usual divergences for soft and colinear emission, which are avoided by a requirement of a minimum invariant mass m_{ij} of the resulting parton pairs. This is normally implemented by the cut $m_{ij}^2 \geqq y_{\text{cut}}\, W^2$ (see PARL(8) and PARL(9) in [8]). With standard values of y_{cut} in the region 0.015 to 0.0025, this gives hard scattering subsystem masses $\sqrt{\hat{s}} = m_{ij}$ down to a few GeV at small W. As discussed above, jet structures cannot be observed at such small masses and we therefore instead used a fixed cut $m_{ij} \geqq 10$ GeV. By not letting the cut scale with W we avoid introducing a bias in the relation between $\sqrt{\hat{s}}$ and W. This relation, see Fig. 3, is of interest for our investigation of how the jet resolution parameter should change with varying ep scattering kinematics (in particular W) in order to obtain an optimal jet reconstruction.

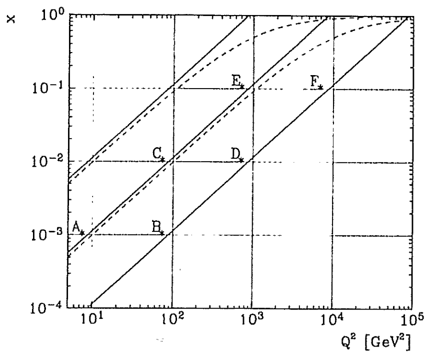

Fig. 4. The x and Q^2 values of the generated six event samples $A-F$. The diagonal full lines represent constant $y\,(=0.01, 0.1, 1,$ top to bottom) and the dashed lines constant W^2 $(=10^3, 10^4\ \text{GeV}^2)$

Detector effects on the generated events have been neglected, except for a requirement of particles to be within the overall acceptance of the detector, i.e. have a minimum angle of 4° to the beam line. Since HERA covers a wide range in x and Q^2, with large variations in the event topologies, one must investigate the performance of the jet algorithms as a function of the basic scattering kinematics. We have therefore chosen to generate six event samples ($A-F$) at fixed x and Q^2, see Fig. 4, representing a kinematic region where these overall event variables can be reasonably well measured by the detector.

4 Description of jet algorithms

We have investigated five different jet algorithms in order to find the one best suited for reconstructing multi-jet events at HERA. All five algorithms use a set of 4-vectors, representing the 4-momenta of the particles in an event, as input and the 4-vectors of the reconstructed jets are provided as output. The algorithms contain a cut-off parameter which determines the resolution of the jet reconstruction. If, however, the resolution depends on the kinematic region in which the algorithm is applied, a suitable scaling variable has to be found to account for this kinematic dependence. The six specific event samples mentioned above have been used to study whether there is such a dependence and, if so, to find the relevant scaling variable. In this investigation we have initially not included any scaling variables in the jet algorithms. Scaling is not needed for an event sample with fixed x and Q^2 and different optimal cut-off values for event samples at different x and Q^2 values will thus indicate the necessity of scaling.

4.1 *Jade*

The jet reconstruction procedure of the Jade algorithm [3] starts by calculating the distance parameter m_{ij} for all pairs of particles according to the expression:

$$m_{ij}^2 = 2E_i E_j (1 - \cos\theta_{ij}), \tag{6}$$

where E_i and E_j are the energies of particles i and j and θ_{ij} is the angle between them. The parameter m_{ij} is the invariant mass of particles i and j under the approximation that both i and j are massless. The pair with the smallest m_{ij} is combined into a cluster. This combination can be made according to different schemes [11, 12] where the natural choice of adding their four-vectors is made in the following so as to conserve energy and momentum and obtain massive jets. The procedure is repeated until all remaining pairs have an invariant mass exceeding a preselected cut-off value, $m_{ij}^2 > y_{\text{cut}} M^2$, determined by a resolution parameter y_{cut} and a reference mass M (in this study initially set to 1). The final clusters represent the jets of the event.

4.2 *Luclus*

The Luclus algorithm [4] uses a similar clustering scheme to Jade but the distance parameter is

$$d_{\text{join}}^2 = \frac{2(|\bar{P}_i|\,|\bar{P}_j| - \bar{P}_i \cdot \bar{P}_j)\,\bar{P}_i \cdot \bar{P}_j}{(\bar{P}_i + \bar{P}_j)^2}, \tag{7}$$

where $\bar{P}_i$ and $\bar{P}_j$ are the 3-momenta of two particles or clusters. For small angles between $\bar{P}_i$ and $\bar{P}_j$ one can interpret d_{join} as the transverse momentum of i (or j) with respect to the direction given by the sum of $\bar{P}_i$ and $\bar{P}_j$. An additional feature of Luclus, which we have used, is the option to reassign particles to new clusters as the clustering procedure progresses.

4.3 *Lucell (ΔR-cone)*

Another approach to jet reconstruction is to form cones around localised flows of energy. This was originally developed for $p\bar{p}$ colliders by the UA1 collaboration [13] and we use the equivalent algorithm Lucell in [5]. The total solid angle coverage of the detector is subdivided into equal cells in pseudorapidity ($\eta = -\ln\tan\theta/2$) and azimuthal angle (ϕ). The deposited transverse energy ($E_\perp = E\sin\theta$) is summed in each cell and all cells with $E_\perp$ greater than a preselected value are taken as possible initiators of jets. Taking these initiators in falling $E_\perp$ sequence, the algorithm checks if the total transverse energy in a cone around the initiator cell exceeds a minimum, $E_{\perp\,\text{min}}$. If so, these cells define a jet and are removed from further considerations. The jet energy is given by the cells and its direction by their energy-weighted centre. The cone size is given by $\Delta R = \sqrt{\Delta\eta^2 + \Delta\phi^2}$, which in our study is set to 1 and the minimum initiator energy is 0.3 GeV. With this scheme not all particles are necessarily assigned to jets.

4.4 *Arclus*

The Arclus algorithm [6] is closely related to the colour dipole model CDM [14], where the emission of a gluon from a $q\bar{q}$ pair is treated as radiation from a colour dipole formed by the quark and the antiquark. A major difference between Arclus on one hand and Jade, K_T and Luclus on the other is that Arclus considers all possible combinations of three particles instead of two. The idea is to regard each combination of three clusters (i, j and k) as two clusters forming a dipole which radiates a third cluster.

Since Arclus works with three particles/clusters instead of two, Arclus calculates a parameter called $P_\perp$ three times. Initially,

$$P_{\perp k}^2 = m_{ijk}^2 \left(1 - x_i + \frac{m_i^2 - (m_k + m_j)^2}{m_{ijk}^2}\right) \cdot \left(1 - x_j + \frac{m_j^2 - (m_k + m_i)^2}{m_{ijk}^2}\right) \tag{8}$$

is calculated, with $x_i = 2E_i/m_{ijk}$ where E_i is the energy of particle/cluster i in the centre-of-mass system of particle i, j and k and m_{ijk} is the invariant mass of these particles. The masses m_i, m_j and m_k of the three individual particles are usually set to zero which reduces (8) to

$$P_{\perp k}^2 = m_{ijk}^2 (1 - x_i)(1 - x_j) = \frac{m_{ik}\, m_{jk}}{m_{ijk}}, \tag{9}$$

where m_{ik} is the mass of particles i and k and m_{jk} is the mass of particles j and k.

Since the $P_{\perp k}^2$ defined by (9) is calculated from three Lorentz invariant masses it is obvious that $P_{\perp k}^2$ is also Lorentz invariant. What is perhaps less obvious is that for small energies of k (in the cms of i, j and k) or for small angles of k with respect to i or j the two clusters i and j will be almost back-to-back and $P_{\perp k}$ is then the transverse momentum of k with respect to the direction of i and j.

In the algorithm not only $P_{\perp k}$ is used but also the two other possible $P_\perp$ values ($P_{\perp i}$ and $P_{\perp j}$) are calculated. This is repeated for all combinations of three particles. The smallest $P_\perp$ is compared with a resolution parameter $P_{\perp\,\text{min}}$ and if it is smaller than this parameter the three particles/clusters which gave the smallest $P_\perp$ are replaced by two new clusters, n and m, in the following way.

The two massless clusters n and m are required to have an invariant mass (m_{nm}) which is equal to the invariant mass of the original three clusters (m_{ijk}) and momentum vectors, $\bar{P}_n$ and $\bar{P}_m$, that are equal in magnitude but oppositely directed along a fixed axis*. In the cms of the three original clusters $\bar{P}_i+\bar{P}_j+\bar{P}_k=\bar{0}$ and thus $m_{ijk}=E_i+E_j+E_k$. Since the two new clusters n and m also have $\bar{P}_n+\bar{P}_m=\bar{0}$ and $m_{nm}=E_n+E_m$ the requirements of $\bar{P}_n=-\bar{P}_m$ and $m_{nm}=m_{ijk}$ ensure momentum and energy conservation in the clustering process (provided the original hadrons in the event are assumed to be massless).

The two resulting clusters are boosted back to the laboratory system and the procedure is repeated until all combinations have a $P_\perp$ larger than the specified resolution scale $P_{\perp\,\mathrm{min}}$. The remaining clusters are the jets. With this procedure no hadron will be uniquely assigned to one specific jet but its momentum is shared by two jets and the minimum number of jets found by Arclus is two, i.e. in our case 1+1 jets.

4.5 K_T

A two-step procedure, similar to the one we have proposed in an earlier study [15] for the Jade algorithm, is used in the K_T algorithm [7] for DIS processes, where the first step comprises preclustering of hadrons into a beam jet and so-called final state macro-jets. A second step aims at resolving jet structures within the system of macro-jets.

In the preclustering, a variable K_{Tij} is calculated for all pairs of particles/clusters i and j according to the scheme:

$$K_{Tij}^2=2(1-\cos\theta_{ij})\min(E_i^2,E_j^2), \tag{10}$$

where θ_{ij} is the angle between the momentum vectors of i and j and E_i and E_j are the corresponding energies. In addition, a second variable K_{Tip} is calculated for all particles/clusters i according to:

$$K_{Tip}^2=2(1-\cos\theta_{ip})\,E_i^2, \tag{11}$$

where θ_{ip} is the angle between i and the proton direction.

One specific feature of the K_T algorithm for DIS processes is that all quantities (E_i, E_j, θ_{ij} and θ_{ip}) are calculated in the Breit frame, i.e. where the exchanged vector boson has the four-vector $q=(0,0,0,-Q)$. The boson and proton are here both along a common axis, but longitudinally boosted compared with their centre-of-mass system. Consequently, for small angles and for $E_i\leq E_j$, K_{Tij} can be regarded as the transverse momentum, in the Breit frame, of i with respect to the direction of j while K_{Tip} can be regarded as the transverse momentum of i with respect to the proton direction.

At this stage a new variable ($E_\perp$) is introduced in the algorithm and

$$y_{ij}=\frac{K_{Tij}^2}{E_\perp^2}, \qquad y_{ip}=\frac{K_{Tip}^2}{E_\perp^2}, \tag{12}$$

are calculated. The algorithm proceeds by checking if the smallest y value obtained is less than one. If this is the case and the y value is of the type y_{ij} then i and j are combined to a new cluster, preserving both energy and momentum. If, on the other hand, the smallest y value is of the type y_{ip} then i is regarded as part of the spectator jet and is removed from further treatment. The procedure is repeated until all y values are larger than one. In other words, the algorithm checks whether $\min(K_{Tij}^2, K_{Tip}^2)<E_\perp^2$ in which case either two clusters are combined or one cluster is assigned to the spectator jet. One can therefore regard $E_\perp^2$ as the resolution parameter in the algorithm's first step which tries to separate the spectator jet from the macro-jets.

In the algorithm proposed by [7], the algorithm then continues with a second step in which a parameter Q_0 is introduced and the variable $y_{\mathrm{cut}}=Q_0^2/E_\perp^2$ is calculated ($E_\perp^2$ remains the same as for step one). All particles in the event which were not assigned to the spectator jet in step one are used again. For every pair of particles the y_{ij} value is calculated and the pair giving the smallest y value is compared with the y_{cut} value. If $y_{ij}<y_{\mathrm{cut}}$ the hadrons are combined into a cluster. When all y values exceed the y_{cut} value the procedure is stopped and the remaining clusters are the final jets. In fact, what is done in this step, is to test if $K_{Tij}^2<Q_0^2$, in which case the clusters i and j are combined to form a new cluster. The parameter Q_0 is thus a second resolution parameter which is used to resolve the macro-jets.

It can be added that for our purposes and with the method of chosing $E_\perp^2$ that we have developed (this method will be described below), the second step is not needed and the jets found in the first step can be used directly. We therefore do not discuss the Q_0 parameter further.

4.6 Theoretical considerations

The choice of jet algorithm depends on what kind of physics analysis is to be made with the reconstructed jets. In order to obtain a proper comparison with theoretical results the jet definition should also be applicable in the theoretical calculations. The invariant mass cut used in Jade is suitable for fixed order matrix element calculations where it is often used as the basic cut-off against divergences. This works theoretically well as long as the resolution y_{cut} is not too small. At small y_{cut}, however, higher order corrections become enhanced by powers of $\ln y_{\mathrm{cut}}$ and certain resummation techniques are then necessary. In particular, the large logarithmic corrections to the relevant quantity may then exponentiate. As discussed in [16], the K_T algorithm is preferable under such circumstances since its use of transverse momentum to resolve jets is suggested by the coherence properties of soft QCD emission processes in order to preserve the exponentiation. The other algorithms do not have this property (it has been suggested [6] that it might hold for Arclus). The distance measure d_{join} and ΔR used in Luclus and Lucell, as well as the complexity of Arclus make these algorithms unsuitable for analytical QCD calculations. However, in applications where the

---

* The direction of this axis is given by $\theta_i=\frac{x_j^2}{x_i^2+x_j^2}(\pi-\psi)$ where θ_i is the polar angle between the axis and particle i and ψ is the angle between particles i and j. This axis is chosen so that the sum of the transverse momentum squared of particles i and j with respect to this axis is minimized

theory can be considered to be treated well enough by a Monte Carlo program that generates complete final states, the choice of algorithm can be made more freely since practically any jet definition can then be applied to the theoretical events in the same way as to the data. For a study of some of these jet algorithms applied to e^+e^- annihilation see [12], where the corresponding next-to-leading order QCD and hadronisation corrections are also investigated. For DIS, the importance of factorization and the special role of the Breit system have been emphasized and discussed for the Jade and K_T type of algorithms in [17].

5 Performance of jet algorithms

In the comparison of jet algorithms we use a sample of 2+1 jet events generated from first order α_s matrix elements. As explained in Sect. 3, only events which fulfill the requirement of a mass cut $m_{ij} \geqq 10$ GeV for all pairs of partons in the event, are accepted. This is to ensure reasonably clear jet structures.

As discussed, the proton remnant continues in the direction of the incoming proton and produces a jet which, to a large extent, escapes down the beam pipe without detection. Some fringe particles might, however, hit the detector and must be treated correctly by the jet algorithm. This can be achieved by inserting a pseudoparticle with the direction of the incoming proton and only longitudinal momentum which is determined from the known longitudinal momentum of the initial state and the measurable longitudinal momentum of final particles outside the beam pipe. This pseudoparticle is treated like any other particle in the jet reconstruction procedure (for details see [18]).

A good starting point in the jet reconstruction procedure is to separate the spectator jet from the hard subsystem. If this separation is not optimized, the reconstruction of the jets from the hard subprocess can be highly distorted by the very energetic spectator jet. In Sect. 5.1 and 5.2 we therefore focus on optimizing the reconstruction of the spectator jet which corresponds to reconstructing the invariant mass of the hard subsystem, $\sqrt{\hat{s}}$. At this stage we do not concern ourselves with the structure of the subsystem itself. This is treated in Sect. 5.3 where we investigate how well the jet multiplicity and the parton four-momenta are reproduced. Finally, the effect of higher order parton emissions is studied in Sect. 5.4.

5.1 General behaviour

As shown for Luclus in Fig. 5 the distribution of the difference between the generated $\sqrt{\hat{s}}$ and the reconstructed invariant mass $\sqrt{\hat{s}_{\text{rec}}}$ exhibits different shapes depending on how the cut-off value of the resolution parameter is chosen. At low cut-off values, the reconstructed invariant mass has a tendency to be too high and there is a tail on the negative side of the distribution, Fig. 5a. This tail indicates that particles from the spectator jet have been included in the hard subsystem by the jet algorithm. At a somewhat higher cut-off value, Fig. 5b, the negative tail decreases and there is a narrow peak centred at zero but an additional bump at positive values appears. This bump corresponds to events where some particles or an entire jet, related to the hard subprocess, have been assigned to the spectator jet, resulting in too low a $\sqrt{\hat{s}_{\text{rec}}}$. Finally, at high cut-off values, Fig. 5c, the negative tail is even less pronounced and the bump at positive values has grown. This is a general behaviour of all the algorithms studied. The ideal distribution would of course be a narrow peak centred at zero with no tail on the negative side and no bump at positive values.

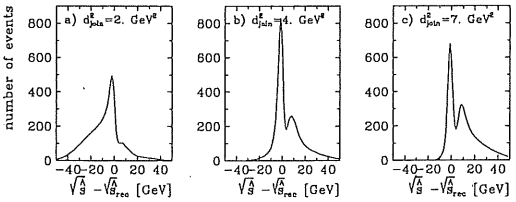

Fig. 5. The difference between the generated and reconstructed invariant mass ($\sqrt{\hat{s}}$) of the current jets, using Luclus with three values of the resolution parameter d^2_{join}

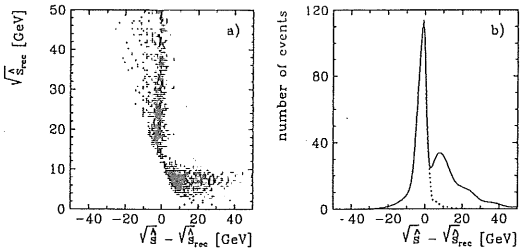

Fig. 6. **a** Scatter plot of $\sqrt{\hat{s}}$ versus $\sqrt{\hat{s}}-\sqrt{\hat{s}_{\text{rec}}}$. **b** The distribution of $\sqrt{\hat{s}}-\sqrt{\hat{s}_{\text{rec}}}$ before (full line) and after (dashed line) a mass cut of $\sqrt{\hat{s}_{\text{rec}}} > 15$ GeV

In order to approach this ideal situation one can use the fact that there is a correlation between the values of $\sqrt{\hat{s}_{\text{rec}}}$ and $\sqrt{\hat{s}}-\sqrt{\hat{s}_{\text{rec}}}$ as is demonstrated in Fig. 6. A lower mass cut in $\sqrt{\hat{s}_{\text{rec}}}$ of for example 15 GeV removes the bump at positive values entirely and a high enough cut-off value for the resolution parameter surpresses the tail. Such a mass cut also corresponds to the lower limit above which clear jet structures might be observed. However, the effect of the mass cut is a decrease in the event sample and since an increasing number of events will populate the bump as the algorithm cut-off value increases, the remaining sample will decrease with increasing cut-off value. The precision of the reconstruction will, however, improve. The events that are lost by the mass cut are those where the spectator jet is not clearly separated from the hard subsystem, i.e. where one of the

Table 1. Jet algorithm cut-off values used for event samples *C* and *D*. The roman numerals in the head of the table are used to correlate the cut-off values for an algorithm with the points plotted in Figs. 8–10. Increasing numbers correspond to increasing cut-off values, i.e. decreasing fraction of remaining 2+1 jet events

Event sample *C*	X	IX	VIII	VII	VI	V	IV	III	II	I
Jade	1300	1100	900	700	500	400	300	200	100	30
Luclus	6.0	5.0	3.8	3.4	3.0	2.6	2.2	1.8	1.4	0.7
Lucell	6.0	5.0	4.0	3.0	2.5	2.0	1.5	1.2	0.7	0.2
K_T	50.0	40.0	30.0	20.0	10.0	5.0	3.0	2.0	1.5	1.0
Arclus	84.0	64.0	48.0	32.0	24.0	14.0	6.0	2.0	1.0	0.2
Event sample *D*	**x**	**ix**	**viii**	**vii**	**vi**	**v**	**iv**	**iii**	**ii**	**i**
Jade	95000	80000	20000	5000	1000	500	200	100	50	20
Luclus	18.0	10.0	7.0	5.0	3.8	3.4	3.0	2.6	2.2	1.8
Lucell	10.0	8.0	6.0	5.0	4.0	3.5	3.0	2.5	2.0	1.5
K_T	140.0	80.0	50.0	40.0	30.0	20.0	10.0	5.0	3.0	2.0
Arclus	140.0	100.0	80.0	60.0	40.0	32.0	24.0	16.0	8.0	4.0

jets from the subsystem goes in the very forward direction. These events are almost impossible to reconstruct in an accurate way and the loss is therefore difficult to avoid.

In this study we have selected three observables which provide information about the reconstruction of $\sqrt{\hat{s}}$. Two of these observables, the full width half maximum (fwhm) and the root mean square (rms) describe the width of the $\sqrt{\hat{s}}-\sqrt{\hat{s}_{\text{rec}}}$ distribution. (The latter is more sensitive to contributions from the tails.) The third observable is the mean value which was used to measure systematic shifts of the distribution.

The five jet algorithms were applied to an event sample using ten different cut-off values of the resolution parameter for each algorithm. (The cut-off values used in event samples *C* and *D* are given as an example in Table 1.) For each value, the fraction of 2+1 jet events surviving the mass cut and the three observables describing the $\sqrt{\hat{s}}-\sqrt{\hat{s}_{\text{rec}}}$ distribution were measured. These observables were then plotted as a function of the fraction of events remaining after the 15 GeV mass cut. This method of presenting the results is motivated by the fact that in most analyses one must find a compromise between the statistics needed and the precision required. Another motivation is that the properties of the different algorithms can be directly compared despite their different separation criteria and cut-off values. The investigation was repeated for all six event samples to see how the quality of the reconstruction changed and if a universal cut-off value in the algorithms could be found for the entire kinematic range studied.

Results from samples with equal *W* (*A*, *C*, *E* and *B*, *D*, *F* respectively) have a similar correlation between the three reconstruction observables and the cut-off values of the resolution parameters. A possible explanation for this is that events of equal *W* have similar event topologies. This can be realised from studying Fig. 7a and b where the polar angle with respect to the proton beam direction of the two current jets are plotted against each other. Low and high *W* values are exemplified by the event samples *C* and *D*. At low *W* (Fig. 7a) both jets are most likely to be found in the forward region, i.e. the polar angles are small. This is also shown in Fig. 2c which describes a typical *C* event. The high *W* events (Fig. 7b) most often have one jet in the forward direction and the other jet in the backward direction with a θ value of around 160°. This is exemplified in Fig. 2b which shows a typical *D* event. At the parton level, ignoring initial state parton showers, the relationship between the θ values of the jets can be expressed in a massless approximation by

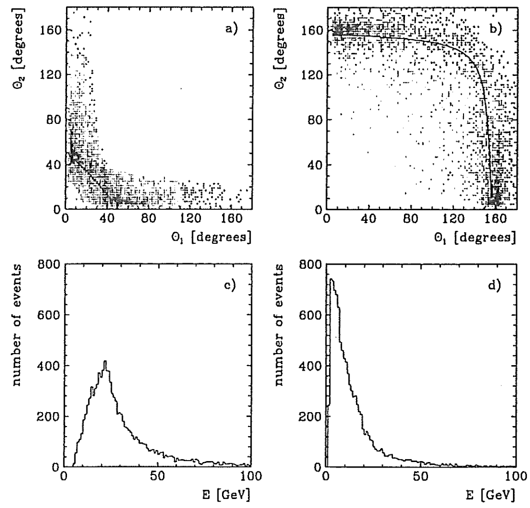

Fig. 7. **a** The angles of the two partons of the first order QCD matrix element with respect to the proton direction for event sample *C* ($W^2=7920$ GeV^2) and **b** for event sample *D* ($W^2=79200$ GeV^2). **c** Energy of the parton closest to the spectator jet for event sample *C* and **d** for event sample *D*

$$2yE_e=E_{\perp 1}\tan\frac{\theta_1}{2}+E_{\perp 2}\tan\frac{\theta_2}{2}, \tag{13}$$

where $E_{\perp i}$ is the transverse energy of jet i. At low x ($x<0.1$) we can, to a good approximation, assume that $y \approx W^2/s$ (see Fig. 4) and (13) then gives the energy and angular correlations between the two jets and W. Taking the average values of $E_{\perp i}$ for both jets (≈ 10 GeV), we have from (13) calculated the correlation curve for the polar angles and depicted it in the scatter plots 7a and b. Since the jet angles are mainly correlated to W we present the results below only for two samples (C and D) with different W. Results from the other four event samples will only be given in the form of summary tables.

5.2 Reconstruction of the hard scattering subsystem

Figures 8 and 9 shows, for event samples C and D respectively, the three observables, fwhm, rms and the mean value of the $\sqrt{\hat{s}}-\sqrt{\hat{s}_{\mathrm{rec}}}$ distribution, versus the remaining fraction of events as the resolution parameters are varied in the five jet algorithms. Each point in these figures corresponds to a specific cut-off value given in Table 1.

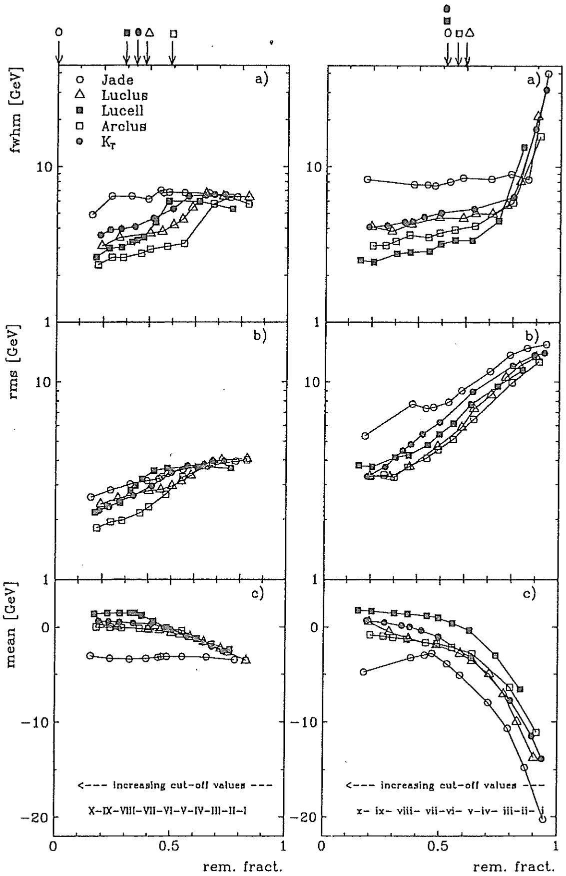

Fig. 8 and **Fig. 9.** Quality measures (y axis) of reconstructed $\sqrt{\hat{s}}$ (invariant mass of hard scattering system) versus remaining fraction of the event sample (x axis) obtained with the indicated jet algorithms applied to event samples C (**Fig. 8**) and D (**Fig. 9**). The points correspond to the cut-off values specified in Table 1 and the arrows at the top indicate chosen cut-off values as described in the text

Comparing the results of the five jet algorithms we note that the Jade algorithm reconstructs $\sqrt{\hat{s}}$ less well than the other four. In almost all respects it gives worse results, i.e. higher values of fwhm and rms (at least at high W), and a mean value different from zero. Arclus seems to perform somewhat better than the other algorithms at low values of W.

Another observation is that the reconstruction of $\sqrt{\hat{s}}$ seems to be better at low (Fig. 8) rather than at high values of W (Fig. 9). The variation in the three reconstruction observables is also much smaller at low W than at high W, making the choice of cut-off values less critical at low W values.

According to Figs. 8 and 9 the quality of the $\sqrt{\hat{s}}$ reconstruction generally improves with increasing cut-off values and consequently an unambiguous cut-off value cannot be found. However, at least for high W we clearly observe that the curves level off which means that the quality in the reconstruction no longer improves significantly with increasing cut-off value; only the statistics is reduced further. This behaviour therefore gives an indication of how to make a reasonable choice of cut-off values. The curves describing the mean value (Fig. 9c) level off at somewhat higher cut-off values than is the case for the curves describing the fwhm (Fig. 9a). Our choice of cut-off values is thus mainly determined by the observed behaviour of the mean value at high W. This method of choosing the cut-off values is of course qualitative and, considering the dependence of rms, governed by the importance of good statistics versus good quality. For all algorithms, the curves describing the mean value in Fig. 9c start to level off at a remaining fraction of events of about 0.5, which for this high W value corresponds to the following cut-off values: $m_{ij}^2 = 2000\ \mathrm{GeV}^2$ in Jade, $d_{\mathrm{join}}^2 = 4.0$ GeV in Luclus, $E_{\perp\min} = 3.5$ GeV in Lucell, $E_{\perp}^2 = 20\ \mathrm{GeV}^2$ in K_T and $P_{\perp\min}^2 = 25\ \mathrm{GeV}^2$ in Arclus. These selected cut-off values at high W are indicated by arrows at the top of Fig. 9.

The relatively flat curves at low W (Fig. 8) makes a similar procedure for selecting cut-off values difficult and therefore prevents a direct comparison of the choices of optimal cut-off values at high and low W. Instead we use the same cut-off values as obtained in the high W case to see whether they also seem to apply to the low W region. (Note that a cut-off value at high values of W resulting in a certain fraction of remaining events will give a different fraction of remaining events at low values of W.) In Fig. 8 these cut-off values have been marked at the top and we can notice that our choices seem reasonable for all algorithms but Jade, where the remaining fraction of events is almost zero.

Even if the behaviour of the reconstruction observables at low W (Fig. 8) indicates that the cut-off values can be set quite low without a severe deterioration of the $\sqrt{\hat{s}}$ reconstruction, we will see later when we study the reconstructed number of jets as a function of the cut-off value (see Sect. 5.3), that the correct jet multiplicity for Jade at both high and low W requires a m_{ij}^2 of about $200\ \mathrm{GeV}^2$. As we can verify from Fig. 8 and Table 1 this value will also provide a reasonable reconstruc-

Table 3. The remaining fraction of events and /fwhm/rms/mean in GeV for the five jet algorithms in event samples *A*, *B*, *C*, *D*, *E* and *F*

α				
		Jade Luclus Lucell K_T Arclus	*E* 0.68 /7/5/ −3 0.58 /5/3/ −1 0.46 /4/3/ +2 0.60 /4/3/ 0 0.54 /3/2/ 0	*F* 0.49 /7/12/ −1 0.68 /6/7/ −2 0.71 /5/6/ +1 0.73 /7/6/ −1 0.70 /4/6/ −1
		C 0.55 /7/4/ −3 0.38 /4/3/ 0 0.30 /3/3/ +1 0.34 /4/3/ 0 0.48 /3/3/ 0	*D* 0.52 /8/8/ −4 0.58 /5/6/ −2 0.50 /3/6/ +1 0.50 /5/6/ −1 0.55 /4/5/ −2	
	A 0.40 /7/5/ −3 0.34 /4/3/ −1 0.25 /4/3/ +2 0.22 /4/3/ +1 0.35 /3/2/ −1	*B* 0.46 /8/7/ +5 0.45 /5/6/ −4 0.31 /4/4/ +1 0.28 /5/4/ 0 0.38 /5/6/ −4		
				Q^2

Table 2. The jet algorithm cut-off values chosen according to the method described in the text

Jade	Luclus	Lucell	K_T	Arclus
0.025	4.0	3.5	20	25
m_{ij}^2/W^2	d_{join}^2	$E_{\perp\,\text{min}}$	$E_\perp^2$	$P_{\perp\,\text{min}}^2$

tion of $\sqrt{\hat{s}}$ at low W while we recall that at high W a value of $m_{ij}^2=2000$ GeV^2 is needed for the correct reconstruction of $\sqrt{\hat{s}}$. This is a factor of ten higher than the value needed at low W, which also corresponds to the ratio of high to low W^2 (79200 GeV^2 to 7920 GeV^2). Thus, we find that the wellestablished use of W^2 as the scaling variable in Jade ($y_{\text{cut}}=m_{ij}^2/W^2$) is reasonable, at least for the reconstruction of the spectator jet, giving a value of $y_{\text{cut}}=0.025$. The final cut-off values chosen for the five algorithms are given in Table 2.

Using the cut-off values of Table 2, we obtain the reconstruction observables fwhm, rms and mean given in Table 3 for all event samples $A-F$. We conclude that event samples with equal W have a similar $\sqrt{\hat{s}}$ reconstruction but that for samples with different W values a difference is observed mainly in the rms values. This is due to the more pronounced tail in the $\sqrt{\hat{s}}-\sqrt{\hat{s}_{\text{rec}}}$ distribution at high W. The reason for this tail is not so much due to the angular distributions of the jets shown in Fig. 7a and b, but to the energy distributions of the jets closest to the spectator jet, Fig. 7c and d. At high W the most likely jet energy for the low angle jet is only a few GeV, while at low W this energy is 10–15 GeV. We know from Fig. 3 that we have similar $\hat{s}$ distributions for all values of W. Consequently, large opening angles between the two current jets, as is true for high W values, in general corresponds to small jet energies. This typically results in a reconstruction of $\sqrt{\hat{s}}$ which is better at low W than at high W.

5.3 *Reconstruction of the parton four-momenta*

We now turn to the reconstruction of individual jets within the hard subsystem. Our first requirement is that the jet multiplicity, which in our study should be 2+1 jets, is correctly reproduced. How the number of 2+1 jet events is affected by the cut-off values is shown in Fig. 10 where the fraction of 2+1 jet events is plotted against the remaining fraction of events, i.e. the purity of the 2+1 jet sample versus the efficiency of the selection. All algorithms, except Jade at high W, reach a probability of almost 100% of reconstructing the events as 2+1 jet events at the chosen cut-off values of Table 2, which is marked by arrows at the top of Fig. 10. Thus, both the spectator jet (and thereby $\sqrt{\hat{s}}$) and the jet multiplicity are correctly reproduced by all algorithms except Jade.

The Jade algorithm has a jet resolution measure based on invariant mass between particles/jet pairs that is directly influenced by the overall mass W of the had-

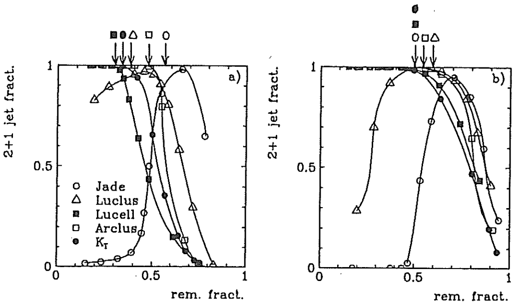

Fig. 10. The fraction of 2+1 jet events versus 'remaining fraction' in event samples **a** *C* and **b** *D*, i.e. the purity of the 2+1 jet sample versus the efficiency of the selection. The points correspond to the cut-off values specified in Table 1, increasing from right to left. The chosen cut-off values, given in Table 2, are indicated by arrows at the top of the figures

ronic system. In contrast, the other algorithms are based on various measures of transverse momenta which are not directly related with W, but rather with the scale for hard QCD emission or $\hat{s}$. The latter is essentially uncorrelated with W^2 (see Fig. 3) and one can therefore have a fixed jet resolution cut-off in those algorithms. In Jade, however, a cut-off that increases with W^2 is needed for an optimal reconstruction of the spectator jet, as demonstrated above.

If we in the case of Jade instead use a fixed cut-off at around 200 GeV^2 we are able to reproduce the jet multiplicity independent of W, whereas $\sqrt{\hat{s}}$ is well reconstructed only at low W but not at high W (see point *iv* of Fig. 9). This last problem is solved by scaling the cut-off with W^2, but then the jet multiplicity is not reproduced at high W^2. This is obvious since the resulting cut-off value $m_{ij}^2=2000$ GeV^2 is too high to resolve jets in a hard scattering subsystem with a lower invariant mass (in our case down to 225 GeV^2) and hence the two jets are merged resulting in $1+1$ jet events.

In order to improve the Jade algorithm so as to combine good reconstruction of both $\sqrt{\hat{s}}$ and the jet multiplicity independent of W we have proposed [15] a two-step procedure. In the first step we reconstruct the spectator jet using W^2 as a scale. The spectator jet is then removed and Jade is applied a second time to the remaining hard subsystem. A suitable scale in the second step is the reconstructed invariant mass squared, $\hat{s}_{\text{rec}}$. The result of the second step, with $y_{\text{cut}}=0.25$ and using $\hat{s}_{\text{rec}}$ as the scale, is that almost 100% of the events are reconstructed as $2+1$ jet events, compared to only 30%, at high values of W^2, without a second step as shown in Fig. 10b.

With the modified Jade algorithm we have five algorithms tuned to give reasonable reconstructions of $\sqrt{\hat{s}}$ and the correct jet multiplicity. The next step is a comparison of the jets and the parton four-momenta using the chosen cut-off values presented in Table 2 and applying the 15 GeV mass cut as before. In addition, we require the polar angles of the two reconstructed current jets (θ) to be between 10° and 160°. This improves the reconstruction slightly since it forces most of the jet energy flow to be inside the detector acceptance region. Each jet was assigned to the closest parton from the hard subprocess, which was defined in terms of the three-momentum difference, $|\vec{P}_{\text{jet}}-\vec{P}_{\text{parton}}|$, in order to account for both energy scale and direction. The relative error of the reconstructed parton energy as well as the absolute errors in the angle θ and the azimuthal angle ϕ were calculated. As before, the results of event samples C and D are typical for the behaviour of the algorithms for high and low W values and are shown in Fig. 11 and 12, respectively. Not surprisingly, these results indicate a behaviour of the jet algorithms which is consistent with that found in the previous chapter on reconstructing $\hat{s}$. The Jade algorithm performs less well, especially at low values of W, and the other algorithms give comparable results.

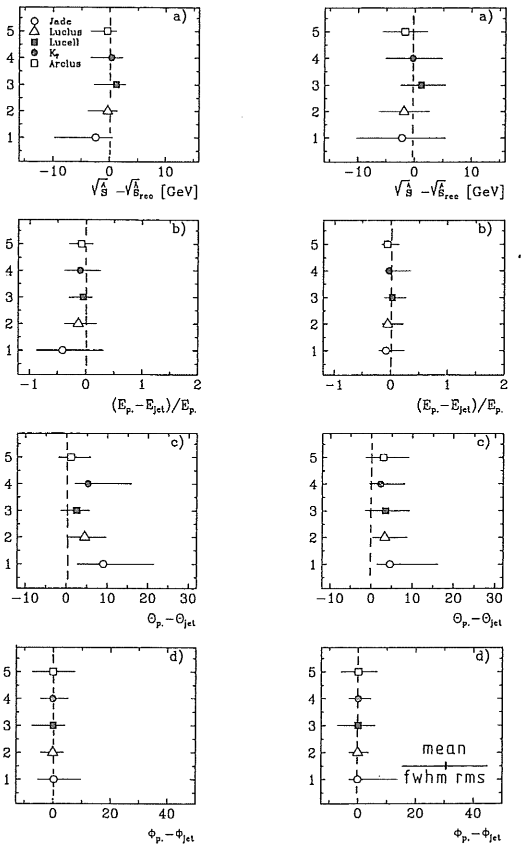

Fig. 11 and **Fig. 12.** Quality of reconstructed $\sqrt{\hat{s}}$, jet energy and angles in event samples G (**Fig. 11**) and D (**Fig. 12**) shown by the mean value (data point), full width half maximum (left error bar) and root mean square (right error bar) of the distributions for the given quantity (x axis) obtained with the indicated jet algorithms

5.4 *Effects of higher order parton emissions*

To complete this comparison of jet algorithms we investigate the effect of higher order QCD parton emissions on the reconstruction quality. These emissions are included by adding parton showers (in leading log approximation) after the matrix element treatment in Lepto 6.1 [8]. Within a given event, these additional emissions are associated with a smaller momentum transfer scale compared to the one in the matrix element. The number of emitted partons can be large, depending on the energy (or virtuality) scale of the parton initiating the shower and on the cut-off applied to stop the QCD parton branching processes, but most of them are neither energetic enough nor sufficiently separated in phase space to give rise to observable jets. The main effect is therefore a broadening of the energy flow of the jets given by the matrix element. At a suppressed rate there will, however, be hard emissions resulting in events with a jet

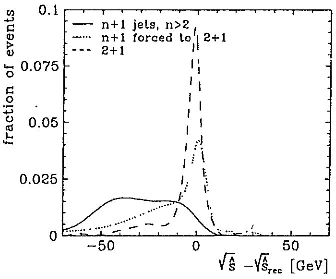

Fig.13. Quality of reconstructed $\sqrt{\hat{s}}$ using Luclus on an event sample (kinematic region *D*) with higher order QCD included through parton showers. The curves are for the specified jet multiplicities with a cut-off 4 GeV^2 and an increased cut-off to avoid multi-jet reconstruction (dotted)

multiplicity of 3+1 or more. The exact rate depends, of course, on the jet resolution.

The aim of the jet reconstruction should be related to the physics issue investigated. If the purpose is to study the first order matrix element processes, i.e. to correlate a jet with a parton of the matrix element, events with more than 2+1 reconstructed jets are problematic. To simply reject them could introduce a bias in the remaining sample and would also lower the statistics of the sample. Alternatively, one can reassign them as 2+1 jet events by merging jets, through an increased cut-off in the jet algorithm, until only the required jet multiplicity is obtained. Although this corresponds to a merging of partons, in order to recover the hardest emissions governed by the matrix element calculation, the exact kinematics of the matrix elements will not be obtained since the remaining jets are affected by higher order emissions.

These issues are illustrated in Fig. 13, showing results when Luclus has been applied to events with parton shower emissions included. The reconstruction of $\sqrt{\hat{s}}$ is poor for events with more than 2+1 jets. This is caused by extra jets from the initial state parton emission which results in a larger energy-momentum fraction being taken from the proton. Compared to the matrix element 2+1 jet case, energy will be taken from the spectator causing an increased invariant mass of the observable hard scattering system including such extra jets. The reconstruction improves considerably when these events are forced to give 2+1 jets using a higher cut-off. Naturally, the best reconstruction is still obtained from the 2+1 jet sample acquired with the original cut-off value of 4.0 GeV^2, i.e. when no jets from higher order QCD are present and can disturb the matrix element kinematics.

In the following study of the influence of higher order QCD effects we have chosen to retain the cut-off values of Table 2, i.e. values obtained from events based on matrix elements. This is appropriate given our main purpose of reconstructing jets for investigations of the QCD matrix elements. In this spirit we keep only 2+1 jet events in order to suppress distortions from higher order hard emissions giving manifest deviations from the leading order QCD matrix elements. One should realise, however, that in doing so the remaining sample may have some biases, e.g. towards smaller $\hat{s}$, which must be investigated by Monte Carlo studies before physical conclusions can be safely made. With this caveat, the results are shown in Figs. 14 and 15 and should be compared with the ones in Figs. 11 and 12 which show the results when no parton showers were included. The broadening of the jets, caused by the parton showers, increases the danger of misassigning particles. This leads to a more pronounced tail towards too large $\hat{s}_{rec}$ as well as a shift in the reconstructed parton energy and polar angle and increased rms spread. The larger effect observed at higher *W* values is most likely dominated by an increased smearing due to the enhanced initial state radiation at the higher Q^2 values associated with larger *W*.

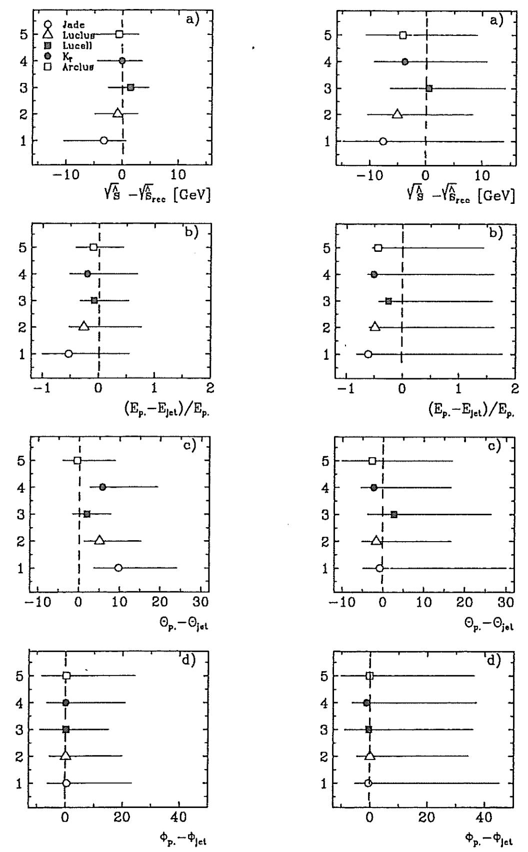

Fig. 14 and **Fig. 15**. Quality of reconstructed $\sqrt{\hat{s}}$, jet energy and angles in event samples *C* (**Fig. 14**) and *D* (**Fig. 15**) as in Figs. 11 and 12 but with higher order QCD parton emission included through parton showers

In the reconstruction of the first order matrix element subsystem and its jets, we have so far only considered events with an invariant mass of the resulting parton pairs $m_{ij} > 10$ GeV. Below this cut-off the matrix elements increase without bound for $m_{ij} \rightarrow 0$ corresponding

Table 4. Reduction of event statistics due to the cuts applied to the three event types (described in the text) to obtain a clean 2+1 jet sample

Event sample:	C			D		
Event type:	q	qg	$q\bar{q}$	q	qg	$q\bar{q}$
Initial sample	39608	5336	9414	32094	9032	7556
$\sqrt{\hat{s}} > 15$ GeV	892	1890	4396	4492	5590	6421
$n_{\text{jet}} = 2+1$	787	1600	3787	3772	3518	3144
$10° < \theta_{\text{jet}} < 160°$	181	921	2000	1602	2154	2000
$\lvert\eta_{\text{jet}\,1} - \eta_{\text{jet}\,2}\rvert < 2$	181	920	1997	274	1673	1233

to the usual soft and collinear divergences for bremsstrahlung processes of massless quanta. The Sudakov form factor suppression built into the parton shower makes it more suitable to simulate emissions in this region. The class of events with no hard emission from the matrix element treatment, called q events [8], but with possible softer radiation from parton showers must also be considered. In general, these events will be reconstructed as 1+1 jets and give a small $\sqrt{\hat{s}}$. However, for large fluctuations and given the huge 1+1 jet cross section compared to the genuine 2+1 jet cross section one cannot neglect them a priori. Table 4 shows the results of a generation of about 50000 events. The QCD-Compton and the boson-gluon fusion events, denoted qg and $q\bar{q}$ respectively, are generated with QCD matrix elements for $m_{ij} > 10$ GeV, whereas below that limit zeroth order events, denoted q events, are generated. Parton showers are added to all types of events. As can be seen, q events dominate the inclusive sample, but the fraction of events surviving the criteria for 2+1 jet events is very small. The criteria are *(i)* a reconstructed subsystem mass of at least 15 GeV, *(ii)* a reconstruction of exactly 2+1 jets and *(iii)* the polar angles of the two current jets in the region $10° \leqq \theta \leqq 160°$. In event sample C the amount of surviving q events can be neglected, but in event sample D the amount is comparable to the real 2+1 jet events.

The difference in the rate of fake 2+1 jets in sample C and D is due to their different jet topologies. The current quark direction is, in QPM kinematics, in the backward direction for the large W in sample D, see (3) and Fig. 2a, whereas it is in the forward direction for the lower W in sample C. The additional jets in q events from parton showers mainly come from the initial state radiation along the incoming parton, i.e. they emerge along the proton in the forward direction. Such emissions, which are more abundant at large W, will therefore be better separated from the current jet in sample D and have a greater chance of being reconstructed as a jet. This fake jet will thus have a large opening angle with respect to the scattered quark and consequently the invariant mass of this pair will be large and might survive the mass cut of 15 GeV. However, the pseudorapidity distributions of the three event classes turn out to have different shapes such that a cut in the difference between the jet pseudorapidities, $\lvert\eta_{\text{jet}\,1} - \eta_{\text{jet}\,2}\rvert < 2$, would greatly improve the ratio of qg and $q\bar{q}$ events to q events in sample D and would not be harmful in kinematic regions (like C) where such an improvement is not necessary. Figure 16 demonstrates this for events which passed the 2+1 jet criteria of Table 4.

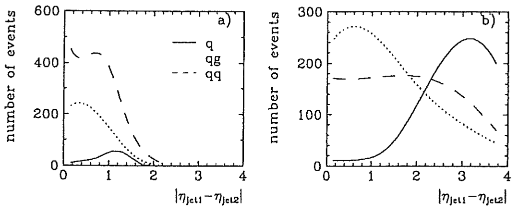

Fig. 16. Difference in pseudorapidity between the two jets reconstructed in q, qg and $q\bar{q}$ events for event samples **a** C and **b** D

6 Conclusions

The ability to reconstruct the jet structures of the order α_s processes in HERA events has been investigated by comparing three commonly used and two new algorithms. In particular, an attempt was made to optimize the jet reconstruction to reproduce the properties of partons generated according to the first order α_s matrix elements. This was achieved by using a Monte Carlo simulation based solely on matrix elements for which the multiplicities and properties of the partons are well defined. In addition we required the invariant mass of any two partons to be larger than 10 GeV to ensure reasonably clear jet structures. After optimization of the algorithms the influence due to parton showers was studied.

The reconstruction of jets at HERA contains the well-known problem of separating the spectator jet from the jets of the hard subsystem in the event. In order to perform a systematic study of this problem we have investigated how the reconstructed invariant mass of the hard subsystem, $\sqrt{\hat{s}}$, depends on the resolution parameter of the algorithm. To avoid events where the hard subsystem is partly merged with the spectator jet we have found that a cut on the reconstructed invariant mass of the hard subsystem of 15 GeV is efficient. The fraction of events which is removed by this cut depends on the cut-off value of the resolution parameter in the algorithm. Since both the quality of the $\sqrt{\hat{s}}$ reconstruction and the number of events surviving the mass cut are dependent on the resolution parameter their variation with the cut-off value can be used to compare different jet algorithms and to obtain an indication of an appropriate choice of cut-off value for a specific algorithm.

In contrast to what might be intuitively expected, we find that jets are in general better reconstructed at low than at high invariant masses of the hadronic final state (W). This can be understood from the fact that the $\sqrt{\hat{s}}$ distributions at high and low W are similar but the event topologies are not. At high W the opening angle between the jets is in general larger than at low W. Consequently the jet energies must be smaller at high W compared to low W in order to obtain similar $\sqrt{\hat{s}}$ values. The low energy of the jet closest to the spectator jet at high W makes a correct reconstruction difficult.

One of the investigated algorithms (Jade) performed consistently worse than the other four (Luclus, Lucell, Arclus and K_T). In order to find one single cut-off value which gives reasonable reconstruction of $\sqrt{\hat{s}}$ at various W, the invariant mass m_{ij}, used as a distance parameter in Jade, has to be scaled with W^2. For high W this implies that the invariant mass will take values which are much larger than the typical invariant mass of the hard subsystem and thus the algorithm, although it works well in separating the hard subsystem from the spectator jet with this scaling variable, will not resolve the individual jets of the hard subsystem. We therefore propose to use Jade in two steps where the scale in the second step should be the reconstructed $\hat{s}$. In spite of this improvement the Jade algorithm reconstructs the parton four-momenta less well than the other four algorithms which give similar results.

The effect of higher order parton emissions was studied by adding parton showers to the partons generated by first order matrix elements. As expected, the inclusion of parton showers deteriorates the quality of the reconstruction somewhat but it does not change our overall conclusions from the matrix element study. Finally, we note that the background from QPM-type events, where initial state radiation fakes an additional jet, can not be neglected, especially not at high W. In this case we have found that a cut in the measured pseudorapidity difference between the two reconstructed jets greatly improves the signal-to-background ratio.

Acknowledgements. We would like to thank M. Nyberg for many valuable discussions. R. Nisius, L. Lönnblad, M. Seymour, G. Grindhammer and Yu. Dokshitzer are acknowledged for useful comments to various parts of the content. The Lund group would like to thank the DESY directorate for its kind hospitality.

References

1. G. Hansson et al.: Phys. Rev. Lett. 35 (1975) 1609; Ch. Berger et al., PLUTO Coll.: Phys. Lett. B78 (1978); 176; R. Brandelid et al., TASSO Coll.: Phys. Lett. B83 (1979) 261
2. For previous studies of jet reconstruction at *ep* colliders, see e.g.: P. Burrows, G. Ingelman, E. Ros: Z. Phys. C39 (1988) 257; M. Fleischer et al.: in [19] vol. 1, p. 303
3. W. Bartel et al., JADE Coll.: Z. Phys. C33 (1986) 23; S. Bethke et al., JADE Coll.: Phys. Lett. B213 (1988) 235
4. T. Sjöstrand: Comput. Phys. Commun. 28 (1983) 227
5. T. Sjöstrand: Comput. Phys. Commun. 39 (1986) 347; ibid. 43 (1987) 367
6. L. Lönnblad: Z. Phys. C58 (1993) 471
7. S. Catani, Yu.L. Dokshitzer, B.R. Webber: Phys. Lett. 285B (1992) 291
8. G. Ingelman: LEPTO version 6.1, in [19] vol. 3, p. 1366
9. M. Arneodo et al., EMC Coll.: Z. Phys. C36 (1987) 527; Phys. Lett. 150B (1985) 458; G.T. Jones et al., WA21 Coll.: Z. Phys. C25 (1985) 121; ibid. C27 (1985) 43; D. Allasia et al., WA25 Coll.: Z. Phys. C24 (1984) 119
10. T. Ahmed et al., H1 Coll.: Phys. Lett. B298 (1993) 469; I. Abt et al., H1 Coll.: DESY 93-137; M. Derrick et al., ZEUS Coll.: Z. Phys. C59 (1993) 231; M. Derrick et al., ZEUS Coll.: Phys. Lett. B306 (1993) 158
11. S. Bethke: in: Proc. 'QCD – 20 years later', Aachen 1992, p. 43; Singapore: World Scientific 1993; S. Bethke: J. Phys. G17 (1991) 1455
12. S. Bethke, Z. Kunszt, D.E. Soper, W.J. Stirling: Nucl. Phys. B370 (1992) 310
13. G. Arnison, et al., UA1 Coll.: Phys. Lett. B123 (1983) 115; ibid. B132 (1983) 223
14. B. Andersson, G. Gustafson, L. Lönnblad, U. Pettersson: Z. Phys. C43 (1989) 621
15. V. Hedberg, G. Ingelman, C. Jacobsson, L. Jönsson: in: [19] vol. 1, p. 331
16. S. Catani et al.: Phys. Lett. B269 (1991) 432
17. B.R. Webber: J. Phys. G19 (1993) 1567
18. D. Graudenz, N. Magnussen: in: [19] vol. 1, p. 261
19. Proceedings 'Physics at HERA', W. Buchmüller, G. Ingelman (eds.), DESY Hamburg 1992, vol. 1–3

Appendix C

Jet Identification based on Probability Calculations using Bayes' Theorem

DESY 94–217

November 1994

Jet Identification based on Probability Calculations using Bayes' Theorem

C. Jacobsson[a], L. Jönsson[a], G. Lindgren[b], M. Nyberg-Werther[a]

[a] Physics Department, Lund University, Sölvegatan 14, S-223 62 Lund, Sweden
[b] Department of Mathematical Statistics, Lund University, Box 118, 221 00 Lund, Sweden

Abstract

The problem of identifying jets at LEP and HERA has been studied. Identification using jet energies and fragmentation properties was treated separately in order to investigate the degree of quark-gluon separation that can be achieved by either of these approaches. In the case of the fragmentation-based identification, a neural network was used, and a test of the dependence on the jet production process and the fragmentation model was done. Instead of working with the separation variables directly, these have been used to calculate probabilities of having a specific type of jet, according to Bayes' theorem. This offers a direct interpretation of the performance of the jet identification and provides a simple means of combining the results of the energy- and fragmentation-based identifications.

ISSN 0418-9833

1 Introduction

In many tests of QCD, based on processes producing jets, it is of great importance to be able to identify whether a jet originates from a quark or a gluon. Different criteria such as specific decay properties, prior knowledge of the short range dynamics of the process or differences in the topology of jets due to hadronisation can be used in such an identification.

Especially heavy quarks can be identified from their decay properties by using apropriate particles in the decay chain to tag the flavour of the heavy quark. Fast leptons from semileptonic decays have been used, as well as charged kaons and D-mesons. Further, the long decay time of weak decays offers the possibility of reconstructing the secondary decay vertex by using high resolution vertex detectors.

The short range dynamics defines the kinematic properties of the process. For example, the fact that gluons are produced from primary quarks in a bremsstrahlung-like process implies that the gluon jets are usually less energetic than the quark jets in an event.

The topology of jets is due to features of the partons which are related to their intrinsic properties, such as mass and colour charge. Such differences influence the way the partons fragment into final state hadrons forming jets.

In this analysis we have studied jet separation from a general aspect and therefore have concentrated on differences in the jet energies and in those properties of jets that are related to the fragmentation process. The optimal cut in jet energy for a separation between quarks and gluons obviously depends on how much energy is available for a certain process and how many jets are produced in that process. In e^+e^- collisions the energy available for jet production is well defined, while for *ep* collisions the energy involved in the hard scattering subprocess varies from event to event. For the description of the shape of jets a large number of fragmentation variables are available. In principle the fragmentation of a parton should not depend on the way it has been produced, i.e. if the underlying process is an e^+e^- or an *ep* collision, especially if we restrict ourselves to consider the jet core which makes a possible influence of the colour strings less important. We have thus made an attempt to find a process-independent method to identify quarks and gluons by using suitable fragmentation variables alone.

The neural network method has previously been used with various input variables for the purpose of separating gluon jets from quark jets [1]. For various reasons which will be explained in the following, we have in this analysis distinguished between identification based on jet energies and identification based on fragmentation properties, using a neural network in the latter case. In a final step the two methods have been combined in order to improve the result by using all the available information. This can easily be done if, instead of working with the various separation variables directly, one converts these into probabilities that a jet is a quark or a gluon jet and applies cuts in the combined probabilities.

Most previous attempts to perform jet identification have been based on studies of individual jets. The approach which we have adopted is to isolate the specific event type of interest and use the additional information contained in the knowledge of the exact number of quarks (q), antiquarks ($\bar{q}$) and gluons (g) for that event. Experimentally this method is possible for 3-jet events in e^+e^- collisions which must be of the type $q\bar{q}g$, whereas it is a good approximation to assume that 4-jet events consist of a $q\bar{q}gg$ configuration, since the $q\bar{q}q\bar{q}$ contribution is strongly suppressed. In the case of ep collisions (2+1) jet events denote events with two jets in the hard scattering system in addition to the jet from the spectator quarks. The spectator jet, which is easily identified, is of no direct interest in the study of the hard subsystem which is the motivation for treating such events as 2-jet events in the following. The final state of these events is either of qg type (the QCD-Compton process) or $q\bar{q}$ type (the Boson-Gluon fusion process), although in certain kinematic regions the $q\bar{q}$ events can be neglected and we are left with a clean sample of qg events. For higher jet multiplicities the situation becomes less clear and an event-based identification can not be easily applied. In this study we have thus concentrated on 3-jet events generated at the LEP centre-of-mass energy, 91.2 GeV, and (2+1) jet events of the qg-type from simulated collisions between 820 GeV protons and 26.7 GeV electrons at HERA. The Feynman diagrams for the processes investigated here are shown in Fig. 1.

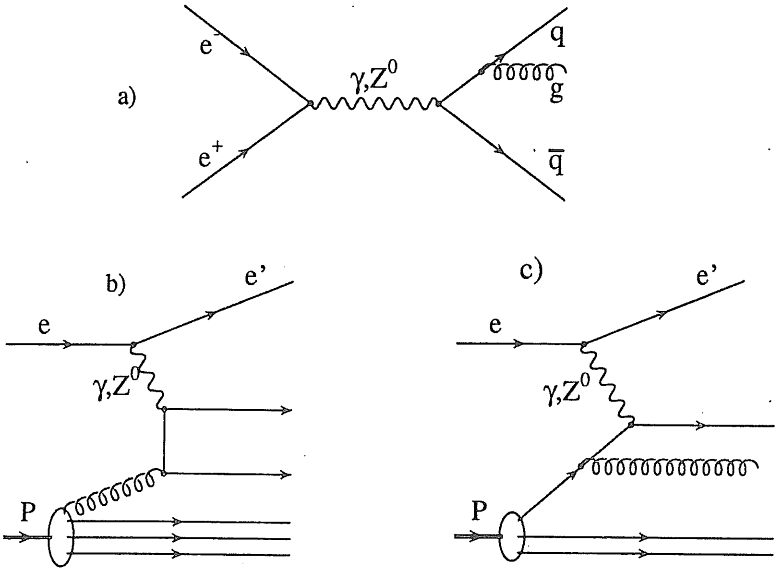

Figure 1: *The Feynman diagrams for a) a 3-jet event from an* e^+e^- *collision, b) a BGF event from an ep collision and c) a QCD-Compton event from an ep collision.*

2 Event generation

In order to investigate whether our jet identification based on fragmentation properties is process-independent, we have applied our method to both Monte Carlo-generated e^+e^- events and ep events. The generation of ep events has been done with the Monte Carlo (MC) programs LEPTO and HERWIG, which are known to reproduce Deep Inelastic Scattering (DIS) data from previous fixed target lepton-nucleon scattering experiments and also to give a fair description of the limited data on jet physics currently available at HERA. The Monte Carlo program JETSET has proven to give a good description of various e^+e^- data and was thus used to produce such events.

The basic concept of the event generators is that hard scattering processes can be factorized into an elementary hard process, initial- and final state radiation, and a hadronisation process. This general scheme can be used to describe a large variety of QCD and electroweak processes by applying different elementary subprocess matrix elements.

The JETSET program [2] describes e^+e^- annihilation into hadronic final states, using two alternative approaches. One is the calculation of explicit matrix elements (ME) up to the second order in α_s and the other is based on parton shower (PS) emission, which allows the production of an arbitrary number of jets. Although both methods have their advantages and disadvantages we have, in this analysis, chosen the parton shower option based on the coherent evolution scheme by Marchesini and Webber. A parton shower is based on the branchings $q \rightarrow qg, g \rightarrow gg$ and $g \rightarrow q\bar{q}$ as given by Altarelli-Parisi evolution equations in the leading logarithm approximation of perturbative QCD. The evolution is performed in an iterative manner and stopped when all parton masses have evolved below some minimum mass. This leads to an ordering in angle in the sense that angles between two emitted partons decrease with consecutive branching. The hadronisation is performed according to the Lund string model [3] [2].

LEPTO [4] simulates the basic DIS neutral and charged current processes and we have chosen to consider only the dominant neutral current process where a reconstruction of the event kinematics from the scattered electron can be made. In addition to the leading order Quark Parton Model (QPM) process, $\gamma^* q \rightarrow q$, where no jet identification is needed and therefore is of no interest for this analysis, also first order (α_s) processes, i.e. the QCD-Compton process, $\gamma^* q \rightarrow qg$, and the boson-gluon fusion process, $\gamma^* g \rightarrow q\bar{q}$, are calculated from QCD matrix elements. In order to avoid divergences from soft and collinear parton emission, a cut-off in the invariant mass of any two partons, m_{ij}, is implemented. Higher order corrections are then included by adding parton showers according to the same scheme, based on the Altarelli-Parisi evolution equation, as in JETSET. The amount of initial- and final-state radiation is determined by the virtual mass of the initiating parton just before and after the boson vertex. The initial-state radiation is generated by a backward evolution scheme from the hard vertex which is controlled by the parton density function specified in the program. We have used the MRS H parametrisation of the density function, as it describes recent results on the proton structure function F_2 at low Bjorken-x values from HERA. As in the case of the e^+e^- events, the Lund string fragmentation is used to produce the hadronic final state.

Similar to the LEPTO program, the simulation of (2+1) jet ep events by the HERWIG generator [5] is done using matrix elements to describe the first order processes in the strong coupling constant, and higher order emissions are introduced by parton showers which are generated essentially with Q^2 as mass scale. The upper limit for the shower evolution variables are related to energies and angles rather than to parton virtualities. The backward evolution process produces coherent, initial-state parton showers with full QCD cascading of all emitted partons. The same parton density function was used as for LEPTO. The final-state coherent showers include soft gluon interference and azimuthal correlations due to the gluon spin. The emitted gluons are split into quark antiquark pairs (or possibly into diquark antidiquark pairs) between which there are colour lines forming colour-singlet clusters. The clusters created in this way are fragmented into hadrons through a longitudinal splitting of the high mass clusters and phase space decay of lower mass clusters. This fragmentation scheme is normally denoted cluster fragmentation.

As already mentioned, this study has been limited to simulated 3-jet events from e^+e^--interactions at LEP and (2+1) jet events from generated *ep* collisions at HERA. No detector simulation has been done but, for the analysis of HERA events, the usual beam pipe cut was introduced, excluding the regions in polar angle below 4^o and above 176^o not covered by the detector. Due to the event topologies of deep inelastic scattering processes most of the spectator jet will disappear undetected down the forward cone, while for the majority of events the scattered electron will proceed inside the backward cone. No such cut is necessary at LEP since no specific activity is expected in these regions and since the jet analysis is in any case limited to the barrel region of the detector.

Since the Monte Carlo generators we have used cover jet production in e^+e^- as well as *ep* collisions and, in addition, use two different fragmentation schemes, we are able to test both the process- and model-dependence. This is done by training the neural network on samples from either of the generators and comparing the results when the network is applied to a test sample from the same generator and from one of the other generators, respectively, according to the following procedure. A comparison of the results from the network when trained on event samples from HERWIG and LEPTO respectively and subsequently tested on an event sample generated by LEPTO, will provide the model-dependence. On the other hand, if the respective event samples from JETSET and from LEPTO are used to train the network, which is then tested on a sample from JETSET, the process-dependence will come out. Finally, if the network trained on the samples from HERWIG and from JETSET respectively is applied on the test sample from JETSET, we obtain both the model- and the process-dependence.

3 Jet reconstruction

In order to reconstruct particle jets, the LUCLUS algorithm [6], based on the combination of energy clusters, was used. A careful study of the reconstruction quality as a function of the resolution parameter in the algorithm showed that a value $d_{join} = 4$ GeV was relevant (see [7]). In the HERA analysis the clustering was done in the so-called hadronic center-of-mass system i.e. in the center-of-mass system of the incoming proton and the exchanged virtual photon. In order to reconstruct the spectator jet in the best possible way, a pseudoparticle is added to each event to represent the fraction of the proton fragment lost in the beam pipe. The momentum of this pseudoparticle is given by the difference between the longitudinal momentum of the initial state and the measured longitudinal momentum of the final state, as described in [8].

In a Monte Carlo generator which includes parton showers, many partons can contribute to a jet and one needs a method to establish whether the reconstructed jet should be regarded as originating from a quark or from a gluon. For *ep* events, where the ME forms the basis of the processes and PS are added to simulate higher order corrections, we simply checked which reconstructed jet was closest to the original parton from the ME, according to: $\min(|\bar{P}_{jet1} - \bar{P}_q| + |\bar{P}_{jet2} - \bar{P}_g|, |\bar{P}_{jet2} - \bar{P}_q| + |\bar{P}_{jet1} - \bar{P}_g|)$. Since the e^+e^- events are not generated with ME, we have to extract the momentum vectors of the jets for both the parton level and the hadron level by applying the LUCLUS jet algorithm. A comparison of the momentum vectors in pairs on the parton and hadron level, identified which jet on the hadron level corresponds to a certain jet on the parton level. If the jet on the parton level contains an odd number of quarks, it is considered to be a quark-initiated jet, while if the number of quarks in the jet is even, it is defined as a gluon jet. For almost all three jet events, the result of this definition is exactly one gluon and two quark jets. If not, the event is discarded.

4 Event selection

4.1 Selection of HERA events

Since we want to concentrate on the (2+1) jet events we have considered only those events in which the jet algorithm found exactly two jets + the spectator jet. In the hadronic centre-of-mass system we required the minimum energy of each jet to be 5 *GeV* and the invariant mass of the two jets to be larger than 15 *GeV* to ensure that the selected events had a reasonably clear jet structure. We also required a minimum of four particles to be assigned to each jet, since the jet variables which were used to study the fragmentation, are not meaningful for jets with too few particles. In order for the two hard jets to be well inside the acceptance region of the HERA experiments and to have a separation in space from the proton remnant, both jets had to be reconstructed within the region of polar angles $10^\circ < \theta < 160^\circ$ as measured in the laboratory system. The two jets also had to be separated by less than two units of pseudorapidity. It has been previously shown [7] that this is necessary in order to cut down the background of q-type events which otherwise enter the (2+1) jet sample.

Finally, we use only events produced within certain limits of the kinematic variables generally used to describe DIS events. These are Q^2, the momentum transfer squared, the Bjorken-x and -y scaling variables and W^2, the invariant mass squared of the hadronic system:

$$Q^2 \equiv -q^2 = -(p_e - p_l)^2, \quad x \equiv \frac{Q^2}{2P \cdot q}, \quad y \equiv \frac{P \cdot q}{P \cdot p_e}, \quad W^2 \equiv (q+P)^2 = Q^2 \frac{1-x}{x} + m_p^2$$

(For a description of these variables and how they can be measured at HERA, see, for example, [9]).

The cross-section falls rapidly with increasing x and Q^2, for both the qg - and the $q\bar{q}$ type of events, but qg events dominate in the region of high-x-values. At $x \geq 0.1$ an almost pure sample of qg events is produced, $\frac{qg}{q\bar{q}} > 8$, and one can thus concentrate on separating quark jets from gluon jets in this region. A sample of qg events from this region was therefore used in our attempts to identify gluon jets at HERA. At lower values of x ($x < 0.1$) a mixture of qg - and $q\bar{q}$ events is produced and therefore the problem of separating the two event types has to be dealt with.

4.2 Selection of LEP events

In the selection of Monte Carlo-generated 3-jet events from e^+e^- collisions at LEP, we required each jet to have an energy of more than 5 GeV in order to have reasonably collimated flows of particles. Exactly as for the jets from *ep* collisions, the invariant mass of any jet pair, m_{ij}, should exceed 15 GeV to give an observable 3-jet topology. Also in analogy with the treatment of *ep* collision events we required each jet in an e^+e^- event to contain at least 4 particles, since the same fragmentation variables are going to be used in both cases. The energy sum of all three jets in an event was required to be greater than or equal to 90 GeV in order to guarantee that no fraction of a jet had escaped detection. We have assumed a LEP detector with full azimuthal coverage but restricted the jets to fall inside the range $40^o < \theta < 140^o$ of polar angle. This is the barrel region which is normally well covered by both the tracking system and the calorimetry of a detector.

5 Identification of gluon jets using jet-energy

Based on the assumption that gluon jets carry less energy than quark jets and using the known number of quarks and gluons in the event type under investigation, we want to calculate the probability that a jet originate from a gluon. In doing this we recall that there is a difference between e^+e^- collisions and *ep* collisions in the sense that the energy sum of quarks and gluons is constant and equal to $\sqrt{s}$ for e^+e^- processes, while the energy entering the hard scattering subprocess in *ep* collisions varies from event to event. An identification which includes jet energies will therefore always be process-dependent.

The probability of emitting a gluon with a certain energy in an e^+e^- collision is obtained directly from first order ME calculations. The conditional probability of jet1 in a 3-jet event to originate from a gluon, provided the jets have the energies E_1, E_2 and E_3, is given by:

$$P^{E_{123}}_{gqq}(jet1, jet2, jet3|E_1, E_2, E_3) = \frac{E_2^2 + E_3^2}{(E_{cm} - 2E_2)(E_{cm} - 2E_3)} \cdot \qquad (1)$$

$$\left(\frac{E_1^2 + E_2^2}{(E_{cm} - 2E_1)(E_{cm} - 2E_2)} + \frac{E_2^2 + E_3^2}{(E_{cm} - 2E_2)(E_{cm} - 2E_3)} + \frac{E_3^2 + E_1^2}{(E_{cm} - 2E_3)(E_{cm} - 2E_1)}\right)^{-1}$$

where E_{cm} is the centre-of-mass energy of the e^+e^- collision.

The probability that the scattered quark radiates a gluon of a certain energy in an *ep*-interaction is not so easily accessible from the matrix element and we have therefore used Monte Carlo-generated energy distributions to extract the density functions for the gluon and the quark, f_g and f_q, in a qg event.

$$f_g^E = \frac{f_{gq}^E(E_g, E_q)}{f_{g+q}^E(E_g + E_q)}$$

$$f_q^E = \frac{f_{gq}^E(E_q, E_g)}{f_{g+q}^E(E_g + E_q)}$$

where f_{gq}^E is the joint density function, given that the gluon and the quark have the energies E_g and E_q, respectively. The total energy of the quark gluon system, $E = E_g + E_q$, is a random variable with the density $f_{g+q}^E(E_g + E_q)$. Since we know that the *a priori* probability for selecting a quark or a gluon is equal, then the probability for jet1 to be a gluon jet is given by Bayes' theorem (see Appendix A):

$$P_{gq}^{E_{12}}(jet1, jet2|E_1, E_2) = \frac{0.5 f_g^E}{0.5 f_g^E + 0.5 f_q^E} = \frac{f_{gq}^E(E_1, E_2)}{f_{gq}^E(E_1, E_2) + f_{gq}^E(E_2, E_1)} \qquad (2)$$

where E_1 and E_2 give the energies of jet1 and 2, respectively.

In each event the jet with the highest probability, $P_{g,max}$, is selected to originate from a gluon. The allowed range of gluon probabilities is, for 2-jet events $\frac{1}{2} < P_{g,max} < 1$, and for 3-jet events $\frac{1}{3} < P_{g,max} < 1$, where the lower bounds correspond to equal probabilities for all jets in the event to be a gluon. A general definition of the allowed range would thus be $\frac{1}{\#jets} < P_{g,max} < 1$, giving the limits within which a cut (P_{cut}) can be specified in order to enhance the purity of gluon jets in our selected sample. (For processes containing more than one gluon, the procedure can in principle be repeated to find a second gluon in the remaining sample and so on. The probability bounds for the second gluon will then be $\frac{1}{\#jets-1} < P_{g,max} < 1$ and for the i:th gluon candidate $\frac{1}{\#jets+1-i} < P_{g,max} < 1$.) From the generated MC data we can now check whether the jet with the value $P_{g,max}$ and thereby identified as a gluon jet, was actually initiated by a gluon or by a quark. As an example, if we plot, for 3-jet events from e^+e^- collisions, the frequency of the jet to originate from a quark and a gluon, respectively, as a function of $P_{g,max}$, we get the distributions shown in Fig. 2. The figure should be interpreted in the following way. If, in an event, the jet with the highest probability of being a gluon jet has the probability value $P_{g,max}$, then the probability of it to really originate from a gluon is given by the value of the gluon distribution (y_g) at $P_{g,max}$, divided by the summed values of the gluon and quark distributions ($y_g + y_q$) also at $P_{g,max}$. It is then clear that, for a certain P_{cut}, the efficiency and purity for identifying the gluon jet, and thereby also the quark jet(s), in events containing only one gluon, can be expressed as

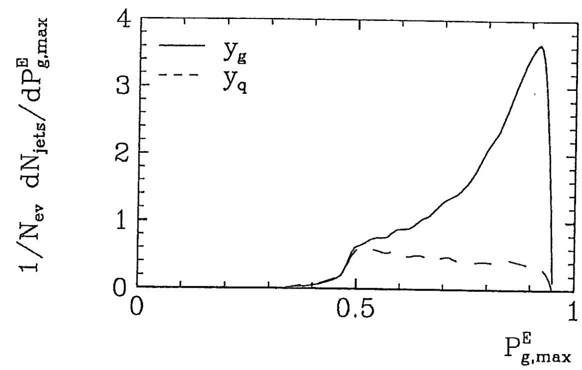

Figure 2: *The $P^E_{g,max}$ distributions for quarks and gluons in a 3-jet event.*

$$Efficiency = \frac{\int_{P_{cut}}^{1} (y_g + y_q)\, dP_{g,max}}{\int_{\frac{1}{\#jets}}^{1} (y_g + y_q)\, dP_{g,max}} \qquad (3)$$

$$Purity = \frac{\int_{P_{cut}}^{1} y_g\, dP_{g,max}}{\int_{P_{cut}}^{1} (y_g + y_q)\, dP_{g,max}} \qquad (4)$$

where $P_{cut} \geq \frac{1}{\#jets}$.

6 Identification of gluon jets using fragmentation properties

Due to the fact that gluons, according to QCD, carry a stronger colour charge than quarks, it is expected that there will be differences in their fragmentation. A large number of variables sensitive to these differences have been suggested for the purpose of performing quark-gluon separation. Above we have derived the probability formalism for a separation using the jet energies alone and here we will go through the same procedure for an identification by fragmentation variables, using a neural network.

Variables describing fragmentation properties are normally based on the relation between single particles in a jet and the jet axis. A jet algorithm therefore has to be applied before the fragmentation-sensitive variables can be calculated. To avoid a dependence of the fragmentation variables on the detailed reconstruction of a jet by different jet algorithms, we consider only particles in the jet core. The jet core is defined by taking the particles of a jet in descending order of P_l, the longitudinal momentum with respect to the jet axis, until we reach 80% of the total jet energy. Since the jet algorithm is not Lorentz-invariant, using only the jet core also leads to an insensitivity of the frame in which the clustering takes place, which is very important for the HERA events. We also want the fragmentation variables to be experimentally useful, i.e. they should not be greatly affected by detector smearing and poor event reconstruction.

One set of variables we have tested and found to provide the best separation between quarks and gluons is the so called **Fodor moments** [11]:

$$F_{nm}(E_{jet}) = \sum \left(\frac{P_T}{E_{jet}}\right)^n \eta^m$$

where P_T and η are the transverse momentum and the pseudorapidity of a particle in a jet with respect to the jet-axis and E_{jet} is the jet energy. The sum is taken over all particles in the jet core. The three lowest moments have an obvious interpretation. F_{00} is the multiplicity of the jet, F_{01} is the pseudorapidity sum of all particles in the jet, and F_{10} is the transverse momentum sum of all particles, scaled by the jet energy. A careful study of the Fodor moments reveals that the results based on the different generators give general agreement only for some of the moments. This is, however, a necessary condition for obtaining an independence of both the jet production process and the fragmentation model used, and consequently we have concentrated on these moments. The mean values of the moments F_{11}, F_{15}, F_{20} and F_{31} exhibit similar behaviour as a function of energy for all the generators except in the low energy range of the moment F_{15} where the JETSET curves fall below the others. This is illustrated in Fig. 3a-d. A separation cut between quarks and gluons common for all the generators can thus, in principle, be found for the moments F_{11}, F_{20} and F_{31} over the full energy range, whereas this is not true for the moment F_{15}. However, as can be observed in Fig. 3f, the Fodor moment distributions for quarks and gluons overlap significantly which in any case prevents a completely clean separation. As an example of a moment where the curves from the various generators are widely spread and therefore make the choice of a common separation cut difficult, we show the moment F_{00} in Fig. 3e. In our selection we have avoided the higher Fodor moments since they will, from an experimental point-of-view, be very sensitive to the reconstruction quality of the energy and direction of the particles.

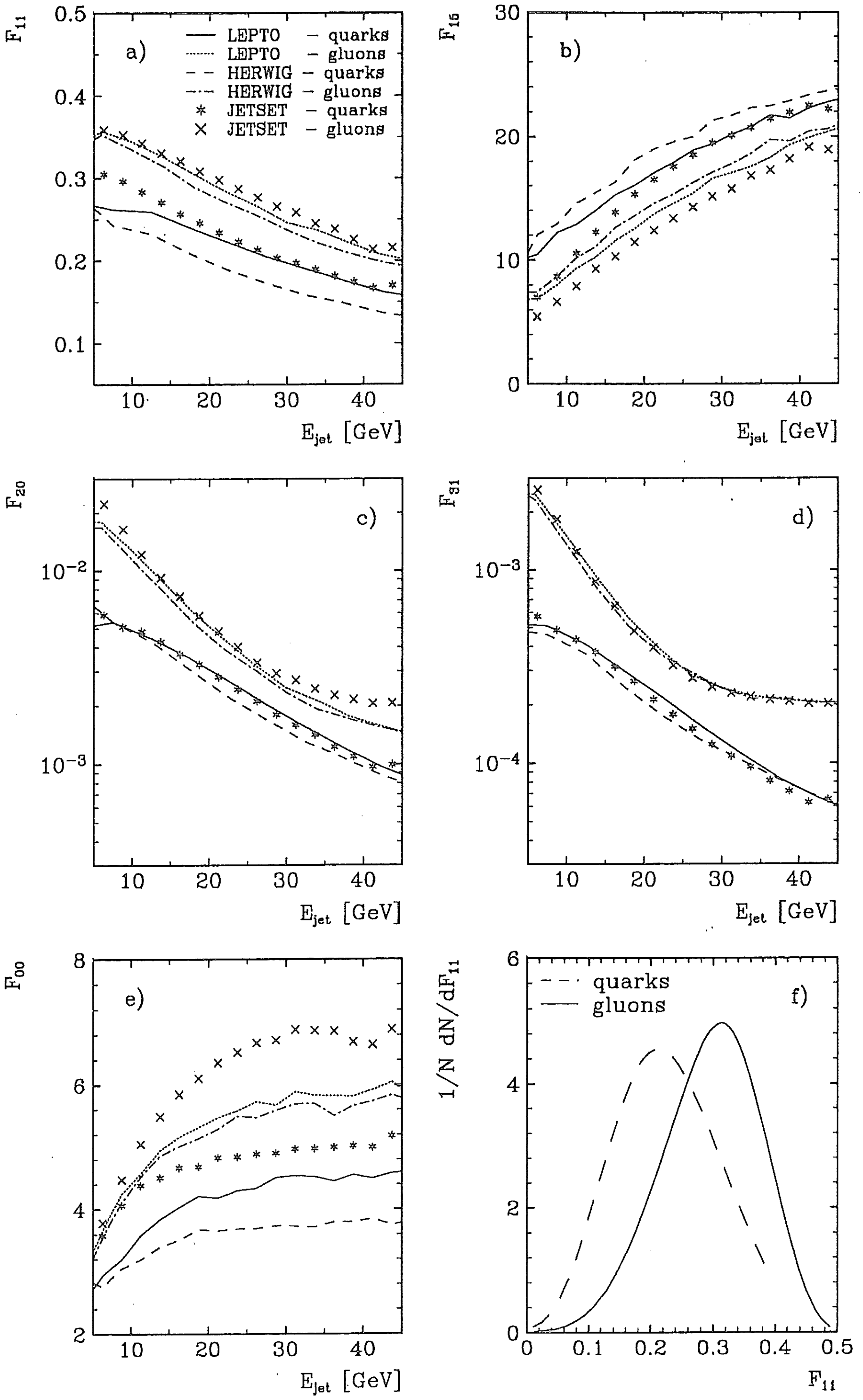

Figure 3: *The Fodor moments a)* F_{11}*, b)* F_{15}*, c)* F_{20}*, d)* F_{31} *and e)* F_{00} *as a function of the jet energy. In f) the* F_{11}*-distributions for quarks and gluons in LEPTO at* $E_{jet} \approx 25$ *GeV are shown.*

One of the reasons for using a neural network in the jet identification based on fragmentation properties is that we want to simultaneously take into account the effect of several variables and their correlations. We have chosen a network, as implemented in the program package JETNET 2.0 [10], using the method of backpropagation, well suited for this kind of pattern recognition. We have varied the number of hidden layers, nodes and values of the learning rate, but this did not produce a significant change in the final results. We therefore decided to use one hidden layer and one output node ($0 = quark; 1 = gluon$)

To enable a process-independent identification it is essential that the result does not depend on the jet energy, and one can therefore either try to select variables which are completely uncorrelated with the jet energy or train the neural network in such a way that the jet energy by itself does not give any discrimination. In the latter case it is important, from the point-of-view of the neural network, to be careful in the use of energy-dependent fragmentation variables. Although we want the network to be sensitive to the energy dependence of the fragmentation variables, it should not be affected by the jet energies themselves. Since the difference in the jet energy distributions is the most dominant effect, it might be picked up even implicitly by the neural network. Therefore a good training strategy will help to emphasize the learning of the network on the more subtle fragmentation properties.

Among the variables we have investigated it turns out that those most sensitive to differences in the fragmentation properties all have a considerable energy dependence (see Fig. 3). We thus trained the neural network with equal and flat energy distributions for quarks and gluons in order to prevent the network from being influenced by the jet energies themselves. Such an artificial training sample is obtained by using individual jets taken from the Monte Carlo-generated events. In the following we denote this method **balanced energy training.**

As input variables to the neural network we finally selected the Fodor moments F_{11}, F_{15}, F_{20} and F_{31} together with the jet energy, in order to provide the energy dependence of the fragmentation variables. Instead of using the notation $F_{nm,i}$ to specify the value of fragmentation variable F_{nm} for jet i, we will simplify the notation by letting F_i represent the values of all the fragmentation variables used for jet i. It has been proven, see e.g. [12], that the output of a neural network will simply be the conditional probability for a jet to be a gluon (or a quark, depending on how the output is defined), given the input variables and the composition of the training sample. Using Bayes' theorem, the probability for jet1 to be a gluon jet can be expressed through the density functions, given that the values of the fragmentation variables are F_1 at an energy $\tilde{E}_1$, in the following way:

$$P_g^F(jet1|F_1) = \frac{\tilde{f}_g^E(\tilde{E}_1) f_g^F(F_1)}{\tilde{f}_g^E(\tilde{E}_1) f_g^F(F_1) + \tilde{f}_q^E(\tilde{E}_1) f_q^F(F_1)} = \frac{f_g^F(F_1)}{f_g^F(F_1) + f_q^F(F_1)} \tag{5}$$

where $P_g^F(jet1|F_1)$ is thus identical to the network output. $\tilde{f}^E$ denotes the density function of the artificial energy distribution used in the balanced energy training, which implies $\tilde{f}_g^E(E_1) = \tilde{f}_q^E(E_1)$. Since the jet energy ($E_1$) is given as input to the network together with the fragmentation variables (F_1), the correct notation of the density function for the fragmentation should be $f^F(F_1|E_1)$. However, in the balanced energy sample the energy will provide information only on the energy dependence of the fragmentation variables, as already explained, which means that we are in reality considering only the fragmentation variables. In order to avoid confusion, we have therefore decided to use the simplified notation $f^F(F_1)$.

The probability (5) based on the fragmentation properties is also valid in the case where, instead of treating individual jets, we make use of the fact that we know the number of quark and gluon jets in the event. Thus it is not necessary to train the network specifically for this situation. For 2-jet events, the output of a network trained on the quark and the gluon in a pair according to the balanced energy method, is just a simple function of the output from a network trained on individual jets, assuming that the jets fragment independently. Since we are only considering the jet core, this assumption is justified. Given the energies E_1 and E_2, we consequently have $f_{gq}^F(F_1, F_2|E_1, E_2) = f_g^F(F_1|E_1)f_q^F(F_2|E_2) = f_g^F(F_1)f_q^F(F_2)$, using our simplified notation, and again, due to the balanced energy training, the combined density functions $\tilde{f}_{gq}^E(E_1, E_2) = \tilde{f}_{qg}^E(E_1, E_2)$.

$$P_{gq}^{F_{12}}(jet1, jet2|F_1, F_2) = \frac{f_g^F(F_1)f_q^F(F_2)}{f_g^F(F_1)f_q^F(F_2) + f_g^F(F_2)f_q^F(F_1)} \tag{6}$$

Dividing the nominator and the denominator by $[f_g^F(F_1) + f_q^F(F_1)][f_g^F(F_2) + f_q^F(F_2)]$ and using the fact that, for individual jets the quark and gluon probabilities are related as $P_q^F(jet1|F_1) = 1 - P_g^F(jet1|F_1)$, we get:

$$P_{gq}^{F_{12}}(jet1, jet2|F_1, F_2) = \frac{P_g^F(jet1|F_1)[1 - P_g^F(jet2|F_2)]}{P_g^F(jet1|F_1)[1 - P_g^F(jet2|F_2)] + [1 - P_g^F(jet1|F_1)]P_g^F(jet2|F_2)}$$

where $P_{gq}^{F_{12}}(jet1, jet2|F_1, F_2)$ is now expressed in single jet probabilities which are identical to the network output values.

The 3-jet events from e^+e^- collisions contain a quark and an anti-quark which are identical from the point-of-view of the fragmentation, and the probability for a gluon jet is obtained by a simple extension of the expression for the 2-jet events:

$$P_{gqq}^{F_{123}}(jet1, jet2, jet3|F_1, F_2, F_3) = \frac{f_g^{F_1} f_q^{F_2} f_q^{F_3}}{f_g^{F_1} f_q^{F_2} f_q^{F_3} + f_g^{F_2} f_q^{F_1} f_q^{F_3} + f_g^{F_3} f_q^{F_1} f_q^{F_2}}$$

with $f_g^{F_i} = f_g^F(F_i)$, i=1,2,3. The probability for a gluon jet in a 3-jet event can be expressed in terms of individual jet probabilites using a similar procedure as for the 2-jet case.

$$\begin{aligned} &P_{gqq}^{F_{123}}(jet1, jet2, jet3|F_1, F_2, F_3) = \\ &\frac{P_g^{F_1}(1 - P_g^{F_2})(1 - P_g^{F_3})}{P_g^{F_1}(1 - P_g^{F_2})(1 - P_g^{F_3}) + P_g^{F_2}(1 - P_g^{F_1})(1 - P_g^{F_3}) + P_g^{F_3}(1 - P_g^{F_1})(1 - P_g^{F_2})} \end{aligned} \tag{7}$$

where $P_g^{F_i} = P_g^F(jeti|F_i)$, i=1,2,3.

7 Jet identification using jet energy and fragmentation properties

We now want to extract the conditional probability for a jet being a gluon jet, given both the jet energies and the values of the fragmentation variables which were used as input to our neural network. In the (2+1) jet case we obtain this by using the equations (2) and (6):

$$P_{gq}^{C_{12}}(jet1, jet2|E_1, E_2, F_1, F_2) = \frac{f_{gq}^{E_{12}} f_g^{F_1} f_q^{F_2}}{f_{gq}^{E_{12}} f_g^{F_1} f_q^{F_2} + f_{gq}^{E_{21}} f_g^{F_2} f_q^{F_1}}$$

where

$$f_{gq}^{E_{ij}} = \frac{f_{gq}^{E}(E_i, E_j)}{f_{gq}^{E}(E_i, E_j) + f_{gq}^{E}(E_j, E_i)}$$

If we now divide all the terms by $(f_{gq}^{E_{12}} + f_{gq}^{E_{21}})(f_g^{F_1} + f_g^{F_1})(f_q^{F_2} + f_q^{F_2})$ we obtain

$$P_{gq}^{C_{12}}(jet1, jet2|E_1, E_2, F_1, F_2) =$$
$$\frac{P_{gq}^{E_{12}} P_g^{F_1} P_q^{F_2}}{P_{gq}^{E_{12}} P_g^{F_1} P_q^{F_2} + P_{gq}^{E_{12}} P_q^{F_1} P_g^{F_2}} = \frac{P_{gq}^{E_{12}} P_g^{F_1}(1 - P_g^{F_2})}{P_{gq}^{E_{12}} P_g^{F_1}(1 - P_g^{F_2}) + (1 - P_{gq}^{E_{12}})(1 - P_g^{F_1}) P_g^{F_2}}$$

After division of all the terms by $P_g^{F_1}(1 - P_g^{F_2}) + (1 - P_g^{F_1}) P_g^{F_2}$ we finally get

$$P_{gq}^{C_{12}}(jet1, jet2|E_1, E_2, F_1, F_2) = \frac{P_{gq}^{E_{12}} P_{gq}^{F_{12}}}{P_{gq}^{E_{12}} P_{gq}^{F_{12}} + P_{gq}^{E_{21}} P_{gq}^{F_{21}}} \tag{8}$$

where we have used $P_{gq}^{E_{12}} = 1 - P_{gq}^{E_{21}}$ and $P_{gq}^{F_{12}} = 1 - P_{gq}^{F_{21}}$.

In a completely analogous way the corresponding conditional probability can be obtained for a 3-jet event.

$$P_{gqq}^{C_{123}}(jet1, jet2, jet3|E_1, E_2, E_3, F_1, F_2, F_3) =$$
$$\frac{P_{gqq}^{E_{123}} P_g^{F_1}(1 - P_g^{F_2})(1 - P_g^{F_3})}{P_{gqq}^{E_{123}} P_g^{F_1}(1 - P_g^{F_2})(1 - P_g^{F_3}) + P_{gqq}^{E_{312}}(1 - P_g^{F_1})(1 - P_g^{F_2}) P_g^{F_3} + P_{gqq}^{E_{231}}(1 - P_g^{F_1}) P_g^{F_2}(1 - P_g^{F_3})} =$$
$$\frac{P_{gqq}^{E_{123}} P_{gqq}^{F_{123}}}{P_{gqq}^{E_{123}} P_{gqq}^{F_{123}} + P_{gqq}^{E_{312}} P_{gqq}^{F_{312}} + P_{gqq}^{E_{231}} P_{gqq}^{F_{231}}} \tag{9}$$

8 Results

Fig. 4a shows the neural network output for individual jets in 3-jet events from e^+e^- collisions, based on the fragmentation variables discussed in section 6 and their energy dependence. The x-axis gives directly the probability that a jet from a quark and a gluon, respectively, is identified as a gluon jet. Using expression (7) we can calculate the event-based conditional probability of a jet to originate from a gluon, given the values F_1, F_2, F_3 for the fragmentation variables and the energies $\tilde{E}_1, \tilde{E}_2, \tilde{E}_3$, specified to account for the energy dependence of the fragmentation variables. From these calculations we select for each event the jet with the highest probability of being a gluon jet, giving a distribution as shown in Fig. 4b. We note that the distributions populate exactly the allowed region $1/3 < P_{g,max} < 1$.

Fig. 4c presents the event-based probability of a jet being a gluon jet as obtained from the ME calculation according to equation (1), and Fig. 4d gives the distributions of jets with the highest conditional probability, in the event, of coming from a gluon. In agreement with what has been indicated previously in the text, Figs. 4b and d confirm that the jet energies are much more efficient in identifying jets than are the fragmentation properties.

The event-based combined conditional probability for gluon jet identification, given the jet energies E_1, E_2, E_3 and the values F_1, F_2, F_3 for the fragmentation variables, achieved using equation (9), is given in Fig. 4e and finally, the jet per event with the highest combined probability of being produced by a gluon is plotted in Fig. 4f. The corresponding plots for (2+1) jet events from *ep* collisions are shown in Figs. 5a-f.

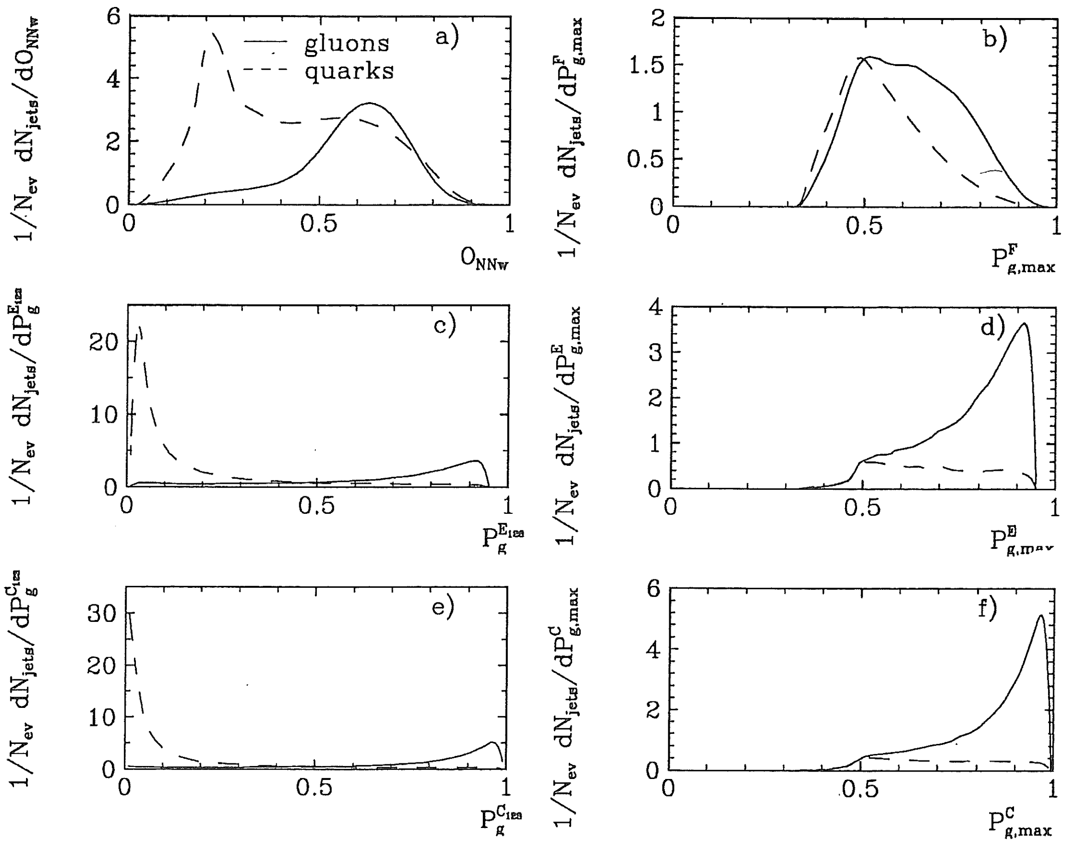

Figure 4: *Results for 3-jet events from e^+e^- shown as, a) the neural network output for individual jets, b) the $P^F_{g,max}$ distribution from the fragmentation, c) the gluon probability obtained from the ME calculation, d) the $P^E_{g,max}$ distribution from the jet energies, e) the combined conditional probability distribution according to equation (9), f) the $P^C_{g,max}$ distribution from the combined conditional probability.*

From the $P_{g,max}$ distributions we can now calculate the purity and efficiency as a function of P_{cut} according to expressions (3) and (4). In Fig. 6 the purity is plotted versus the efficiency separately for an identification based on the jet energies and on the fragmentation variables as well as for a combination of the two. Fig. 6a shows the results for 3-jet events generated with JETSET and for which the neural network has also been trained on a sample generated with JETSET. The corresponding results for (2+1) jet events are shown in Figs. 6b and c for samples generated with LEPTO and HERWIG, respectively, using networks trained on jets from the same generators. In this context, one should bear in mind that the *a*

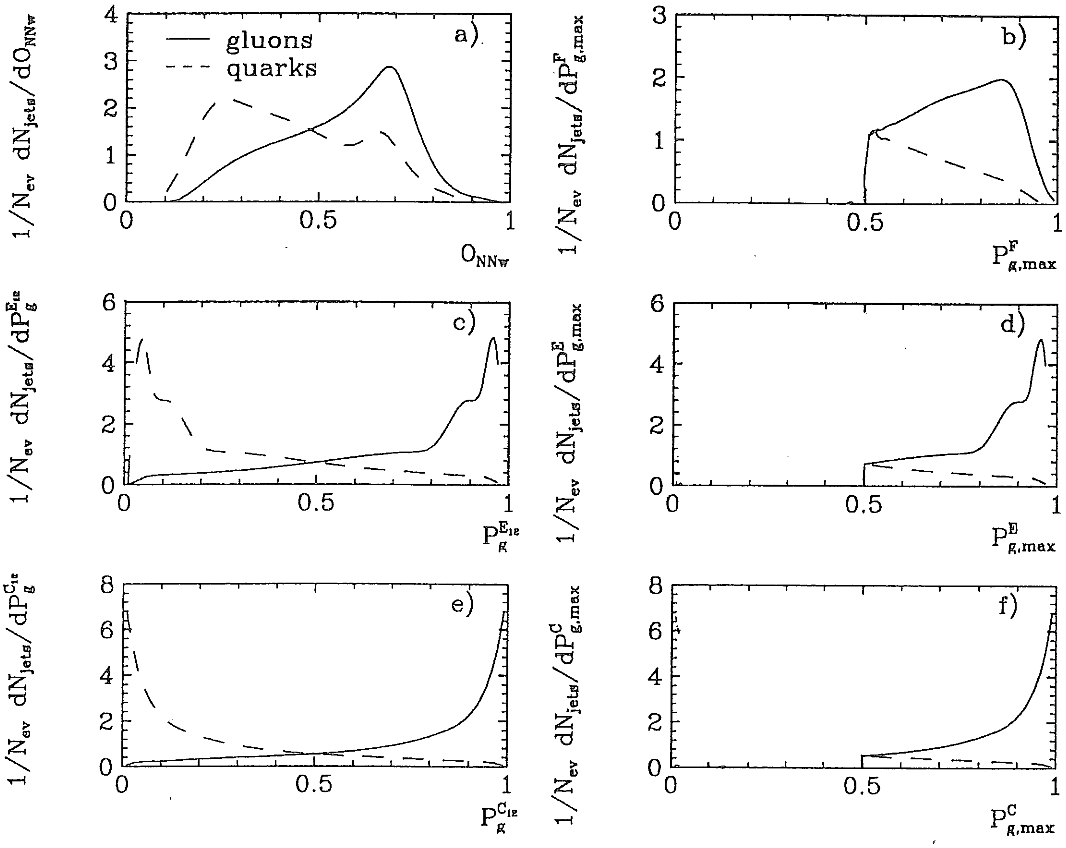

Figure 5: *Results on (2+1)-jet events from ep collisions shown as, a) the neural network output for individual jets, b) the* $P^F_{g,max}$ *distribution from the fragmentation, c) the gluon probability distribution according to equation (2), d) the* $P^E_{g,max}$ *distribution from the jet energies, e) the combined conditional probability distribution according to equation (8), f) the* $P^C_{g,max}$ *distribution from the combined conditional probability.*

priori probability of a correct gluon identification is 33% for 3-jet events, and 50% for 2-jet events. This is also the reason why the vertical axes of Fig. 6 have different starting points. **It must also be stressed that the final results presented here correspond to an identification of all jets in an event and they can therefore not be directly compared with results from identification of individual jets.**

The identification using fragmentation variables in general gives much poorer separation between quarks and gluons than the energy-based identification. However, the methods are normally complementary in the sense that events which are well separated by the jet energies are not necessarily those which are well separated by the fragmentation properties. Consequently an improved result is expected if the identifications from energy and fragmentation are combined.

From a comparison of Figs. 6a-c it can be seen that the energy-based identification of 3-jet events at LEP and (2+1) jet events at HERA are both 78-79% at 100% efficiency, but as an increasingly harder P_{cut} is made in the $P_{g,max}$ distributions the identification improves faster for the ep events than for the e^+e^- events. Concerning the fragmentation-based identification, it seems to give significantly better results for the ep events than for the e^+e^- events over the full efficiency range. This is in particular true for the HERWIG sample, for which the fragmentation-based identification is almost equally good as the one based on jet energies. The combined probabilities give improved identifications with respect to the jet energy results, which are essentially equal for the JETSET and LEPTO samples ($\approx$ 5%), while the improvment is somewhat greater for the HERWIG sample ($\approx$ 9%).

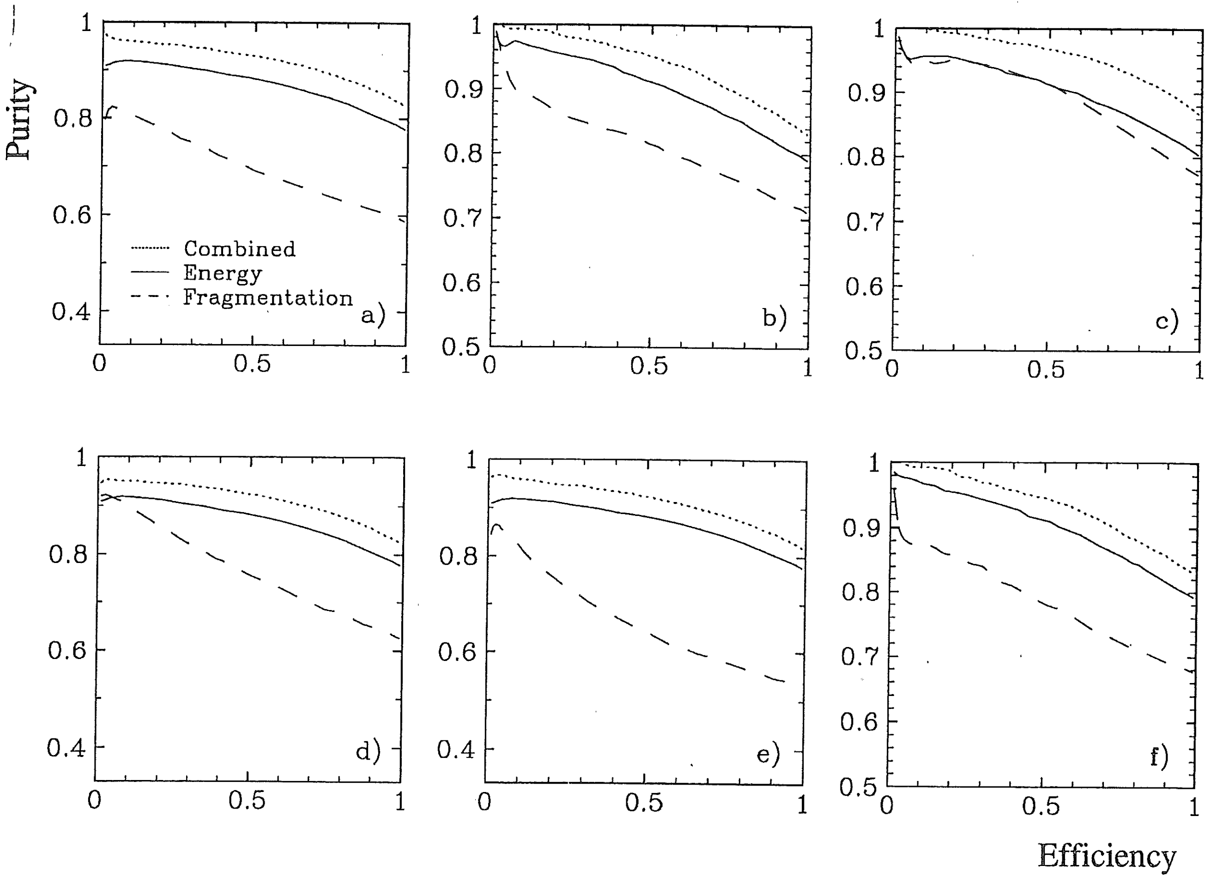

Figure 6: *The purity as a function of the efficiency for a network a) trained on a JETSET sample and tested on a JETSET sample, b) trained on a LEPTO sample and tested on a LEPTO sample, c) trained on a HERWIG sample and tested on a HERWIG sample, d) trained on a LEPTO sample and tested on a JETSET sample, e) trained on a HERWIG sample and tested on a JETSET sample, f) trained on a HERWIG sample and tested on a LEPTO sample.*

In order to investigate the process- and model-dependence we also present results from samples using a generator different from the one used in the training of the neural network.

These results are given in Figs. 6d-f. A comparison between Figs. 6a and d illustrates the process-dependence, while a comparison of Figs. 6b and f provides the model-dependence. From Figs. 6a and e the effects of both the model- and process-dependence can be extracted.

According to Figs. 6a and d the fragmentation result is better when a test sample from JETSET is presented to a network trained on LEPTO compared with a network trained on JETSET. The explanation of this strange behaviour is that the energy dependence of some Fodor moments are different for LEPTO and JETSET, causing the network to implicitly pick up this energy dependence in spite of the balanced energy training. Although it, in principle, should be possible to obtain a process-independent identification of jets using fragmentation variables, our results indicate that this is difficult to achieve in practice. The reason for this is most certainly that the phenomenological models used to generate e^+e^- events and ep events do not give a perfect description of these processes.

Concerning the model dependence of the fragmentation-based identification we have observed that a network trained to a HERWIG sample and applied on a HERWIG test sample gives a much higher degree of identification than a network trained on a LEPTO sample and tested on a LEPTO sample. This difference must be due to the different fragmentation models used in HERWIG and LEPTO. However, if we now compare Figs. 6b and f we notice that the curves are almost identical, indicating that the separation between quarks and gluons is optimized in the same way by the two networks trained on LEPTO and HERWIG samples. Thus a common network can be used to differentiate between quarks and gluons for samples generated with both LEPTO and HERWIG.

9 Conclusions

We have studied the problem of identifying jets using the jet energies and fragmentation variables separately. Jets produced in simulated e^+e^- and ep collisions were used to investigate a possible process-independent identification, and two different fragmentation schemes were used to study the model dependence.

The conditional probability of a jet to originate from a gluon (or a quark) can be calculated from Bayes' theorem provided the density functions for gluons and quarks with respect to jet energies and fragmentation variables are known. The formalism for extracting these probabilities, for the event types investigated here, has been presented. The advantages of working with probabilities are the simple interpretation of the results and the procedure of combining the results from the identifications based on the jet energy and the fragmentation variables. Since jet identification based on fragmentation variables is a multidimensional problem, the neural network technique is the only feasible way to convert the full information on the fragmentation into a probability of having a certain type of jet. By using the neural network as an estimate of Bayesian probabilities, all calculations are performed in the firm framework of mathematical statistics, which is clearly advantageous compared with using the neural network as a black-box classifier.

The event-based level of identification using the jet energies is about 80% at 100% efficiency for both e^+e^- 3-jet events and ep QCD-Compton events, whereas the fragmentation-based identification gives 60% purity for the e^+e^- events and more than 70% for the *ep* events, also at 100% efficiency. A combination of the two leads to improvments, over the full efficiency range, of between 5% and 9% with respect to the results from the jet energy alone. The identification of the jets in a complete event is a much stronger requirement than the identification of individual jets and therefore a direct comparison of such results is not possible.

One advantage of performing the jet identification based on jet energies and fragmentation variables separately is that the neural network will concentrate on extracting the subtle differences in the fragmentation of quarks and gluons without being influenced by the differences in the jet energies. Another advantage is that it allows an investigation of whether a process independent identification is possible, using the fragmentation properties. The fragmentation-based results are observed to be significantly different depending on the fragmentation model used. On the other hand, the variation of the results from a combination of the energy- and fragmentation-based identifications is much less striking, which is consistent with previous observations.

Acknowledgements: The analysis described in this paper as well as the way the results should be presented have gone through several metamorphoses as the work has proceeded. In the initial phase we had many animated discussions with O. Bärring and V. Hedberg, which forced us to find convincing arguments for our analysis strategy. We are indebted to G. Ingelman and M. Lindström for their careful reading of the manuscript and for giving constructive comments, suggestions and critisism. Three of us would like to thank the DESY Directorate for its kind hospitality.

A Appendix

Bayes' Theorem

If the entire event space is composed of the subsets $B_i, (i = 1...n)$, with no elements in common, then the subsets are said to be *mutually exclusive* and *exhaustive*, which means that

$$\sum_{i=1}^{n} P(B_i) = 1 \tag{10}$$

Provided A is also a set that belongs to the event space, Bayes' theorem states

$$P(B_i|A) = \frac{P(A|B_i)P(B_i)}{\sum_{j=1}^{n} P(A|B_j)P(B_j)} \tag{11}$$

This theorem can be proven by starting from the definition of the conditional probability, $P(A \cap B) = P(B|A)P(A) = P(A|B)P(A)$, where $P(B|A)$ is to be interpreted as the probability that the event B occurs under the condition that A has already occurred. For our subset B_i we thus get

$$\begin{aligned} P(A \cap B_i) &= P(B_i|A)P(A) = P(A|B_i)P(B_i) \\ \Rightarrow P(B_i|A) &= \frac{P(A|B_i)P(B_i)}{P(A)} \end{aligned} \tag{12}$$

The elements of a set might be classified according to more than one criterion so that, for example, we have $\sum_{i=1}^{m} P(A_i) = \sum_{j=1}^{n} P(B_j) = 1$. If some of the criteria are being neglected in the classification we can define the *marginal probability* for A_i according to

$$P(A_i) = \sum_{j=1}^{n} P(A_i \cap B_j) = \sum_{j=1}^{n} P(A_i|B_j)P(B_j) \tag{13}$$

where we have again used the definition of the conditional probability for the second step. Using this expression we can now rewrite equation (12) to obtain equation (11).

If we now consider the (2+1) jet case, we could take the subset B_i to represent the four configurations of quark- and gluon jets possible if the jets are identified individually in the event. These are $B_i = \{gq, qg, qq, gg\}$, where, for example, gq means that jet1 is a gluon jet and jet2 a quark jet. Since we have selected events which have one quark and one gluon in the final state (QCD-Compton events) we introduce this information into our probabilities by considering only the allowed configurations, and define the two subsets $B_1 = \{gq\}$, $B_2 = \{qg\}$. Assuming that the two jets are in a state C, which might refer to energy and/or fragmentation variable values, we can compute the probability of having a gq configuration in the state C, by using Bayes' theorem.

$$P(gq|C) = \frac{P(gq)P(C|gq)}{P(gq)P(C|gq) + P(qg)P(C|qg)} \tag{14}$$

This formula is valid when state C has a positive probability $P(C) > 0$. When C is defined in terms of a continuously varying quantity, the discrete probabilities in Bayes formula should be replaced by probability density functions. For example, if C represents a continuous energy variable E, then (14) reads

$$P(gq|E) = \frac{P(gq)f_{gq}(E)}{P(gq)f_{gq}(E) + P(qg)f_{qg}(E)} \tag{15}$$

where f_{gq} and f_{qg} are the joint energy density functions for pairs gq and qg, respectively.

For the 3-jet case, we have 8 possible configurations of quarks and gluons. After deleting the impossible combinations, the remaining subsets are $B_i = \{gqq, qgq, qqg\}$. The final expression becomes

$$P(gqq|C) = \frac{P(gqq)P(C|gqq)}{P(gqq)P(C|gqq) + P(qgq)P(C|qgq) + P(qqg)P(C|qqg)} \tag{16}$$

References

[1] L. Lönnblad, Peterson and Rögnvaldsson, Phys. Rev. Lett. 65(1990)1321.
L. Lönnblad, Peterson and Rögnvaldsson, Nucl. Phys. B349(1991)675.
Csabai, Czako and Fodor, Nucl. Phys. B374(1992)288.

[2] T. Sjöstrand, Computor Phys. Comm. 39 (1986) 347, it ibid 43 (1987) 367.

[3] B. Andersson, G. Gustafson, G. Ingelman, T. Sjöstrand, Phys. Rep. 97(1983)31.

[4] G. Ingelman, LEPTO version 6.1, in Proceedings 'Physics at HERA', Eds W. Buchmüller, G. Ingelman, DESY Hamburg 1992, vol. 1-3 and references therein.

[5] G. Marchesini, B.R. Webber, G. Abbiendi, I.G. Knowles, M.H. Seymour and L. Stanco, Computer Phys. Comm. 67(1992)465.

[6] T. Sjöstrand, Computer Phys. Comm. 28 (1983) 227

[7] V. Hedberg, G. Ingelman, C. Jacobsson, L. Jönsson, Z. Phys. C63 (1994) 49.

[8] D. Graudenz, N. Magnussen,
M. Fleischer et al.,
V. Hedberg, G. Ingelman, C. Jacobsson, L. Jönsson,
Proceedings 'Physics at HERA', Eds W. Buchmüller, G. Ingelman, DESY Hamburg 1992, vol. 1, p. 261, 303, 331.

[9] K. C. Hoeger, Measurement of x, y, Q^2 in Neutral Current Events, in Proceedings 'Physics at HERA', Eds W. Buchmüller, G. Ingelman, DESY Hamburg 1992, vol. 1, p. 43

[10] L. Lönnblad, C.Peterson, H. Pi and T. Rögnvaldsson, Comp. Phys. Comm. 67(1991)193.

[11] Fodor, Phys. Rev. D41(1990)1726.

[12] M.D. Richard, R.P. Lippman, Neural Comp 3 (1991) 461.

Appendix D

The H1 Forward Muon Spectrometer

Nuclear Instruments and Methods in Physics Research A 340 (1994) 304–308
North-Holland

NUCLEAR
INSTRUMENTS
& METHODS
IN PHYSICS
RESEARCH
Section A

The H1 forward muon spectrometer

H. Cronström [a], V. Hedberg [a], C. Jacobsson [a], L. Jönsson [a,*], H. Lohmander [a], M. Nyberg [a], I. Kenyon [b], H. Phillips [b], P. Biddulph [c], P. Finnegan [c], J. Foster [c], S. Gilbert [c], C. Hilton [c], M. Ibbotson [c], A. Mehta [c], P. Sutton [c], K. Stephens [c], R. Thompson [c]

[a] *Physics Department, University of Lund, Lund, Sweden*
[b] *School of Physics and Space Research, University of Birmingham, Birmingham, UK*
[c] *Physics Department, University of Manchester, Manchester, UK*

Received 21 September 1993

The H1 detector started taking data at the electron–proton collider HERA in the beginning of 1992. In HERA 30 GeV electrons collide with 820 GeV protons giving a strong boost of the centre-of-mass system in the direction of the proton, also called the forward region. For the detection of high momentum muons in this region a muon spectrometer has been constructed, consisting of six drift chamber planes, three either side of a toroidal magnet. A first brief description of the system and its main parameters as well as the principles for track reconstruction and T_0 determination is given.

1. General description

The purpose of the forward muon spectrometer is to measure high energy muons in the range of polar angles $3° \leqslant \theta \leqslant 17°$. The detector consists of drift chamber planes, either side of a toroidal magnet. The design specifications aim at measuring the momenta of muons in the range between 5 and 200 GeV/c, the lower limit being given by the amount of material the muons have to penetrate and the influence on the momentum resolution of the multiple Coulomb scattering in the magnet iron. The upper limit is set by the magnetic field strength of the toroid together with the spatial resolution of the drift chambers. The expected momentum resolution at 5 GeV/c is 24% and deteriorates slowly to 36% at 200 GeV/c above which there is a danger of misidentifying the charge of the muon. Muon momenta below 5 GeV/c will be measured in the forward tracker.

Fig. 1a shows schematically the detector arrangement and the toroid magnet. The drift chamber planes, which increase in size from about 4 m diameter for the first detector plane to 6 m diameter for the last, are all divided into octants which are formed from individual drift cells accurately mounted on Al-frames. The orientation of the drift cells is such that four of the planes essentially measure the polar angle (θ) and thereby provide the momentum of the traversing muon whilst the remaining two measure the azimuthal angle (ϕ). Each plane consists of a double layer of drift cells such that each layer is displaced with respect to the other by half a cell width (Fig. 1b). This arrangement enables the resolution of left–right ambiguities and also the determination of T_0 as will be explained below. The total number of drift cells is 1520.

The toroid is 1.2 m thick and constructed out of eight semicircular steel modules with an inner radius of 0.65 m and an outer radius of 2.9 m. Each of the twelve rectangular coils which provide the field consists of 15 turns of watercooled Cu-tube, 11.5×11.5 mm^2. At a current of 150 A the field strength varies from about 1.75 T at the inner radius to about 1.5 T at the outer radius. Field measurements made in the centre of each coil show a variation of less than 1%. A more detailed description of the toroid magnet can be found in ref. [1].

2. Chamber design

All drift cells have a rectangular cross section with a depth of 2 cm, a width of 12 cm and lengths between 40 and 240 cm. With a central sense wire the maximum drift distance becomes 6 cm. The cells have 50 μm thick nichrome wires except for the inner short cells where the diameter is 40 μm. For cells longer than 1.5 m there is a wire support in the middle. As illustrated in Fig. 2 each cell comprises two PCB planes, copper-coated on both sides, and 0.7 mm thin extruded Al-

---

* Corresponding author.

SSDI 0168-9002(93)E1039-Z

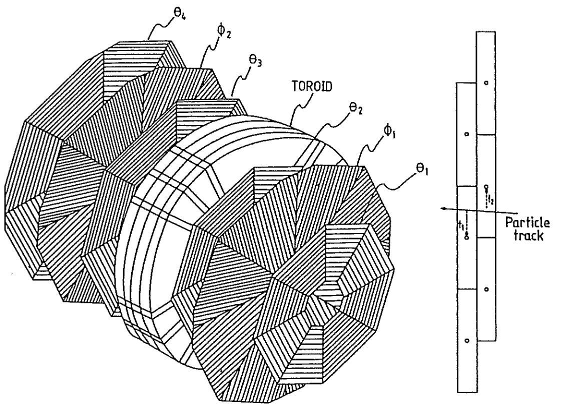

Fig. 1. (a) A schematic view of the forward muon spectrometer and (b) the cell structure of a double layer.

profiles to minimise the dead space between cells. The outer copper surface of the PCB is kept at ground to form a screened box while the inner surface has been machined to give 4 mm wide strips. These are used as drift electrodes connected to a 230 MΩ metal film resistor chain mounted on the end cap to obtain a uniform drift field. The end caps are made of moulded Noryl with high precision holes to locate the crimp pins for fixing the sense wires and provide holes for the gas connections. One end contains the high voltage distribution resistor chain and the sense wire readout connection isolated via a 1 nF ceramic disc capacitor. Sense wires of adjacent cells are linked together via a 330 Ω resistor at the other end forming the equivalent of a U-shaped cell which then is read out at both ends. This allows not only a determination of the track position transverse to the sense wire from the measurement of the drift time but also the coordinate along the wire by charge division measurement and thereby giving information on which cell of a coupled pair was hit.

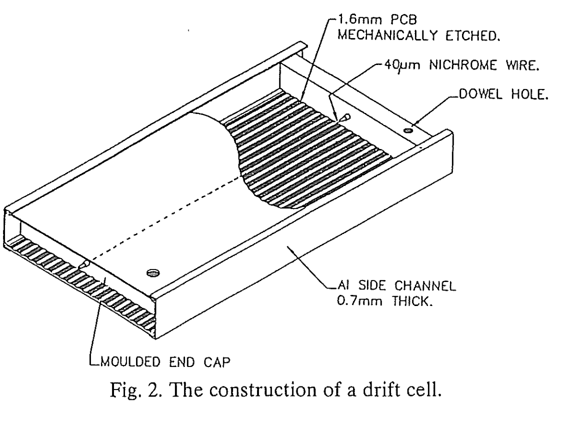

Fig. 2. The construction of a drift cell.

3. The chamber gas and high voltage system

The choice of gas for the drift chambers was determined by several requirements. One is the desire to work in a drift voltage range where the drift velocity is constant. Further the gas has to be fast enough for the pulse to arrive in time for the trigger and finally it should be nonflammable for safety reasons. Currently the so-called FMS gas (forward muon spectrometer gas), which is a mixture of 92.5% argon, 5% CO_2 and 2.5% methane, has been chosen for the chambers. The gas is mixed and purified in a recirculator [2]. The chambers have a total gas volume of 4 m^3, and with a small overpressure of about 0.2 mbar measured at the output, the return gas flow is typically 90% of the input and the oxygen content is measured to be of order 100 ppm. For the FMS gas the drift velocity as a function of the drift field voltage, corrected for atmospheric pressure, is shown in Fig. 3. An average drift field of 480 V/cm gives the desired drift velocity of ~ 5 cm/μs. The drift field is defined by an increasing positive potential from the cathode at ground to +2.88 kV on the centre electrode at the position of the sense wire. The sense wire is kept typically at 4.21 kV for the 40 μm wires and at 4.26 kV for the 50 μm wires. The gas gain is controlled by the difference in voltage between the sense wire and the drift field close to the wire.

A 120-channel CAEN 127 system supplies distribution boxes on the detector with high voltage via 50 m long coaxial cables. One 6 kV 1 mA module supplies drift voltage to an entire octant, feeding 20–40 individual resistor chains. Similarly an 8 kV 200 μA module supplies the sense voltage to all but the 12 innermost cells of a θ-octant, which in case of bad beam conditions might be set to a lower voltage. For the φ-octants the central section which is close to the beam tube can be moved outwards mechanically by remote controls and thus there is no need for any special HV arrangement.

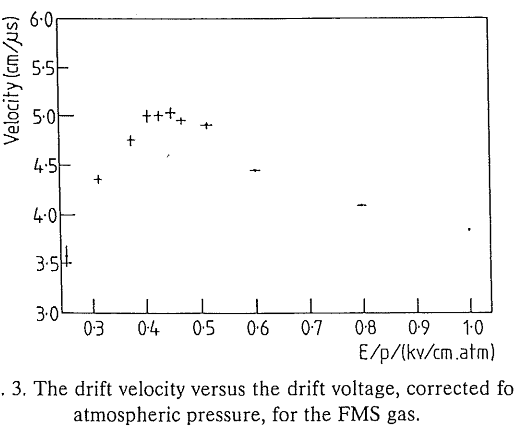

Fig. 3. The drift velocity versus the drift voltage, corrected for atmospheric pressure, for the FMS gas.

There is a continuous monitoring of the gas composition and flow rates as well as of the high voltage, communicated via an Apple Macintosh II ci in the control room. From this work station it is also possible to control the high voltage of the detector and the toroid magnet.

4. The readout system

The signals are read out into 8 channel preamplifiers of standard H1 design [3] mounted close to the cells. The output pulses are driven down 50 m long coaxial cables to F1001 flash analogue to digital converters (FADC) [3] run in common stop mode. Signals are digitised with the equivalent of 10 bit resolution (8 bit nonlinear response) in 9.6 ns time bins, phase locked to the HERA beam crossing frequency. These are stored in a circular buffer with a depth of 256 time bins. Each crate of 256 FADCs is controlled by a scanner [4] which on receiving the first trigger stops the buffer and scans the preceding 256 digitisings for hits. Each scanner then transfers the zero suppressed data to a front end processor where the pulses are analysed to extract start times and charge contents.

5. The charge–time analysis

Only the rising edge and peak region of a pulse is used to get the time and charge information. A pulse is said to start when there are two successively rising digitisings above threshold. The end of a pulse is taken as the second successive digitising after the peak which is below threshold, or eight 9.6 ns time bins from the start of the pulse, whichever occurs first. The arrival time of the pulse is obtained by extrapolating a line fitted to the steepest part of the leading edge back to the intercept with the background level. With a test setup, looking at cosmic muons, this method gave a resolution of < 200 μm as illustrated in Fig. 4. This result was obtained with a gas mixture of 90% argon and 10% propane providing a drift velocity of 4 cm/μs. However, to satisfy the gas requirements specified in section 3, we have, as mentioned earlier, chosen the FMS gas with a drift velocity of ~ 5 cm/μs, resulting in an expected resolution of ~ 250 μm. Pairs of pulses which originate from the same hit are associated by requiring the difference of their arrival times to be less than the full propagation time through the two sense wires of the linking resistor.

The collected charge is found by integrating the digitisings of the pulses from the two wire ends over intervals of the same length, with subtraction of a constant background. A correction for fractional time bins was found to be important since the start times for the two pulses are subject to variable propagation delays. With cosmic muons in the test setup we found a charge-division versus distance characteristics which was linear to about 1%, which is well matched to the resolution.

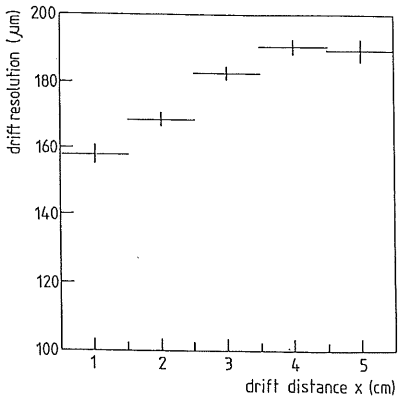

Fig. 4. The space resolution of a drift cell as a function of drift distance for the gas mixture 90% argon and 10% propane (drift velocity 4 cm/μs).

6. Track reconstruction

The space points obtained from the charge–time analysis of the chamber hits are used in a three-step procedure for track reconstruction which starts with the pairing of hits in each double layer followed by association of pairs into straight track segments and finally the linking of track segments through the toroid to form full tracks and thus provide a momentum measurement. Pair finding in the double layers is decisive due to the displacements of cells which results in the sum of drift times being a constant (compare Fig. 1b). A vertex pointing requirement is applied as selection criteria but also unpaired hits are kept to be considered in the track segment finding where we demand three out of four hits in the θ-layers. The measuring errors of the space points for a pair define a cone which is extrapolated to the other θ-layer on the same side of the toroid. In the area defined by the cone, hits are tried for segment fits and are selected by a χ^2-cut. In the future the information from the ϕ-layers will also be used.

For the linking procedure each pretoroid segment is tracked through the magnetic field of the toroid, taking into account energy loss and multiple Coulomb scattering in the magnet iron. By doing this for a minimal reconstructable momentum of 2.5 GeV/c in the spectrometer and for either of the two muon charges possible, regions in the θ-layers after the toroid are defined inside which segment candidates for linking are considered. From the crossing angle of two linked segments an estimate of the momentum is made. Starting from the pretoroid segment and the estimated momentum the tracking is repeated as the momentum is changed in small steps around the estimated value. Each post-toroid segment obtained from the tracking is compared to the actual segment found and a χ^2 is calculated. The minimum of the χ^2 variation with momentum defines the momentum corresponding to the best fit.

Fig. 5 shows a schematic side view of the H1-detector with the central and forward tracking devices and the calorimeter all surrounded by the instrumented iron. The forward muon spectrometer can be seen to the left of the main H1-detector. A clear muon track originating from the vertex region can be followed through the various subdetectors extending all the way to the end of the forward muon spectrometer. The track coordinates are given by the radial distance from the beam line, R, and the longitudinal Z-coordinate in the direction of the proton beam. However, since the instrumented iron only gives information on the vertical position, X, a radius coordinate cannot be extracted and consequently this track segment is plotted in X, Z-coordinates. This results in the apparent non-alignment of that particular track segment.

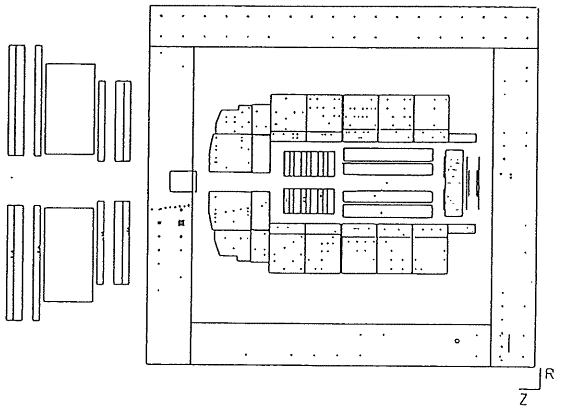

Fig. 5. A side view of a genuine event with a muon penetrating the complete detector.

7. Drift velocity and T_0 determination

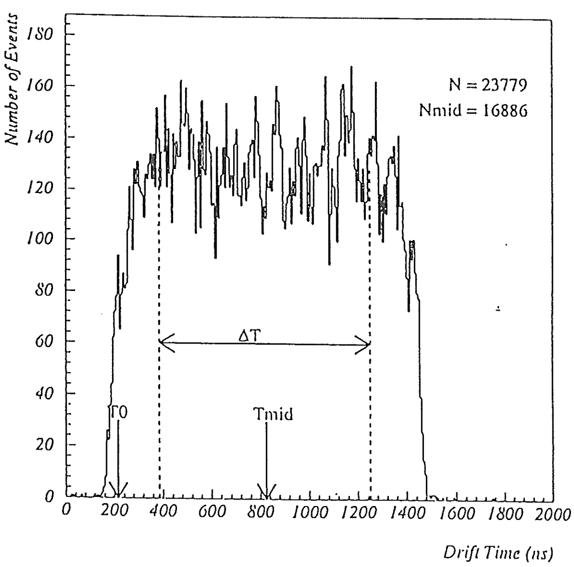

Fig. 6. The drift time distribution for beam halo tracks used to extract T_0 with the FMS-gas.

Beam halo muons are used to determine the drift velocity. From the uniform population of the total number of tracks (N) over the full drift distance (ΔY), recorded in a run, a rectangular distribution is expected if the drift velocity is constant. However, due to field variations close to the sense wire, dependence on the angle of the track, the possibility of tracks traversing only the corner of a cell etc., the drift velocity will be altered and cause a smearing of the distribution (Fig. 6). In spite of this smearing, the drift time (T_{mid}), corresponding to half the drift distance (3 cm), can be defined as the time which leaves equal number of tracks above and below. Taking an arbitrary time interval (ΔT) symmetrically around T_{mid}, where the distribution is still flat, we can count the number of tracks (N_{mid}) in this interval and use it for a determination of the drift velocity by the following expression:

$$v = \Delta Y N_{\text{mid}} / (\Delta T N).$$

The result is $v = 4.926 \pm 0.039$ cm/μs.

T_0 is determined from the specific geometry of the detector which makes one of the following check sums true for each track.

$$T_1 + T_2 + T_3 + T_4 = 4T_{\text{mid}},$$

$$T_1 + T_2 - T_3 - T_4 = 0,$$

where T_1, T_2, T_3 and T_4 are drift times in the four θ-layers. The first check sum thus will provide an independent measurement of T_{mid}. T_0 can now be determined from the expression:

$$T_0 = (3\ \text{cm}/v) - T_{\text{mid}}.$$

The widths of the two check sum distributions can be used to find the spatial resolution of the chambers.

8. Chamber alignment

The drift chambers must be aligned with respect to each other and to the rest of the detector. The cells of a θ-layer are positioned on its supporting Al-frame to a precision of ~ 50 μm along the drift direction and to ~ 1 mm in the two other directions. This is better than the achievable resolution and therefore we only have to consider the alignment of the full octants.

Simulation studies and analysis of a small sample of real data have shown that beam halo tracks are suitable for providing the two translational and one rotational quantities which are needed to specify the position of the octant in the plane transverse to the beam direction. Further studies with angle tracks together with the survey will determine the relative positions of the octants along the direction of the beam [5].

Acknowledgements

We wish to acknowledge the substantial effort from the mechanical and electronic workshops at the Universities of Lund and Manchester, together with the contributions of the engineers from the PAG group at the Rutherford Laboratory. We thank the Swedish and United Kingdom funding agencies for their financial support to the construction of the detector. Further we acknowledge the technical facilities provided at the installation phase by DESY.

References

[1] I. Abt et al., DESY Preprint 93-103 (1993).
[2] G. Kessler and W. von Schröder, private communication.
[3] J. Bürger et al., Nucl. Instr. and Meth. A 279 (1989) 217.
[4] R.J. Ellison and D. Mercer, H1 Internal Note 4/87-63.
[5] P. Sutton, Ph.D. Thesis, University of Manchester (1993).